



TECHNISCHE  
UNIVERSITÄT  
WIEN

DIPLOMARBEIT

# Irreducible Vertex Divergences in Strongly Correlated Metallic Systems

## The Case of the Anderson Impurity Model

Ausgeführt am  
Institut für Festkörperphysik  
der Technischen Universität Wien

unter der Anleitung von  
Associate Prof. Dr. Alessandro Toschi  
und:  
Patrik Gunacker MSc.

durch

**Patrick Chalupa, BSc.**  
Fabriksgasse 2A/13, 2603 Felixdorf

---

Datum

---

Unterschrift



## Abstract

The recently discovered occurrence of multiple divergences in the irreducible vertex functions of strongly correlated electron models, poses serious problems to the state-of-the-art many-body theory. Dynamical mean-field theory (DMFT) calculations for the Hubbard model have shown several lines of divergences of the irreducible vertex function, surrounding the Mott-Hubbard metal-insulator transition, a clear hint of a highly non-perturbative origin.

At high temperatures/large interaction ( $U$ ), where the Hubbard model approaches the atomic limit, the divergences could be ascribed to a unique underlying energy scale  $\nu^*$ . This simple picture is however not applicable in the most interesting parameter regime of low temperatures and intermediate  $U$ , where the system behaves like a correlated Fermi-liquid metal.

For this reason a simpler model was analysed, where a similar physics could be realized: the Anderson impurity model. This provides a more feasible way to treat the Fermi-liquid quasiparticle physics in the parameter regime of interest.

In a preceding *Projektarbeit* I performed CT-HYB calculations at the two particle level, using *w2dynamics*. The results show the first divergence line for the Anderson impurity model, with an unexpected low temperature behaviour.

Motivated by these preliminary findings, in this thesis an investigation of the whole phase diagram of the Anderson impurity model has been performed. In particular, using *w2dynamics*, additional lines of divergences were found: They could be classified in terms of the properties of their associated singular eigenvectors and compared with the corresponding ones found in other many-electron systems. This information provides novel insights on the physical mechanism underlying the breakdown of many-body perturbation theory, clarifying some aspects (such as the relation of the divergences with the Mott-Hubbard transition), which were not fully understood yet. In the final part of the master thesis the implication of the low-temperature behaviour of the divergence lines in the Anderson impurity model onto other models (such as the Hubbard) is discussed as well.

## Deutsche Kurzfassung

Das vor Kurzem entdeckte Auftreten mehrfacher Divergenzen in irreduziblen Vertexfunktionen von stark korrelierten Elektronensystemen stellt für die moderne Vielteilchentheorie ein grundlegendes Problem dar. Dynamische Molekularfeldtheorie (DMFT) Rechnungen für das Hubbard Modell haben Divergenzlinien in der Umgebung des Mott-Hubbard Metall-Isolator Übergangs gezeigt, ein deutlicher Hinweis auf einen höchst nicht-perturbativen Ursprung.

Bei hohen Temperaturen/ großer Wechselwirkung ( $U$ ), wo sich das Hubbard Modell dem atomaren Limes annähert, konnten diese Divergenzen einer zugrunde liegenden eindeutigen Energieskala  $\nu^*$  zugeordnet werden. Diese Vereinfachung ist jedoch im interessantesten Parameterbereich, nämlich bei tiefen Temperaturen und mittlerem  $U$  wo sich das System wie eine korrelierte Fermiflüssigkeit verhält, nicht anwendbar.

Aus diesem Grund wurde ein einfacheres Modell mit gleichartiger Physik analysiert: Das Anderson Störstellenmodell. Dies bietet einen leichter zu realisierenden Weg, die Physik der Quasiteilchen der Fermiflüssigkeit im gewünschten Parameterbereich zu behandeln.

In einer vorangegangenen *Projektarbeit* habe ich, unter Verwendung von *w2dynamics*, CT-HYB Berechnungen auf dem Zweiteilchenniveau durchgeführt. Die Ergebnisse zeigen die erste Divergenzlinie für das Anderson Störstellenmodell, mit einem unerwarteten Tieftemperaturverhalten.

Aufbauend auf diesen ersten Erkenntnissen, wurde in dieser Masterarbeit das gesamte Phasendiagramm des Anderson Störstellenmodells untersucht. Im Besonderen wurden, unter Verwendung von *w2dynamics*, weitere Divergenzlinien gefunden, die durch das Verhalten deren entsprechenden singulären Eigenvektoren klassifiziert werden konnten, und mit Divergenzlinien von anderen Mehrelektronensystemen verglichen. Durch diese Informationen konnten neue Einsichten in den Mechanismus, der dem Versagen der Vielteilchenstörungstheorie zugrunde liegt, gewonnen werden, was auch einige Aspekte (zum Beispiel den Zusammenhang der Divergenzen mit dem Mott-Hubbard Übergang), die soweit noch nicht komplett verstanden waren, klärt. Im abschließenden Teil der Masterarbeit wird die Bedeutung des Tieftemperaturverhaltens der Divergenzlinien des Anderson Störstellenmodells, auf andere Modelle (wie zum Beispiel das Hubbard Modell) diskutiert.

## Dedication and Acknowledgement

This thesis and the completion of my studies is owed to the support from so many people, of which I would like to thank some.

First of all, I want to thank my supervisor, Alessandro Toschi, whose inspiring lectures on the basic as well as the modern topics of quantum theory and theoretical solid state physics are one of the main reasons I decided to start working in this field. His support, dedication, and didactic skills made writing this thesis a most enjoyable and interesting project for me. Grazie mille per il costante supporto e la fiducia che mi hai dato. Non vedo l'ora di lavorare con te nel corso dei prossimi anni!

Furthermore, I am indebted to Patrik Gunacker, without whom obtaining results to this extent would not have been possible. Thank you for the hours you spent teaching me how to use *w2dynamics* and for helping me to deal with some subtle computational aspects.

I also want to thank Karsten Held, Olle Gunnarsson, Sergio Ciuchi, Georg Rohringer, Thomas Schäfer and Philipp Hansmann for insightful discussions as well as Giorgio Sangiovanni for giving me the opportunity to present and discuss my results in Würzburg.

I also acknowledge financial support from the Austrian Science Fund (FWF) through the project I – 2794 – N35. The numerical calculations have been performed on the VSC3 cluster.



# Contents

<b>1</b>	<b>Motivation</b>	<b>1</b>
<b>2</b>	<b>Introduction</b>	<b>3</b>
2.1	Formalism . . . . .	3
2.1.1	Basic Definitions . . . . .	4
2.1.2	Divergences of the Irreducible Vertex . . . . .	9
	Luttinger Ward formalism . . . . .	11
2.2	Overview of the recent developments . . . . .	12
2.2.1	Disordered Models . . . . .	13
2.2.2	Atomic Limit of the Hubbard Model . . . . .	16
2.2.3	Hubbard Model . . . . .	17
2.2.4	Implications at the one-particle level . . . . .	20
2.3	Anderson Impurity Model . . . . .	24
2.3.1	Local Magnetic Moments . . . . .	26
2.4	Kondo Scale . . . . .	27
<b>3</b>	<b>Methods</b>	<b>33</b>
3.1	CT-HYB . . . . .	33
3.1.1	The random number generator . . . . .	34
3.2	Exact Diagonalization . . . . .	35
3.3	Postprocessing: Analysis of Vertex Divergences . . . . .	35
3.3.1	Extrapolation procedure to determine $\tilde{U}$ . . . . .	36
<b>4</b>	<b>Results and Discussion</b>	<b>39</b>
4.1	Phase Diagram . . . . .	39
4.1.1	Crossing of Divergence Lines . . . . .	45
	Boxanalysis . . . . .	45
	ED check . . . . .	46
4.2	Evolution of the singular eigenvectors . . . . .	51
4.2.1	Evolution of the singular eigenvectors - along a given divergence line for different temperatures . . . . .	53

4.2.2	Evolution of the singular eigenvectors - comparison for different divergence lines . . . . .	62
4.2.3	Symmetry of the singular eigenvectors . . . . .	63
4.2.4	Relation of the vertex divergences and the Green's function . . . . .	67
4.2.5	Evolution of the eigenvectors - the role of the interaction $U$ . . . . .	69
<b>5</b>	<b>Conclusions</b>	<b>73</b>
<b>6</b>	<b>Outlook</b>	<b>77</b>
	Error Analysis . . . . .	77
	Kondo scale . . . . .	78
	Two-site model . . . . .	78
	Symmetry broken phases . . . . .	78
	<b>Bibliography</b>	<b>1</b>



# Chapter 1

## Motivation

At the center of this thesis stands the investigation of strong-coupling pathologies, which occur in the many-electron theory at the one- and the two-particle level, shaking some of the foundations of forefront computational approaches. In particular, in recent studies [1, 2, 3, 4, 5, 6, 7, 8, 9, 10] divergences in the irreducible vertex functions, on which we will focus over the course of this work, as well as multivalued determinations of self-energies in the framework of the Luttinger-Ward formalism have been reported. Though unexpected, these features are quite general, as they appear in several many-electron models, among them e.g. the *Falicov-Kimball model*, the *Hubbard atom* and the *Hubbard model*.

The vertex divergences have been observed in these models for specific sets of interaction and temperature values, leading to non-trivial divergence lines extending over large parts of the corresponding phase diagrams. Specifically, the results for models containing a metal-insulator transition [11] (MIT), such as the Dynamical Mean-Field Theory (DMFT) solution of the Hubbard model, show divergence lines also in the correlated metallic regime, at lower interaction values than the MIT itself. This is somewhat surprising, because the vertex divergences are incompatible with the validity of the perturbation theory. At the same time perturbation theory was, however, expected to hold at least at low energies up to the onset of the MIT, due to the metallic nature of the ground state. Moreover, from a precise and insightful comparison of the occurrences of vertex divergences in different electron models, presented in [2], it was also inferred that the metal-insulator transition would have a crucial impact on the shape of the divergence lines.

The aim of this thesis is twofold: *(i)* we want to thoroughly investigate the non-perturbative aspects of the correlated metallic regime using a simpler model than the *Hubbard model*, which, however, still captures the physics of strongly correlated electrons. *(ii)* we want to clarify unambiguously the

role of the MIT for the occurrence of vertex divergences. For this reason the Anderson impurity model (AIM) is analysed, which while yielding a non-trivial description of a strongly renormalized Fermi-liquid, does not show any Mott transition at  $T = 0$ .

The study of the vertex divergences in the AIM will reveal, hence, whether the MIT plays a crucial role for the divergence lines. Further it will also clarify the importance of the Kondo scale [12], which marks the onset of the low-energy Kondo resonance, an essential ingredient of the low-energy physics of the strongly correlated metallic regime.

In a previous Projektarbeit [50] the first divergence line of the AIM was already calculated, revealing some unexpected features of the vertex divergences in the AIM. The emergence of a contradiction between these preliminary results and the interpretations given in the most recent publications [2] has inspired this Master thesis work. Here, the preceding study has been extended to the *whole* phase diagram of the AIM, allowing us to perform a systematic comparison with the corresponding results from other models. This way a definite progress in the understanding of the basic mechanisms controlling the irreducible vertex divergences in correlated systems could be achieved, providing some clear-cut answers about the validity of the interpretations proposed in the most recent scientific works on this topic.

# Chapter 2

## Introduction

*In this introductory chapter the theoretical framework used to analyse the vertex divergences is presented in detail, including precise definitions of the two-particle quantities under consideration. Subsequently a concise overview of the recent results presented in the literature concerning the understanding of irreducible vertex divergences in different many-electron models is given. Afterwards, an explicit definition of the specific Anderson model used throughout this thesis is provided. Eventually, the physics associated with the underlying Kondo scale is briefly reviewed, as it is of particular importance for the interpretation of the subsequent results.*

### 2.1 Formalism

In this work we are interested in phenomena occurring in strongly correlated systems. These systems are usually very hard to treat, as mean field theories do no longer apply, or give unsatisfying results. Quite generally, this reflects in the fact that the expectation value of two operators  $A$  and  $B$  can no longer be approximated by a product of expectation values of single operators:

$$\langle AB \rangle \neq \langle A \rangle \langle B \rangle, \quad (2.1)$$

Nevertheless, powerful methods have been developed in the course of the last 30 years to make predictions for correlated systems, even for the most complicated situations, where perturbation theory cannot be used. Among these we recall the Dynamical Mean-Field Theory (DMFT) [15, 16] and its cluster [17] and diagrammatic extensions [18, 19, 20, 21, 22]. In DMFT purely local correlation effects can be taken into account, due to the mapping of the lattice model treated within DMFT onto an auxiliary Anderson impurity

model. The treatment of non-local correlations is possible through the DMFT extensions, but it is not directly related to the work presented in this thesis.

In the following a short introduction to the formalism of quantum many-body theory on the two-particle level is given, as this provides the formal framework needed to analyse the irreducible vertex divergences, studied in this thesis. Note that the quantities defined here are purely local quantities, which completely describe the local (impurity) physics of the Anderson impurity model, defined in Sec 2.3.

### 2.1.1 Basic Definitions

All definitions given in this section are briefly mentioned in [2], and discussed in great detail in [13, 14]. For a more basic introduction, the reader is advised to the recent literature on this subject, e.g. [23, 24, 25].

As a starting point the one-particle Green's function is given [13, 14].

$$G_{1,\sigma_1\sigma_2}(\tau_1, \tau_2) = G_\sigma(\tau_1, \tau_2) = \langle T_\tau c_\sigma^\dagger(\tau_1) c_\sigma(\tau_2) \rangle \quad (2.2)$$

In the equation given above  $c_\sigma^\dagger(\tau)$  and  $c_\sigma(\tau)$  correspond to creation and annihilation operators of a fermion with spin  $\sigma$  created/annihilated at the imaginary time  $\tau$ , respectively.  $T_\tau$  represents the time-ordering operator, guaranteeing that the operator with the largest time acts first. The thermal expectation value  $\frac{1}{Z} \text{Tr} e^{-\beta \mathcal{H}} \mathcal{O}$  is denoted by  $\langle \mathcal{O} \rangle$ .

An intuitive picture for the one-particle Green's function given in Eq. 2.2 is the following: For  $\tau_1 > \tau_2$  a hole, created at the time  $\tau_2$  with spin  $\sigma$ , propagates through the system, from which it is removed at  $\tau_1$ . Along the path the hole probes the system, thus, the transition amplitude, given by the propagator  $G_\sigma$ , contains essential information about the intrinsic physical processes of the many electron system. The same picture is valid for  $\tau_1 < \tau_2$ , only that now an electron is propagating.

On the two particle level, one can also define a (local) Green's function, see Eq. 2.4, yet, the object usually examined, which is also of particular interest in our case, is the (local) generalized susceptibility<sup>1</sup>  $\chi_{\sigma_1\sigma_2\sigma_3\sigma_4}(\tau_1, \tau_2, \tau_3, \tau_4)$  defined as:

$$\begin{aligned} \chi_{\sigma_1\sigma_2\sigma_3\sigma_4}(\tau_1, \tau_2, \tau_3, \tau_4) &:= G_{2,\sigma_1\sigma_2\sigma_3\sigma_4}(\tau_1, \tau_2, \tau_3, \tau_4) \\ &- G_{1,\sigma_1\sigma_2}(\tau_1, \tau_2) G_{1,\sigma_3\sigma_4}(\tau_3, \tau_4) \end{aligned} \quad (2.3)$$

---

<sup>1</sup>Generalized here means that, if the four times are taken pairwise identical (e.g.  $\tau_1 = \tau_2 + 0^+$ ,  $\tau_3 = 0^+$ ), one could directly obtain expressions for the physical susceptibilities (see Eq. 2.13)

where  $G_{2,\sigma_1\sigma_2\sigma_3\sigma_4}(\tau_1, \tau_2, \tau_3, \tau_4)$  is given by

$$G_{2,\sigma_1\sigma_2\sigma_3\sigma_4}(\tau_1, \tau_2, \tau_3, \tau_4) = \langle T_\tau c_{\sigma_1}^\dagger(\tau_1) c_{\sigma_2}(\tau_2) c_{\sigma_3}^\dagger(\tau_3) c_{\sigma_4}(\tau_4) \rangle \quad (2.4)$$

Exploiting some general symmetries, such as the  $SU(2)$  symmetry, the crossing symmetry and the time invariance of the Hamiltonian, one can restrict the discussion of generalized susceptibilities to  $\chi_{\sigma\sigma'}(\tau_1, \tau_2, \tau_3) := \chi_{\sigma\sigma\sigma'\sigma'}(\tau_1, \tau_2, \tau_3)$  for  $\sigma = \uparrow, \downarrow$  and  $\tau_4 = 0$ . All other spin combinations vanish or can be extracted exploiting explicit algebraic relations [13, 14].

$\chi_{\sigma\sigma'}(\tau_1, \tau_2, \tau_3)$  can be Fourier transformed to Matsubara space in two different ways, which are known as *particle-hole* (*ph*) and *particle-particle* (*pp*) notation. The Matsubara frequencies are defined as  $\nu = (2n + 1)\pi T$  and  $\Omega = 2n\pi T$ , where  $\nu$  denotes a fermionic and  $\Omega$  a bosonic Matsubara frequency. Let us state already at this point that for all calculations performed throughout this thesis, and for those in the literature which are presented in Sec. 2.2,  $\Omega$  will be set to zero. This is done to perform comparisons of the results presented in this thesis to results of the literature, on one hand, but also because the irreducible vertex divergences appear, systematically, at lower interaction values for  $\Omega = 0$ , compared to cases for  $\Omega \neq 0$ . Yet, for the sake of generality, in this section  $\Omega$  is still included in the definitions given and set to zero in the following sections.

The two notations (*ph*) and (*pp*) are depicted in Fig. 2.1 (note that  $\omega$  corresponds to  $\Omega$  in our notation). Physically they describe the process of an electron scattering with a hole (*ph*-notation), see the left panel of Fig. 2.1, or two electrons scattering with one another (*pp*-notation), depicted in the right panel of Fig. 2.1. Summing the corresponding energies of the left and right sight of the diagrams, keeping in mind that holes are associated to negative energies, one finds that the transferred energy is equal to  $\Omega$  for both notations.



Figure 2.1: Left panel: particle-hole notation. Exploited to describe the scattering process of a hole and a particle. Right panel: two particles scattering with each other. In both cases the energy  $\Omega$  is transmitted during the process (in our notation  $\omega$  is equal to  $\Omega$ ). Taken from [13].

In the following equation the definition of the Fourier transformed gener-

alized susceptibility in  $ph$ -notation,  $\chi_{ph,\sigma\sigma'}^{\nu\nu'\Omega}$ , is given [13, 14].

$$\begin{aligned}\chi_{ph,\sigma\sigma'}^{\nu\nu'\Omega} &= \int_0^\beta d\tau_1 d\tau_2 d\tau_3 e^{-i\nu\tau_1} e^{i(\nu+\Omega)\tau_2} e^{-i(\nu'+\Omega)\tau_3} \\ &\times [\langle T_\tau c_\sigma^\dagger(\tau_1) c_\sigma(\tau_2) c_{\sigma'}^\dagger(\tau_3) c_{\sigma'}(0) \rangle \\ &- \langle T_\tau c_\sigma^\dagger(\tau_1) c_\sigma(\tau_2) \rangle \langle T_\tau c_{\sigma'}^\dagger(\tau_3) c_{\sigma'}(0) \rangle]\end{aligned}\quad (2.5)$$

The corresponding generalized susceptibility in  $pp$ -notation can be obtained from the one in Eq. 2.5 by a frequency shift, namely  $\chi_{pp,\sigma\sigma'}^{\nu\nu'\Omega} = \chi_{ph,\sigma\sigma'}^{\nu\nu'(\Omega-\nu-\nu')}$ . For the sake of conciseness, we restrict ourself to the  $ph$  case in the following. Let us also state here the relation of the susceptibility given here to the local physical susceptibility, given by

$$\chi_{ph,\sigma\sigma'}^{phys} = \frac{1}{\beta^2} \sum_{\nu\nu'} \chi_{ph,\sigma\sigma'}^{\nu\nu'\Omega=0} \quad (2.6)$$

The susceptibility given above can be split into a part accounting for the independent propagation of the two particles, the so called bubble term, and a part containing all vertex corrections. This yields the following relation [13, 14] :

$$\chi_{\sigma\sigma'}^{\nu\nu'\Omega} = \chi_0^{\nu\nu'\Omega} \delta_{\sigma\sigma'} - \frac{1}{\beta^2} \sum_{\nu_1\nu_2} \chi_0^{\nu\nu_1\Omega} F_{\sigma\sigma'}^{\nu_1\nu_2\Omega} \chi_0^{\nu_2\nu'\Omega} \quad (2.7)$$

In Eq. 2.7,  $\chi_0$  corresponds to the bubble term, which is given by a product of two Green's functions:

$$\chi_0^{\nu\nu'\Omega} = -\beta G_\sigma(\nu) G_\sigma(\nu + \Omega) \delta_{\nu\nu'} \quad (2.8)$$

$F_{\sigma\sigma'}^{\nu_1\nu_2\Omega}$ , denoted by  $F$  in the following, represents the vertex corrections to the generalized susceptibility, i.e., it comprises all possible scattering events between the two particles that propagate through the system. Diagrammatically, it corresponds to all connected two-particle diagrams, which can be further classified in terms of their two-particle reducibility [13, 14]: One can distinguish between *fully irreducible* and *reducible* two-particle diagrams. In this context reducibility means that the two-particle diagram falls apart, when cutting *two* internal Green's function lines. This is the natural extension of the concept of reducibility from the one-particle level to the two-particle case, discussed here <sup>2</sup>. Fully irreducible two-particle diagrams do not

<sup>2</sup>We recall that at the two-particle level *all* connected diagrams (i.e. all those belonging to  $F$ ), are - per construction - always one-particle irreducible.

fall apart when cutting two internal Green's function lines.

Reducible diagrams can be found in different ways, as Fig. 2.2 shows, where a generic reducible two-particle diagram is shown. Here the outer legs 1 and 3 represent outgoing particles, whereas 2 and 4 denote incoming particles. In Fig. 2.2, the outer legs 1 and 2 are disconnected from 3 and 4 by cutting two internal lines. Of course one may also think of other possible combinations. This leads to the following definitions: If the outer legs 1 and 3 are separable from 2 and 4, the diagram is called *particle-particle* reducible. In the specific situation depicted in Fig. 2.2 the diagram is *particle-hole longitudinal* ( $ph$ ) reducible. The remaining possibility of separating 1 and 4 from 2 and 3 is defined as *particle-hole transverse* ( $\overline{ph}$ ) reducible.

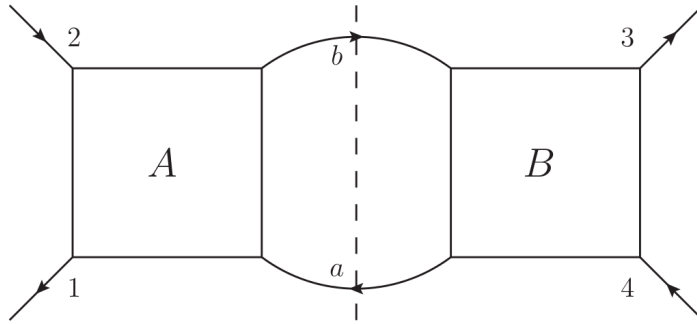


Figure 2.2: A generic two-particle diagram reducible in the longitudinal particle-hole channel, as it can be split by cutting the two internal Green's function lines  $a$  and  $b$ . 1 and 3 denote outgoing particles, whereas 2 and 4 represent incoming ones. Taken from [13].

Note that a two-particle diagram is either fully-irreducible or reducible in one of the channels defined above. This enables one to write down an exact relation for classifying the two-particle diagrams, which is known as the *parquet equation* [26]. This is depicted in Fig. 2.3, where  $\Phi_\rho$  denotes the reducible part in the corresponding channel  $\rho$  ( $pp$ ,  $\overline{ph}$  or  $ph$ ) and  $\Lambda$  the fully irreducible part.

From this classification it easily follows that one can express the contributions of  $F$  in respect of a specific channel, i.e.  $F = \Gamma_\rho + \Phi_\rho$ . Here  $\rho$  represents the desired channel ( $ph$ ,  $\overline{ph}$  or  $pp$ ) and  $\Gamma_\rho$  all diagrams that are irreducible in this specific scattering channel  $\rho$ .

$\Gamma_\rho$ , the irreducible vertex, is the crucial object of interest for this thesis. Hitherto, we have considered the definition for the "spinless" case. Yet, if the spin is explicitly considered, specific spin combinations are of particular

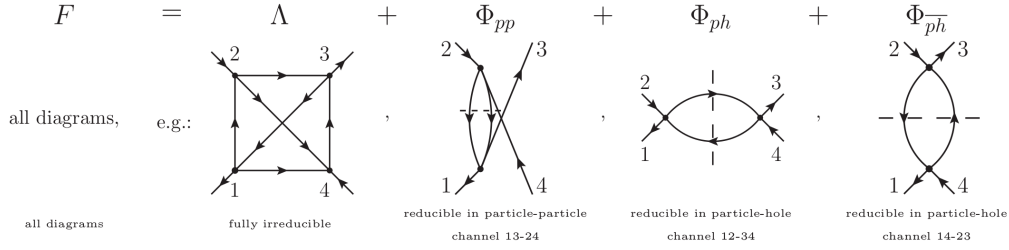


Figure 2.3: The parquet equation, an exact relation for the connected two-particle diagrams, depicted in an algebraic notation, with a low order diagrammatic example for each class. Taken from [13].

importance, which are given below

$$\Gamma_c^{\nu\nu'\Omega} = \Gamma_{ph,\uparrow\uparrow}^{\nu\nu'\Omega} + \Gamma_{ph,\uparrow\downarrow}^{\nu\nu'\Omega} \quad c = \text{charge channel} \quad (2.9)$$

$$\Gamma_s^{\nu\nu'\Omega} = \Gamma_{ph,\uparrow\uparrow}^{\nu\nu'\Omega} - \Gamma_{ph,\uparrow\downarrow}^{\nu\nu'\Omega} \quad s = \text{spin channel} \quad (2.10)$$

$$\Gamma_{pair}^{\nu\nu'\Omega} = \Gamma_{pp,\uparrow\downarrow}^{\nu(\Omega-\nu')\Omega} - \Gamma_{pp,0}^{\nu\nu'\Omega} \quad \text{pair channel} \quad (2.11)$$

$$\Gamma_{pp,\uparrow\downarrow}^{\nu\nu'\Omega} = \Gamma_{ph,\uparrow\downarrow}^{\nu\nu'(\Omega-\nu-\nu')\Omega} \quad (2.12)$$

and hereinafter compactly denoted by  $r$  in the case of the charge, the spin and the pair channel. The particle-particle up-down channel will always be explicitly stated. They represent the channels where fluctuations related to physical processes can occur. Note that for  $\chi_{ph,\sigma\sigma'}^{\nu\nu'\Omega}$  and  $F$  the same relations hold. Let us also state here the relation of  $\chi_c^{\nu\nu'\Omega=0}$  to the physical local charge susceptibility, given by [9]

$$\chi_{ch} = \frac{1}{\beta^2} \sum_{\nu\nu'} \chi_c^{\nu\nu'\Omega=0} \quad (2.13)$$

$\Gamma_r$  is connected to objects introduced so far by the Bethe-Salpeter equation, given in the following [2]

$$\pm \chi_r^{\nu\nu'\Omega} = \chi_{r,0}^{\nu\nu'\Omega} - \frac{1}{\beta^2} \sum_{\nu_1\nu_2} \chi_{r,0}^{\nu\nu_1\Omega} \Gamma_r^{\nu_1\nu_2\Omega} \chi_r^{\nu_2\nu'\Omega} \quad (2.14)$$

The + sign corresponds to the charge and spin channel, – to the pair one<sup>3</sup>. Eq. 2.14 is depicted in a diagrammatic way in Fig. 2.4, where it naturally occurs that the Bethe Salpeter equation can be viewed, to some extent, as the two-particle analogon of the Dyson equation.

<sup>3</sup>The corresponding Bethe Salpeter equation of the particle-particle up-down channel can be found in the appendix of [13, 14].



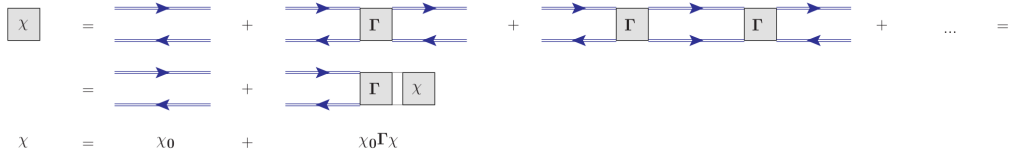


Figure 2.4: Bethe Salpeter equation depicted diagrammatically where the blue double lines represent the Green’s function. Taken from [2].

### 2.1.2 Divergences of the Irreducible Vertex

When considering two-particle vertex functions (which are matrices in frequency/momentum space) a variety of divergences can occur (in fact, working with matrices gives more ”freedom”, than in the case of the self-energy). It is important, then, to discuss first of all some general features of the vertex divergences and their connection to the work presented in this thesis.

All vertices defined in the previous section ( $F, \Gamma, \Lambda$ ) can diverge. For instance, this is the case for the full vertex  $F$ , which is defined above as the representation of all connected two-particle diagrams. This divergence takes place along the diagonal of  $F$ , if expressed as a matrix of the fermionic Matsubara frequencies. The diagonal elements of this matrix are proportional to  $U^2$  times the physical susceptibility, containing, thus, two-particle reducible processes. Hence, such a divergence of  $F$  is connected to a physical phase transition.

Here, however, we are interested in the investigation of the more subtle irreducible vertex divergences, i.e. divergences of  $\Gamma$  in a given channel. Interestingly, in such a case, the full vertex  $F$  does not diverge. This feature is depicted in Fig. 2.5, which shows a DMFT calculation for the *Hubbard model* for two interaction values, lower and higher than the corresponding interaction value where the irreducible vertex divergence takes place. In the first row  $F$  is depicted showing no divergence.  $\Gamma_c$  on the other hand, depicted in the next row, displays a low-frequency divergence. Due to the fact that  $\Gamma_c$  diverges but  $F$  stays finite  $\Lambda$  has to diverge as well, to compensate for the divergence of  $\Gamma_c$ . This can be seen in the last row of Fig. 2.5.

One can analyse the onset of irreducible vertex divergences from two different perspectives, namely (i) by considering the inversion of the Bethe-Salpeter equation or (ii) through a functional derivative of the self-energy functional, as it will be explained in detail in the following [2].

Inverting the Bethe Salpeter equation, here given in a matrix representation (indicated by the bold characters), leads to the following expression. Note that this short part was already discussed in a preceding *Projektarbeit*

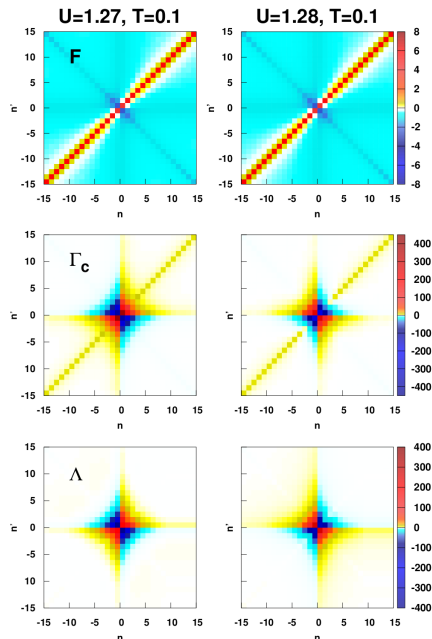


Figure 2.5: First row: the (local) full vertex  $F^{\nu\nu'\Omega=0}$  of the Hubbard model, depicted in a Matsubara frequency density-plot, obtained from a two-particle DMFT calculation.  $F$  shows no particular features across this low-frequency divergence of  $\Gamma_c$ , which is depicted in the second row. To compensate for the divergence, i.e. for  $F$  to stay finite,  $\Lambda$  also shows a low-frequency divergence. Taken from [2].

[50] in great detail, but as this is of high relevance for this work, it is given here again.

$$\pm \mathbf{\Gamma}_r = \beta^2 \left( [\chi_r]^{-1} - [\chi_{r,0}]^{-1} \right) \quad (2.15)$$

Note that  $\Omega$  is now set to 0 and omitted hereinafter, as discussed in the section above.

From Eq. (2.15) it can be easily seen that, although we are working in Matsubara frequency space, divergent contributions in  $\mathbf{\Gamma}_r$  can indeed arise from a singular generalized susceptibility  $\chi_r$ , while  $\chi_{r,0}$  does typically not pose any problem, being merely a product of two Green's functions<sup>4</sup>.

In Eq. (2.16) the spectral representation of the generalized susceptibility is given.  $\lambda_i$  is the eigenvalue and  $V_{i,\nu}$  the corresponding eigenvector. From

<sup>4</sup>For the case of  $\nu \rightarrow \infty$  the Green's function will be equal to zero, inducing a singular  $\chi_{r,0}$ , which is of course never reached in our numerical calculations. Also one might think of a zero of the Green's function at frequency zero in the Mott insulating phase, however this could only be seen in a calculation at  $T = 0$ .

Eqs. (2.15) and (2.16) one can easily understand, that a divergence in  $\mathbf{\Gamma}_r$  corresponds mathematically to a singular (i.e. vanishing) eigenvalue of  $\chi_r$ .

$$[\chi_r]_{\nu\nu'}^{-1} = \sum_i (V_{i,\nu'})^* (\lambda_i)^{-1} V_{i,\nu} \quad , \quad (2.16)$$

$\mathbf{\Gamma}_r$  diverges, if one or more  $\lambda_i = 0$  for  $i = k_1, k_2, \dots$ . The way how the vanishing on an eigenvalue  $\lambda_{k_j}$  leads to divergent contributions in  $\mathbf{\Gamma}_r$  is connected to the frequency structure of the corresponding eigenvector  $V_{k_j,\nu}$ . Specifically, if the eigenvector is localized in frequency, e.g. a combination of delta functions, the divergence in  $\mathbf{\Gamma}_r$  can only be observed at frequencies for which  $V_{k_j,\nu} \neq 0$  holds. This means that for a finite set of frequencies  $\mathbb{D}$  a local divergence of  $\mathbf{\Gamma}_r$  takes place [2].

In the other case of  $V_{k,\nu} \neq 0$  for all frequencies,  $\mathbf{\Gamma}_r$  diverges globally.

This means that two different kinds of irreducible vertex divergences can be expected.

### Luttinger Ward formalism

The other possibility of treating irreducible vertex divergences is to extract the irreducible vertex function as the functional derivative of the self-energy functional with respect to the Green's function, in the context of a very general theoretical formalism, the Luttinger-Ward formalism [27, 28, 29].

In this framework, the static and dynamic properties of a system of correlated electrons can be calculated by using the so called Luttinger-Ward functional  $\Phi$  [29]. This is related to the grand potential, from which, in turn, thermodynamical (static) properties can be derived. Further, the following relation holds

$$\beta \frac{\delta \Phi[G]}{\delta G} = \Sigma[G] \quad , \quad (2.17)$$

with  $\Sigma[G] = \Sigma$  if  $G$  is exact, relating  $\Phi$  to dynamic properties of the system. The Luttinger-Ward functional  $\Phi[G]$  is unique, i.e. it only depends on the interaction term of the Hamiltonian. This in turn means that for several models, such as the Hubbard model and the Hubbard atom the functional is the same. The problem is that  $\Phi[G]$  can not be obtained in a closed form. It can be, however, calculated by a diagrammatic weak-coupling perturbation expansion as the limit of an infinite series of skeleton diagrams [29], or non-perturbatively using a functional-integral approach as proposed by [28].

The Luttinger-Ward functional came to great popularity in the field of quantum many-body physics, because it could be shown that the so called

” $\Phi$ ”-derivable approximations automatically fulfill several macroscopic conservation laws, where  $\Phi$ -derivable means that a given (approximative) expression for the Luttinger-Ward functional is the starting point for calculating simultaneously one- and two-particle quantities (i.e., both  $\Sigma$  and  $\Gamma_r$ ) [30].

For our purposes, however, the important aspect is that the Luttinger-Ward formalism can also be used to calculate  $\Gamma_r$ , as the functional derivative of the self-energy functional  $\Sigma[G]$  with respect to  $G$ . Yet, as we are dealing with functional derivatives, it is in principle necessary to introduce symmetry breaking fields to perform such a calculation. This of course prevents the possibility to obtain  $\Gamma_r$  analytically for many cases, such as the Hubbard model and the Anderson impurity model. In very simple cases of disordered systems, though, the introduction of symmetry breaking fields is not necessary, enabling the calculation of the vertex function analytically. More precisely, for these simpler systems, a normal derivative of  $\Sigma$  with respect to the Green’s function can be done by exploiting the possibility of writing analytic expressions for  $\Sigma$  in terms of  $G$  [2].

$$\Gamma_{\sigma\sigma'}^{\nu\nu'\Omega=0} = \beta \frac{\delta\Sigma_{\sigma}(\nu)}{\delta G_{\sigma'}(\nu')} \quad (2.18)$$

We should, however, stress that, although the latter is possible also for the atomic limit case, the simplification of neglecting the introduction of symmetry breaking fields is no longer valid.

## 2.2 Overview of the recent developments

In this section a short overview of the recent developments and results concerning the irreducible vertex divergences for various models is provided. In this respect it is useful to start from a Hamiltonian, encoding all models under consideration [2].

$$\mathcal{H} = - \sum_{\langle i,j \rangle, \sigma} t_{\sigma} c_{i\sigma}^{\dagger} c_{j\sigma} + \sum_{i, \sigma} \epsilon_i c_{i\sigma}^{\dagger} c_{i\sigma} + U \sum_i n_{i\uparrow} n_{i\downarrow} \quad (2.19)$$

The first term is the nearest neighbour hopping term with  $t_{\sigma}$  being the hopping amplitude between nearest neighbouring lattice sites  $i$  and  $j$  for the electron species with spin  $\sigma = \uparrow, \downarrow$ . The second term contains a random external potential  $\epsilon_i$  and the last term is an instantaneous and local interaction term with a coupling strength parameter  $U$ .

## 2.2.1 Disordered Models

As a first step, disordered models, such as the *Binary Mixture* and the *Falicov-Kimbal* model are analysed [2, 31].

The *Binary Mixture* model is realized by making the following choice of parameters in Eq. 2.19:  $t_{\uparrow} = t_{\downarrow} = t$ ,  $U = 0$  and  $\epsilon_i = \pm W/2$ . This means that the electrons can hop between neighbouring lattice sites but there is no interaction among them. At the same time, the randomly distributed potential  $\epsilon_i$  acts, to a loose extent, as a strongly simplified interaction term.

As already discussed in Sec. 2.1, for simple situations the irreducible vertex can be obtained analytically as a functional derivative of the self-energy with respect to the Green's function [2].

Following [2], and exploiting the semi-analytical expression of the DMFT Green's function available for the *Binary Mixture* case, one obtains a single valued self-energy functional of the non-interacting Green's function  $G_0$ , but interestingly a multivalued functional of the Green's function  $G$ .

$$\Sigma^{\pm}[G] = \frac{\pm\sqrt{1+W^2G^2}-1}{2G} \quad \text{and} \quad \Sigma[G_0] = \frac{W^2}{4}G_0 \quad (2.20)$$

Note that the frequency argument of the Green's function is omitted. A multivalued self energy functional is a very surprising result, as will be discussed in the following section.

The next step is the calculation of the irreducible vertex, which for this case is irreducible in the charge channel (for the *Binary Mixture* case the charge channel is defined as  $\Gamma_c = \Gamma_{\uparrow\uparrow}$ ).

$$\Gamma_{c,\pm}^{\nu\nu'(\Omega=0)} = \beta\delta_{\nu\nu'} \frac{\sqrt{1+W^2G^2} \mp 1}{2G^2\sqrt{1+W^2G^2}} \quad (2.21)$$

Note that throughout this overview and the rest of the thesis the bosonic transport frequency  $\Omega$  is set to zero, as already explained in Sec. 2.1. The  $\pm$  in  $\Gamma_c$  reflects a multivaluedness of  $\Sigma[G]$ .

In fact, it is easy to see that as soon as  $1+W^2G^2 = 0$  holds, the irreducible vertex diverges. Inserting the explicit expression for the Green's function into this condition, one can identify a unique energy scale, underlying all vertex divergences, as

$$\nu^* = \frac{2W^2-1}{4W}. \quad (2.22)$$

As soon as a fermionic Matsubara frequency  $\nu$  is equal to this scale, the condition  $1+W^2G^2 = 0$  will hold and the vertex, given in Eq. 2.21, will diverge at exactly this frequency. This also means that the vertex divergences

in the *Binary Mixture* model are frequency localized divergences. By performing this analysis for different temperatures and disorder strengths, one finds divergence lines, along which the irreducible vertex diverges. The corresponding phase diagram is depicted in Fig. 2.6, and shows a rather non-trivial situation: At  $T = 0$  the divergence lines accumulate at a disorder strength ( $W = 1/\sqrt{2}$ ) which is *lower* than the value of the "Mott" metal-insulator transition of this model ( $W = 1$ ) [2].

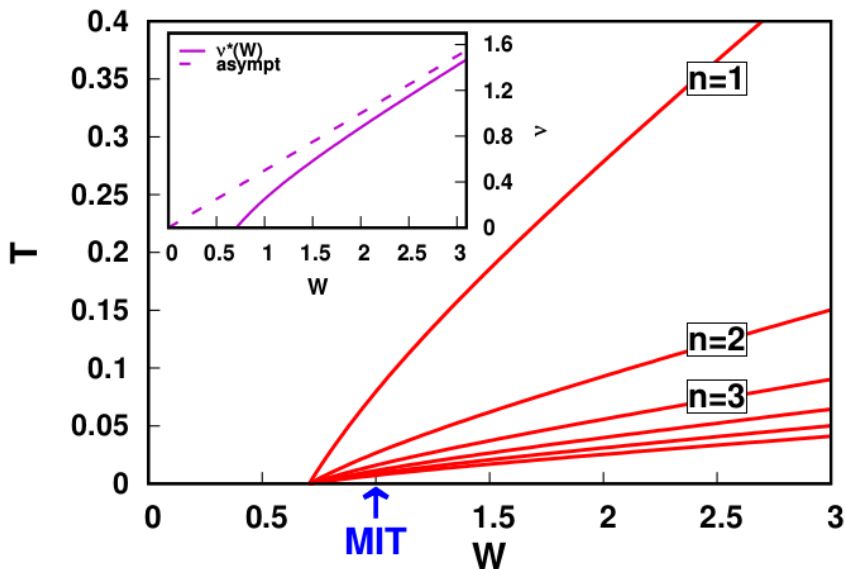


Figure 2.6: Phase diagram of the *Binary Mixture* model, depicting divergence lines, along which the irreducible vertex in the "charge" channel diverges. Remarkably, these lines accumulate well before the Mott transition of the *Binary Mixture* model. In the inset the energy scale  $\nu^*$ , underlying all the divergences, is shown. Taken from [2].

Due to the existence of a single energy scale  $\nu^*$  and the local frequency structure of the above given relations, it is possible to identify each divergence line with a single Matsubara frequency (marked by the indices in the boxes in Fig. 2.6). This can be easily understood, if one imagines to decrease the temperature at a fixed  $W$ . The first Matsubara frequency to fulfill the relation  $(2n - 1)\pi T = \nu = \nu^*$  will be the one with  $n = 1$ . Decreasing the temperature further, other divergences corresponding to the fulfilment of the condition  $(2n - 1)\pi T = \nu = \nu^*$  for progressively larger (integer) values of  $n$  are found. This evidently implies that (i) infinitely many divergences take place and that (ii) the divergence lines can be rescaled by a factor  $(2n - 1)$ ,

which let them collapse onto a single line.

The situation described here is quite similar to the slightly more complex case of the *Falicov Kimball* [31] model. Here, one spin species is frozen and hence, the corresponding electrons act as "scattering centers" for the mobile spin-species electrons. This can be realized in Eq. 2.19 if the parameters are chosen such that  $t_{\uparrow} = t$ ,  $t_{\downarrow} = 0$ , the random potential  $\epsilon_i$  is put to zero, and  $U > 0$ .

Starting from the DMFT Green's function for the mobile electrons, which is exactly the same as in the *Binary Mixture* case, one finds again a multivalued self-energy functional. However, at the two-particle level, the differences between the two models emerge, as in the *Falicov Kimball* case the external scattering potential is not assigned from the beginning, but it is induced by the immobile electrons, which are in thermal equilibrium with the mobile ones. This yields a richer structure of the vertex function, as given in the following, and a new kind of vertex divergence [2].

$$\begin{aligned} \Gamma_{c,\pm}^{\nu\nu'(\Omega=0)} &= \beta\delta_{\nu\nu'} \frac{\sqrt{1+U^2G^2(\nu)} \mp 1}{2G^2(\nu)\sqrt{1+U^2G^2(\nu)}} \\ &+ \beta \frac{U^2}{4} C_{\pm} \frac{1}{\sqrt{1+U^2G^2(\nu)}} \frac{1}{\sqrt{1+U^2G^2(\nu')}} \end{aligned} \quad (2.23)$$

where

$$C_{\pm} = \frac{1}{1 - K_{\pm}}, \quad K_{\pm} = \sum_{\nu} \frac{\sqrt{1+U^2G^2} \mp 1}{2\sqrt{1+U^2G^2}} \quad (2.24)$$

Comparing the result for the irreducible vertex function in the charge channel with Eq. 2.21, one immediately realizes that the first term is exactly the same as in the *Binary Mixture* case for  $U = W$ . This of course implies that a similar scenario as above is realized, i.e. a single energy scale  $\nu^*$  exists causing infinitely many divergence lines along which the vertex diverges locally at the Matsubara frequency which is equal to the energy scale.

The second term, which is originated by taking the functional derivative with respect to the thermally averaged density of the immobile electrons, see [2], diverges also where the first kind of divergences take place, but one can also see that for  $K_{\pm} = 1$  the coefficient  $C_{\pm}$  diverges. This leads to a *global* divergence taking place at all Matsubara frequencies. In this case, no single energy scale can be identified and following the discussion made in Sec. 2.1, it can be seen that the corresponding singular eigenvectors have finite weight at all Matsubara frequencies.

## 2.2.2 Atomic Limit of the Hubbard Model

After discussing disordered models we now turn one step closer to the *Hubbard model* by analysing the atomic limit of the latter. For the *Hubbard atom* only two energy scales are of importance, i.e. the interaction  $U$  and the temperature  $T$ : In Eq. 2.19 the hopping amplitude is set to zero as well as the potential  $\epsilon_i$ .

Although the one-particle Green's function is similar to the *Binary mixture/Falicov-Kimball* one, the divergences of  $\Gamma$  can no longer be calculated by the functional derivative procedure used above for the simpler cases of disordered models. As discussed in Sec. 2.1, the alternative is to analyse the eigenvalues of the generalized susceptibility, which for the Hubbard atom is known analytically [2, 13, 14].  $\chi_c^{\nu\nu'}$  consists of three contributions: (i) depending on  $\nu^2$  and  $\nu'^2$ , (ii) proportional to  $\delta_{\nu\nu'}$  and (iii) depending on  $\delta_{\nu(-\nu')}$ . By applying  $\chi_c^{\nu\nu'}$  to an antisymmetric eigenvector of the form

$$V_{c,\bar{\nu}}(\nu) = \frac{1}{\sqrt{2}}[\delta_{\nu\bar{\nu}} - \delta_{\nu(-\bar{\nu})}], \quad (2.25)$$

all symmetric contributions will disappear, simplifying the extraction of the eigenvalues of the remaining contributions. Note that the frequency structure of the antisymmetric eigenvector in Eq. 2.25 is completely localized, as it only consists of two delta functions evaluated at a fixed fermionic frequency  $\bar{\nu}$ . The extraction of eigenvalues can be further simplified by using symmetry relations, which is presented in detail in [2]. Here, only the condition for a vanishing of an eigenvalue is recalled:

$$\bar{\nu} = \frac{\sqrt{3}}{2}U, \quad (2.26)$$

where  $\bar{\nu}$  is the fixed fermionic frequency.

This defines an energy scale  $\nu^*$  implying similar properties of the vertex divergences and the divergence lines as for the *Binary Mixture* and for the first kind of divergences of the *Falicov Kimball* model. The difference is the linear relation with  $U$  which causes the lines to accumulate at the origin. This difference reflects the missing hopping term in the *Hubbard atom* and the corresponding appearance of a spectral gap down to  $U = 0^+$ . Also note that the limit of large  $U$  for  $W = U$  in Eq. 2.22 is not compatible with the results found for the *Hubbard atom* ( $\nu_{BM}^*(W = U \ll 1) = U/2$ ). The phase diagram for the *Hubbard atom* is given in Fig. 2.7, displaying the divergence lines corresponding to the energy scale  $\nu^*$  in red color.

In Fig. 2.7, a second kind of divergence is also depicted. As in the case of the second kind of divergences of the *Falicov Kimball* model these divergences



take place at all Matsubara frequencies, and, thus, no single energy scale can be found. Interestingly, along the orange lines in Fig. 2.7 not only the irreducible vertex in the charge channel but also  $\Gamma_{pair}$  diverges globally for the *Hubbard atom* as opposed to the *Falicov Kimball* model. The corresponding singular eigenvector is given in [2].

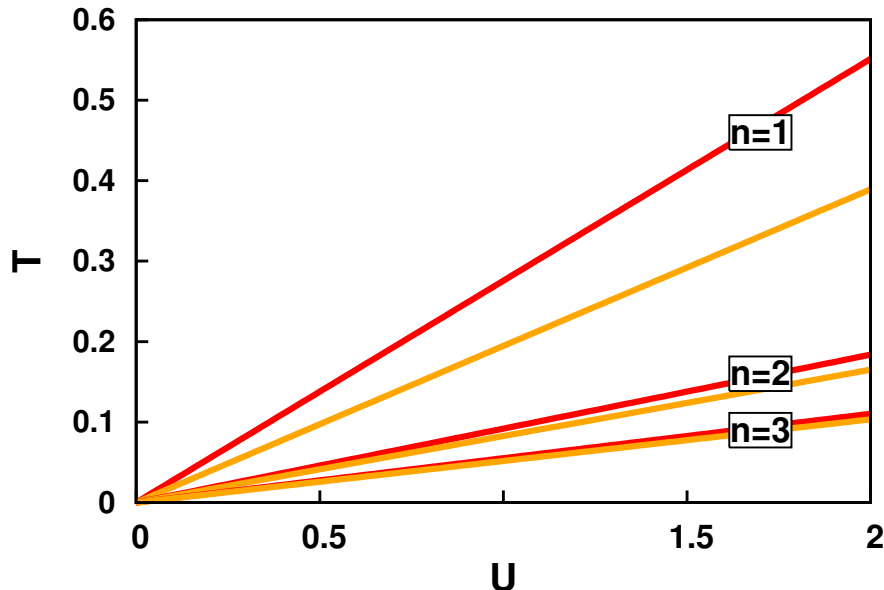


Figure 2.7: Phase diagram of the *Hubbard atom* displaying two different kinds of irreducible vertex divergences. Depicted in red are the purely local divergences in the charge channel, which correspond to the energy scale  $\nu^* = \frac{\sqrt{3}}{2}U$ . Along the orange lines, instead the vertex diverges globally in the charge and the pair channel simultaneously. Taken from [2]

### 2.2.3 Hubbard Model

After analysing simpler models, where the irreducible vertex divergences are accessible analytically, via a functional derivative for disordered models or the analysis of the eigenvalues of the analytically known generalized susceptibility in the case of the *Hubbard atom*, we now discuss the case of the *Hubbard model*, or, more precisely its DMFT solution. For the Hamiltonian in Eq. 2.19, this implies the following parameter choice:  $t_{\uparrow} = t_{\downarrow} = t$ ,  $\epsilon_i = 0$  and  $U > 0$ . Due to the complexity of the *Hubbard model* the vertex divergences are to be studied numerically in DMFT, by extraction of the eigenvalues of the generalized susceptibilities.

In Fig. 2.8 the DMFT results for the half-filled *Hubbard model* are depicted. Along the red divergence lines the irreducible vertex in the charge channel diverges, along the orange lines a simultaneous divergence in the charge and the particle-particle up-down channel takes place. The dashed red and orange line in Fig. 2.8 represent the corresponding results for the first red and orange line of the *Hubbard atom*. Note that the ratios of  $U/T$  for all divergence lines of the *Hubbard atom* are also listed on the right side of the figure. The blue line corresponds to the metal-insulator transition of the Hubbard model, as predicted by DMFT.

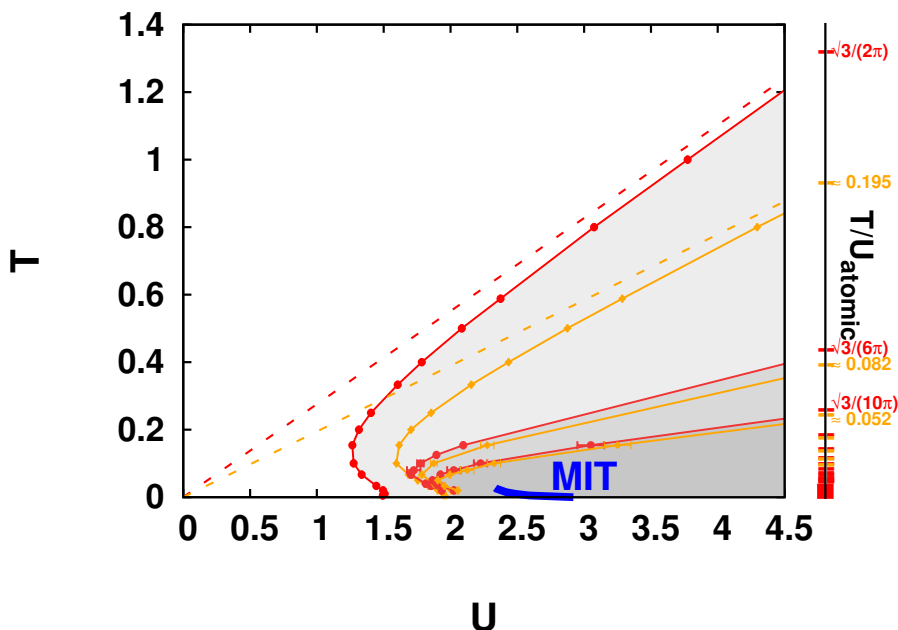


Figure 2.8: Phase diagram of the *Hubbard model* showing the divergences of the irreducible vertex functions. Along the red lines the charge channel diverges, whereas along the orange lines a simultaneous divergence in the charge and the particle-particle up-down channel takes place. The blue line corresponds to the metal-insulator transition, the dashed lines and values listed on the right represent the corresponding results obtained for the *Hubbard atom*. Taken from [2]

Studying this specific manifestation of non-perturbative physics, one notices that for high- $T$  and large  $U$  the results of *all* considered models have qualitatively the same behaviour. The divergence lines of the *Hubbard model* can even be interpreted quantitatively in terms of the results of the *Hubbard atom* in this parameter regime. The lines show a linear behaviour, the eigenvector has a localized frequency structure and from this comparison, and in

particular, from the existence of infinitely many divergence lines in the *Hubbard atom* (see the ratios  $U/T$  on the right side in Fig. 2.8), it logically follows that infinitely many divergences must be expected also in the *Hubbard model* [2].

Yet, following the divergence lines towards lower temperatures significant deviations from the *Hubbard atom* behaviour are found. At first, the lines show a non-linear behaviour, qualitatively similar as that observed in the *Binary mixture* and *Falicov Kimball* model. This might be ascribed to small corrections stemming from the finite hopping value. Still, this comparison may be misleading, due to an important difference rooted in the corresponding eigenvectors. As it can be seen in Fig. 2.9, where the corresponding singular eigenvectors of the first red divergence line for different temperatures for the *Hubbard model* are shown, the frequency structure of the eigenvector changes drastically. With decreasing  $(U, T)$  the frequency structure of the eigenvector broadens, an effect that was absent in the case of the disordered models.

Reducing the temperature further, by following the divergence lines the strongly correlated metallic regime is reached. Here, the divergence lines show a so far unobserved behaviour. Not only do the divergence lines no longer accumulate at  $T = 0$ , they also show a re-entrance, i.e. a bending towards higher interaction values, as if the perturbative low-temperature regime were to some extent "protected" against this non-perturbative manifestation. This is supported by the fact that a Kondo resonance, which enables a Fermi-liquid description in terms of low-energy quasiparticle excitations, appears at low temperatures, as opposed to the models considered so far [2]. Further it is inferred in [2] that the Mott transition plays a crucial role for the shape of the divergence lines.

In a recent work [5] irreducible vertex divergences were also found in a DCA calculation of the two-dimensional *Hubbard model*, which demonstrates that this phenomenon is not merely an artefact of DMFT <sup>5</sup>.

To summarize, the analysis recapitulated so far shows the existence of infinitely many divergence lines in the phase diagram of many-body model systems. For disordered models and the *Atomic Limit* they could be related to a single energy scale  $\nu^*$ , governing the shape of the divergence lines and the frequency structure of the divergences of  $\Gamma_c$  (for the first kind of divergences of

---

<sup>5</sup>While this topic is beyond the scope of this thesis, we note here that the inclusion of non-local correlations determines in general a loss of metallic coherence, which is reflected in a shift of the divergences towards lower interaction values. Moreover, in the case of exact diagonalization (see Sec. 3.2), it has been shown that the momentum structure of the divergences and of their singular eigenvectors become as (if not more) important as their frequency structure.

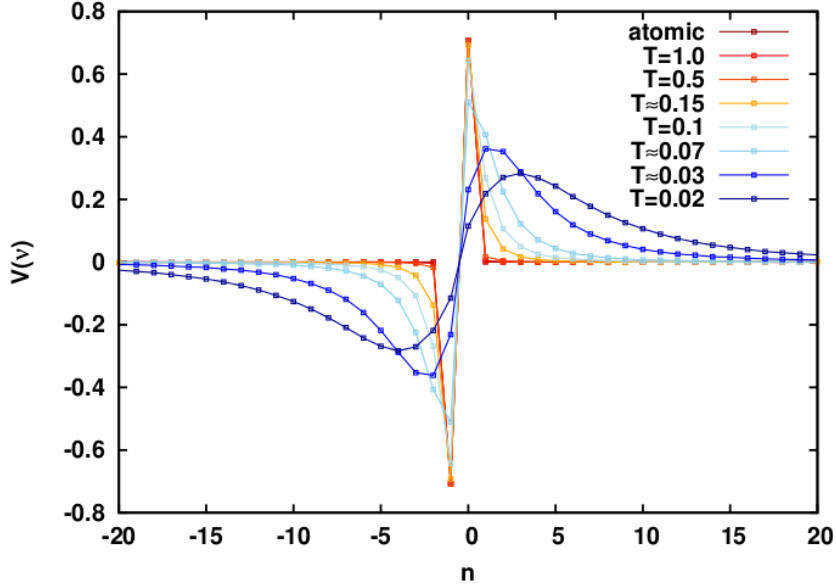


Figure 2.9: Eigenvectors of the first red divergence line of the *Hubbard model* for different temperatures expressed in the basis of the Matsubara index  $n$ . In red the result for the highest temperature is depicted, where the eigenvector shows a localized frequency structure as is the case for the eigenvectors of the atomic limit. By reducing the temperature the components of the eigenvector at an increasingly large number of Matsubara frequencies gain finite weight, leading to a "broadening" of the frequency structure of the eigenvector. Taken from [2]

the *Falicov Kimball* model and the *Hubbard atom*). In particular, for models with a metal-insulator transition, it turned out that these divergences take place always *before* the transition, in the (correlated) metallic phase.

Additionally, a second kind of divergence was found, which is not related to a single energy scale, as this takes place at all Matsubara frequencies simultaneously (a *global* divergence of the irreducible vertex). This second kind of divergences in general appears always after the one of the first kind.

## 2.2.4 Implications at the one-particle level

Returning to the discussion of Eq. 2.20 of the *Binary Mixture* model, where a multivaluedness of the self-energy functional, if expressed as a functional of the interacting Green's function  $G$ , was observed, we will discuss now the corresponding implications at the one-particle level.

In Fig. 2.10, the self-energy for two different values of the disorder strength  $W$  is depicted. The left panel shows the situation for the temperature  $T = 0.002$  and  $W = 0.65 < \widetilde{W} = 1/\sqrt{2}$ , with  $\widetilde{W}$  being the disorder strength value at which the vertex divergences accumulate at  $T = 0$ , meaning that at this  $W$  no divergence has taken place yet. The calculations of [2] have shown that, for these parameters, the physical self-energy is always given by one of the solutions of Eq. 2.20,  $\Sigma^+$ , which is agreeing with the predictions of perturbation theory, as opposed to  $\Sigma^-$  which has a non-perturbative asymptotic behaviour. Conversely, for disorder strengths  $W > \widetilde{W}$ , the situation is different, as it can be seen in the right panel of Fig. 2.10. In the low-frequency range the physical self-energy is given by  $\Sigma^-$  and changes abruptly at the energy scale  $\nu^*$  to the perturbative  $\Sigma^+$  branch. Quite remarkably, at the frequency where this change of branches of the physical self-energy occurs, i.e. at the energy scale  $\nu^*$ , the imaginary part of the one-particle Green's function as a function of Matsubara frequencies displays a *minimum*. From this it evidently follows that the occurrence of vertex divergences and the multivaluedness of the self-energy is closely related to the spectral gap formation, at least for the *Binary Mixture* model [2]. We also note that, in this specific case, the abrupt changing of branches can also be observed for the two-particle quantities, as discussed in [2].

After considering the implications of vertex divergences at the one-particle level for the *Binary Mixture* model, we now turn to the case of the *Hubbard atom*.

In a recent, pioneering, publication by Kozik [6] it was observed that diagrammatic Monte-Carlo algorithms, which sum skeleton diagrams of the interacting Green's function  $G$ , run into unphysical solutions, although the diagrammatic series has converged (in the work the case of the *Hubbard atom* was explicitly considered). Mathematically, this indicates that only a "simple", but not an "absolute", convergence of the diagrammatic series could be found. This poses, evidently, a serious problem to these methods, as no criterion was identified to decide whether the diagrammatic series converges to the physical solution or not.

At the same time, this ambiguity can be recasted in the statement that the mapping  $G_0 \rightarrow G$  is not invertible for interacting systems, as originally anticipated. On a more theoretical level this is a discomfoting result as in the Luttinger Ward formalism the existence of a unique mapping is somehow implicitly assumed. Thus, a lack of uniqueness might lead to an ill-defined Luttinger Ward functional, which, in turn, is crucial for guaranteeing that the chosen approximation is "conserving", i.e. consistent with fundamental physical conservation laws [30].

More recently, Gunnarsson *et.al.* [9] could demonstrate rigorously the

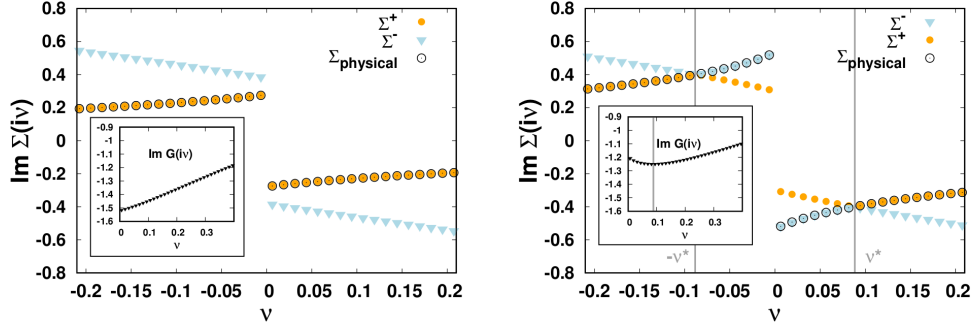


Figure 2.10: Imaginary part of the physical self-energy shown together with the two solutions of Eq. 2.20 for  $T = 0.002$  and two different values of the disorder strength  $W$ .  $\Sigma^+$  corresponds to a solution of Eq. 2.20, agreeing with perturbation theory, as opposed to  $\Sigma^-$ . In the left panel, the disorder strength is lower than  $\widetilde{W}$ , implying that no divergence has taken place so far. Here, the physical self-energy corresponds for all frequencies to the perturbative one, i.e.  $\Sigma = \Sigma^+$ . For  $W > \widetilde{W}$  this is no longer the case: For low frequencies the physical self-energy is given by  $\Sigma^-$  changing abruptly to  $\Sigma^+$  at the energy scale  $\nu^*$ , which is related to the vertex divergences. The insets show the imaginary part of the Green's function as a function of Matsubara frequencies, which has a minimum exactly at  $\nu^*$ . Taken from [2]

connection of this "phenomenon" to the irreducible vertex divergences described above. In fact, the study in [9] has shown that infinitely many unphysical  $G_0$  solutions exist in the functional space of the interacting model, which for specific parameters cross the physical one. This means that for a given temperature  $T$  and interaction  $U$  the two functions  $G_{unphys}^0(\nu)$  and  $G_{phys}^0(\nu)$  are exactly equal for all Matsubara frequencies. At such a crossing an irreducible vertex divergence takes place, which could be proven analytically [9] (see supplemental material, section A). Moreover, the functional dependence on  $U$  at the crossing determines the frequency structure of the corresponding singular eigenvector and thereby if the vertex divergence is global or localized in frequency. The situation is depicted in Fig. 2.11, where, in the left panel, the double occupancy ( $\text{Tr}G\Sigma$ ) and in the right panel the crossing of physical and unphysical solutions is depicted. For the red lines at a single frequency the crossing of the physical and unphysical Green's functions is linear with  $U$ , whereas at all other frequencies it is quadratic with  $U$ . This can be seen in the right panel of Fig. 2.11, especially in the inset showing the red lines. The one frequency where the linear crossing is observed is also the frequency

where the singular eigenvector has finite weight. In the case of the orange lines the crossing happens for all frequencies with the same behaviour. In the left panel of Fig. 2.11 it can be seen that double occupancies calculated with unphysical Green's functions cross the physical one for specific parameters. The unphysical double occupancies increase with higher  $U$ . The crossing of these solutions bears, evidently, the danger for an algorithm, based on the resummation of dressed diagrams, to run into an unphysical solution. The grey lines in the left panel correspond also to unphysical Green's functions, which however never cross the physical one.

As for the physical implications of the essentially formal problem discussed in this section, let us note here: The authors of [9] have managed to relate the irreducible vertex divergences of the *Hubbard model* to the behaviour of the local physical charge susceptibility  $\chi_{ch}$ , defined in Eq. 2.13, which obviously decreases as the Mott transition is approached. By a projection into the eigenvalue basis it becomes clear that the decrease of  $\chi_{ch}$  is originated by several initially positive eigenvalues changing sign, and by that causing a vertex divergence each time. This behaviour is also shown in Fig. 2.12, where it is evident that without the negative eigenvalues,  $\chi_{ch}$  would saturate at a value too large in the Mott insulating phase.

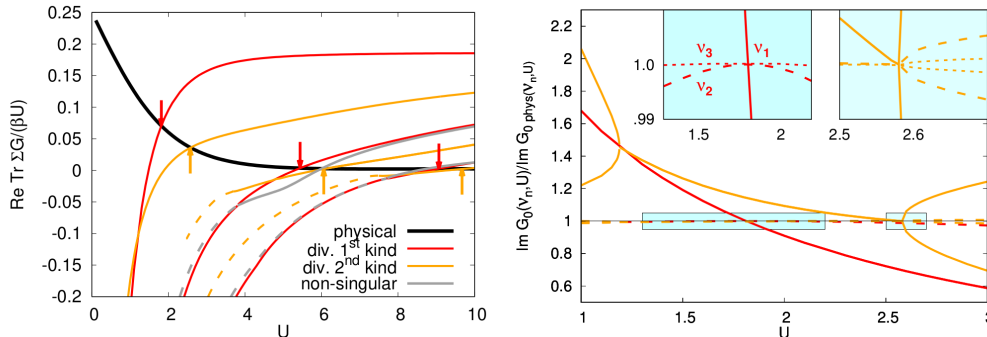


Figure 2.11: Left panel: Double occupancy expression, for the Hubbard atom, where  $\Sigma$  is calculated with the physical (black solid line) or with unphysical  $G_0$  (red and orange lines). It is obvious that this observable should decrease with increasing  $U$ , which, however, happens only for the physical solution. For specific parameters the unphysical and physical solutions cross exactly where also a divergence of the irreducible vertex takes place. Right panel: Imaginary part of the unphysical and physical Green's function  $G_0$  crossing each other for a specific  $U$ , where the dependence on  $U$  at the crossing determines the frequency structure of the vertex divergence. Taken from [9].

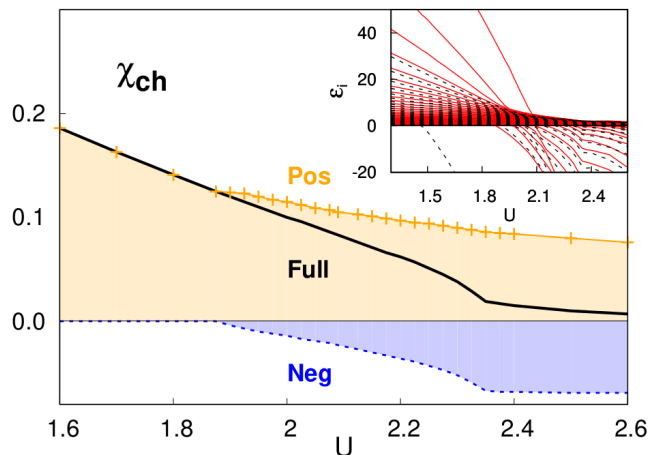


Figure 2.12: Results for  $\chi_{ch}$  of a DMFT calculation for the half-filled *Hubbard model*, where the internal frequency sum is projected into the corresponding eigenbasis. Evidently, at large  $U$  the negative eigenvalues cause the decrease of  $\chi_{ch}$ , leading to the expected strongly suppressed value in the Mott insulating phase. Taken from [9].

## 2.3 Anderson Impurity Model

The Anderson impurity model (AIM) [32] is one of the most prominent models in solid state physics. Originally introduced to describe the physics of local magnetic moments, eventually applied to study the Kondo effect [12], the AIM nowadays has become a crucial part of the DMFT scheme.

The AIM describes a single impurity site embedded in a non-interacting bath of electrons, which can hybridize onto/from the impurity site. In the case of interest for this work, the impurity site has a single non-degenerate level, resulting in a doubly occupied impurity site at most.

The Hamiltonian of the Anderson impurity model [33] is given in Eq. 2.27, and depicted in a simplified way in Fig. 2.13, for the specific case considered here.

$$\begin{aligned}
 \mathcal{H} &= \sum_{\sigma} \epsilon_d c_{d,\sigma}^{\dagger} c_{d,\sigma} + U n_{d,\uparrow} n_{d,\downarrow} \\
 &+ \sum_{\mathbf{k},\sigma} \epsilon_{\mathbf{k}} c_{\mathbf{k},\sigma}^{\dagger} c_{\mathbf{k},\sigma} \\
 &+ \sum_{\mathbf{k},\sigma} (V_{\mathbf{k}} c_{d,\sigma}^{\dagger} c_{\mathbf{k},\sigma} + V_{\mathbf{k}}^* c_{\mathbf{k},\sigma}^{\dagger} c_{d,\sigma})
 \end{aligned} \tag{2.27}$$



In the first line the impurity site terms are given, where  $\epsilon_d$  corresponds to the energy of the impurity level and  $U$  is the local interaction value, contributing if the site is doubly occupied.  $c_{d,\sigma}^\dagger/c_{d,\sigma}$  creates/annihilates an electron on the impurity site and  $n_{d,\sigma}$  is equal to  $c_{d,\sigma}^\dagger c_{d,\sigma}$ . The second line describes the energy of the non-interacting bath of electrons with  $\epsilon_{\mathbf{k}}$  being the dispersion relation, while in the third line the hybridization onto/from the impurity site ( $V_{\mathbf{k}}/V_{\mathbf{k}}^*$ ) is given.

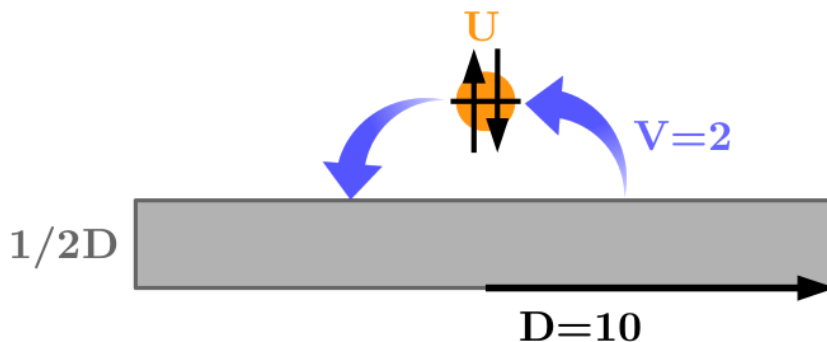


Figure 2.13: A simple sketch of the Anderson Impurity model, depicting the basic elements of the Hamiltonian in Eq. 2.27 - a box-shaped density of states (grey), hybridization onto/from the impurity site from/to the electron bath (blue) and the local interaction on the impurity site, if doubly occupied (orange).

Depending on the choice of parameters, situations with and without local magnetic moments can be realized, which is discussed in the subsequent section. For this work the parameters are chosen in the following way: The hybridization is taken to be  $\mathbf{k}$ -independent, i.e.  $V_{\mathbf{k}} = V$  and the non-interacting density of states (DOS)  $\rho(\epsilon)$  for the bath electrons is chosen to be box shaped. The corresponding  $\rho(\epsilon)$  is given in Eq. 2.28, where  $D$  is the half bandwidth

$$\rho(\epsilon) = \frac{1}{2D} \Theta(D - |\epsilon|) \quad (2.28)$$

The values for the parameters defining the specific model used in the calculations are listed in Tab. 2.1, and illustrated schematically in Fig. 2.13.

The choice of a box-shaped DOS and a  $\mathbf{k}$ -independent hybridization ensures that no particular features of  $\rho(\epsilon)$  or  $V$  will affect the study of divergences.

Parameters	Values
half bandwidth $D$	10
hybridization $V$	2
interaction $U$	3-10

Table 2.1: Parameters of the AIM for this work

### 2.3.1 Local Magnetic Moments

As the following section 2.4 is deeply connected to the physics of local magnetic moments, their appearance shall be briefly discussed. Note that for this section the ground state properties are analysed, hence the temperature is set to zero.

As a starting point the impurity site, detached from the host metal, is analysed, i.e.  $V = 0$ . In the case we consider here, depicted in Fig 2.14, there is only one orbital at the impurity site, which can be at most doubly occupied. The empty level has energy 0, the singly occupied, which is degenerate because of the spin, has the energy  $\epsilon_d$  and the doubly occupied impurity site has  $2\epsilon_d + U$ , due to the on-site interaction. It is clear that only the singly occupied impurity site has a non-zero magnetic moment. The energies, or more precisely the values of  $\epsilon_d$  and  $U$ , can be chosen in a way, for the singly occupied state to be the ground state, which corresponds to a localized magnetic moment.



Figure 2.14: Isolated interacting impurity with a single orbital. Due to the spin-degeneracy the impurity site can be at most doubly occupied.

The next step is to analyse a non-interacting ( $U=0$ ) impurity embedded in a metallic host ( $V \neq 0$ ). Due to the hybridization a change in the density of states is observed. This can be seen by calculating the Green's functions of the conduction band and the impurity site, which is discussed in detail in [33].

More specifically, assuming a flat conduction band and a  $\mathbf{k}$ -independent hybridization  $V$ , as is the case in this work, the change in the local density

of states of the impurity site  $[\delta\rho(\epsilon)]$  can be obtained easily. This is given by

$$\delta\rho(\epsilon) = \frac{\Delta/\pi}{\epsilon^2 + \Delta^2}, \quad (2.29)$$

where  $\Delta = \pi\rho_0|V^2|$ . Note that this broadening of the DOS leads to a renormalization of the specific heat and the magnetic susceptibility, but it will not give a Curie-Weiss contribution to the magnetic susceptibility.

The final step is to include the on-site interaction at the impurity site ( $U \neq 0$ ). For specific parameters, discussed below, the interacting Anderson impurity model can be mapped onto a  $s$ - $d$  model.<sup>6</sup> This model consists of a Heisenberg exchange interaction between the local moment of the impurity site and the conduction electrons of the host metal [33]. The Hamiltonian is given in the following, where  $J_{\mathbf{k},\mathbf{k}'}$  is a coupling constant.

$$\mathcal{H}_{s-d} = \sum_{\mathbf{k},\mathbf{k}'} J_{\mathbf{k},\mathbf{k}'} (S^+ c_{\mathbf{k},\downarrow}^\dagger c_{\mathbf{k}',\uparrow} + S^- c_{\mathbf{k},\uparrow}^\dagger c_{\mathbf{k}',\downarrow} + S_z (c_{\mathbf{k},\uparrow}^\dagger c_{\mathbf{k}',\uparrow} - c_{\mathbf{k},\downarrow}^\dagger c_{\mathbf{k}',\downarrow})) \quad (2.30)$$

One can demonstrate that in the parameter regime  $\epsilon_d + U \gg \epsilon_F$ ,  $\epsilon_d \ll \epsilon_F$  and  $|\epsilon_d + U - \epsilon_F|$ ,  $|\epsilon_d - \epsilon_F| \gg \Delta$  the mapping of the interacting Anderson impurity model onto the  $s$ - $d$  model works, which means that a local magnetic moment exists, and results in an antiferromagnetic exchange interaction, for details see [33].

In our case, using the values given in Tab. 2.1, the abovementioned constraints hold (note that we also impose particle-hole symmetry), as we have:

$$\Delta = \pi\rho_0 V^2 = \pi/5 < 1 \quad \text{and} \quad \epsilon_d = -U/2 \quad (2.31)$$

## 2.4 Kondo Scale

The full treatment of the Kondo effect and the Kondo problem exceeds the scope of this thesis, which is why it is summarized here only shortly, focusing on the specific elements needed in the course of this work. For a thorough treatment of the Kondo effect and of the Kondo problem, the reader is referred to the literature, e.g. [33, 34, 35, 36].

In a nutshell, the Kondo effect is a many-body effect which was first observed in metals with magnetic impurities, in particular in simple metals containing a small amount of transition metals, i.e. at "d" impurities [36].

---

<sup>6</sup>This mapping is somewhat similar to the one applicable to the half-filled Hubbard model at strong coupling ( $U \ll t$ ), where by projecting out the double-occupied/empty state one obtains an Heisenberg model with coupling constant  $J = \frac{4t^2}{U}$  [33, 35].

In such systems, a term proportional to  $-\ln(T)$  in the electrical resistivity of the conduction electrons is observed in the low-temperature regime. Fig. 2.15 depicts schematically such a contribution, which in combination with the resistivity term stemming from the lattice vibrations (typically  $\propto T^5$ ), gives a resistivity minimum. Note that this is merely a sketch, i.e.  $\rho$  and  $T$  are plotted in arbitrary units, nevertheless it matches qualitatively well the behaviour found in realistic cases, e.g. in copper doped with iron [36].

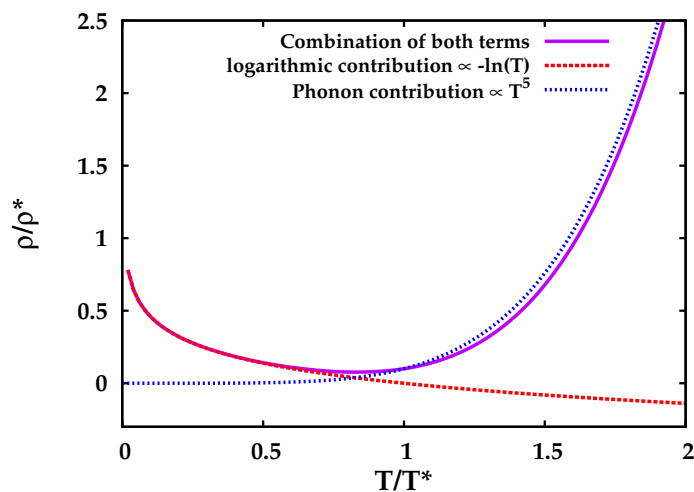


Figure 2.15: Resistivity minimum due to the combination of a logarithmic term increasing with decreasing temperature and the typical phonon term - this is merely an example  $\rho$  and  $T$  are given in arbitrary units ( $\rho^*, T^*$ ).

The  $-\ln(T)$  term appears due to the interaction of the conduction electrons with the localized magnetic moments of the impurities. This was first explained by J. Kondo in 1964 [12], who showed that second order perturbation theory is sufficient to get logarithmic terms in the resistivity. In fact, these logarithmic terms stem from spin flip processes, which can be seen if the problem is analysed using the  $s$ - $d$  model, given in Eq. 2.30. In particular, one of the second order spin flip terms is depicted in Fig. 2.16, where the dotted line represents the local magnetic moment of the impurity and the solid line represents a conduction electron. In the scattering process one of the conduction electrons with wavevector  $\mathbf{k}$  and spin down ( $\downarrow$ ) is scattered to the state  $\mathbf{k}' \downarrow$  via an intermediate state where the spin of the conduction electron and the impurity spin are flipped. These processes give rise to a temperature dependent scattering amplitude, because terms containing factors like  $(1 - f_{\mathbf{k}''})$ , describing the probability of an empty intermediate state,

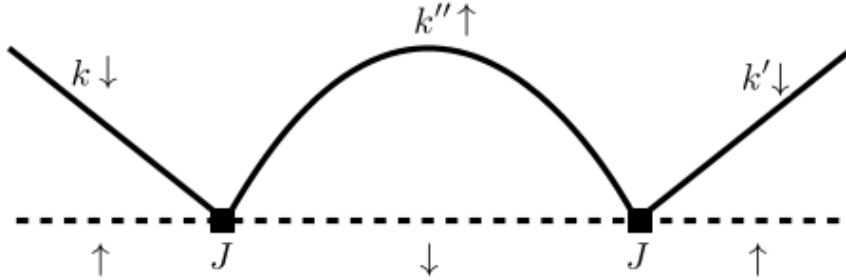


Figure 2.16: Spin flip processes, second order in the coupling strength  $J$  (assumed to be  $\mathbf{k}$  independent), which are responsible for the temperature dependent scattering amplitudes, eventually causing the logarithmic terms in the electrical resistivity. A conduction electron with wavevector  $\mathbf{k}$  and spin down ( $\downarrow$ ) is scattered into an intermediate state  $\mathbf{k}'' \uparrow$ , where the spins of both, the conduction electron and the impurity are flipped. The conduction electron is then scattered to the final state  $\mathbf{k}' \downarrow$ .

do not cancel out [33, 35, 36].

After calculating all the scattering amplitudes, and considering a random distribution of impurities in the metal, the resistivity of the conduction electrons amounts to

$$R(T) = aT^5 + R_0 - c_{imp}R_1 \ln \left( \frac{k_B T}{D} \right), \quad (2.32)$$

where  $c_{imp}$  represents the concentration of impurity sites in the metallic host [33] and  $R_1$  is a factor, containing amongst other constants, the coupling strength  $J$  (assumed to be  $\mathbf{k}$  independent). We should also note that the first term in Eq. 2.32 is the resistivity due to the electron-phonon interaction and the second term is the temperature-independent resistivity contribution accounting for the scattering of conduction electrons on non-magnetic impurities. We recall that, as for the latter a spin flip process is evidently not possible, their low-temperature contribution reduces to a more standard, constant ( $R_0$ ) behaviour [23, 24]. As a result, calculating the minimum of the resistivity  $R(T)$  yields a temperature which weakly depends on the impurity concentration ( $T_{min} \propto c_{imp}^{1/5}$ ).

Hence, with these findings, the observed resistivity minimum could be explained as well as the subsequent increase with decreasing temperature. Yet, it is obvious that the solution in Eq. 2.32 is not universally applicable, as for  $T \rightarrow 0$  the logarithmic term diverges, which contradicts the always finite experimental extrapolated value of the resistivity for  $T \rightarrow 0$  in these

metallic systems. Moreover, analogous "artificial" divergences are also found in other physical quantities like the magnetic susceptibility or the specific heat.

From a theoretical point of view, this can be traced back to a breakdown of the perturbative ansatz. In fact, the challenge of finding a suitable treatment of the Kondo effect for  $T \rightarrow 0$ , has been known for decades of the last century as the "Kondo problem".

A first idea of summing up the leading logarithmic terms from higher orders of perturbation theory, carried out by A. A. Abrikosov in 1965 [37], did not solve the problem, but brought new insights. As it turns out, in this framework the divergence takes place at a *finite* temperature for all physical quantities (resistivity, specific heat and magnetic susceptibility). This temperature is known as the *Kondo temperature*, which is given by

$$k_B T_K \propto D e^{-1/2 J \rho_0}, \quad (2.33)$$

for the perturbatively treated *s-d* model ( $\rho_0$  is the constant value of a box-shaped density of states, which was assumed in this case) [33].

Later, Anderson found another way to sum up the leading logarithmic terms, which is known as the *Poor Man's scaling*. This method is a scaling approach which gradually eliminates scattering processes involving high energy states in the upper and lower band edge, resulting in a reduced bandwidth. The reduction is accounted for by a corresponding renormalization of the coupling strength.

Anderson's approach works perfectly for the ferromagnetic case. Yet, for the antiferromagnetic case of our interest, the reduction of the bandwidth only works down to an energy of the order of  $k_B T_K$ . At this point, the coupling strength diverges and the approach breaks down.

More advanced approaches, e.g. a non-perturbative renormalization group method used by Wilson [38], or the Bethe-Ansatz method which gave exact results [39, 40], were required to gain an accurate description of the non-perturbative regime for  $T < T_K$ . Their application eventually yielded a unified physical picture <sup>7</sup> [33, 35, 36] : For temperatures lower than  $T_K$  the impurity spin is gradually screened by conduction electrons. This results in a reduction of the magnetic moment and eventually the moment is fully quenched, as the conduction and impurity electrons form a singlet state, yielding a temperature independent contribution to the resistivity and a constant contribution to the magnetic susceptibility.

---

<sup>7</sup>For a concise review see [http://www.scholarpedia.org/article/Kondo\\_effect](http://www.scholarpedia.org/article/Kondo_effect), by A. C. Hewson and J. Kondo

Another important aspect is that for low temperatures all physical quantities can be expressed as universal functions of the energy scale  $T_K$ , which clearly shows the intrinsic importance of the *Kondo temperature*.

Note that the discussions of the Kondo effect and the Anderson impurity model have been made hitherto in a somewhat historical context, focusing on the implication of this effect on conduction electrons in metals with magnetic impurities. In other words, the resistivity of the conduction electrons was the quantity of interest.

The "building block" of this intriguing physics, i.e. the spin-dependent scattering processes occurring at a single impurity site, can of course have a variety of other applications. We recall, e.g., the resonances induced by the Kondo effect in quantum dots, which eventually enhance its conductivity, just the opposite trend compared to the effect in metals with impurities. In DMFT, the Kondo effect also plays a role: Here however, the impurity electrons are of relevance, as they mimic the local physics of the lattice system under consideration. Hence in DMFT, the Kondo effect, leading to a low-temperature Kondo resonance at the Fermi level, *enhances* the conductivity for a fixed interaction strength  $U$ .

In the perspective of this Master work, it is intriguing to investigate the relation of the Kondo scale with the irreducible vertex divergences occurring in strongly correlated systems. To this end, an analytic expression for the Kondo scale valid for the single impurity Anderson model and the chosen parameters is highly desirable, as Eq. 2.33 is only valid for the *s-d* model solved using the perturbative ansatz described above.

Unfortunately, the *Poor Man's scaling* approach does not work in all parameter regimes. This is due to the fact, that the Anderson impurity model also contains charge fluctuations of the impurity site, in contrast to the *s-d* model. In some cases, these charge fluctuations are only virtual or can be treated perturbatively by a scaling approach. For example, if the impurity levels, i.e.  $\epsilon_d$  and  $\epsilon_d + U$  lie outside the conduction band ( $\epsilon_d \ll -D$  and  $\epsilon_d + U \gg D$ ) there are no real charge fluctuations, and a Schrieffer-Wolff transformation can be safely used to map the Anderson model onto an *s-d* model [33]. In this case, the Kondo scale would be given by a similar expression as Eq. 2.33 with  $J = \frac{U|V^2|}{|\epsilon_d||\epsilon_d+U|}$ . Charge fluctuations can be taken into account perturbatively in a scaling approach, if only one impurity level or both lie inside the conduction band. However, for  $|\epsilon_d|$  and  $|\epsilon_d + U| \ll D$  there is almost no renormalization of the parameters  $U$  and  $\epsilon_d$ , i.e. the scaling approach is not applicable. In the most general situation, depending on the values of  $\Delta$ ,  $U$  and  $\epsilon_d$ , charge fluctuations might occur or not and the Kondo scale will be a complicated function of these parameters.

A more general treatment can be made using the Bethe ansatz [33]. For the single impurity Anderson model, this yields an expression for the Kondo temperature in the case of  $D \gg U$  (assuming a linear dispersion), which reads

$$k_B T_K = 0.4107 U \left( \frac{\Delta}{2U} \right)^{1/2} e^{-\pi U/8\Delta + \pi\Delta/2U} \quad (2.34)$$

This is Eq. (6.109) of [33], together with the numerical factor 0.4107, derived by a comparison with numerical renormalization group results obtained by Krishna-murthy et al. [41]. Eq. 2.34 will be used for comparing the numerical results of this Master work with the Kondo temperature.

At this point, it is time to illustrate our original expectation for the relation of the Kondo scale with the irreducible vertex divergences.

As discussed in Sec. 2.2 in the atomic limit regime, a linear shape of the vertex divergence lines is found. In the low-temperature intermediate coupling regime, however, we expect that the Kondo scale will play a crucial role for the behaviour of the divergence lines, especially governing the  $T \rightarrow 0$  part of the line. Due to the fact that, in the AIM no metal-insulator transition exists for  $T = 0$ , we are certain that no divergence at a finite interaction value will be found for  $T \rightarrow 0$ .

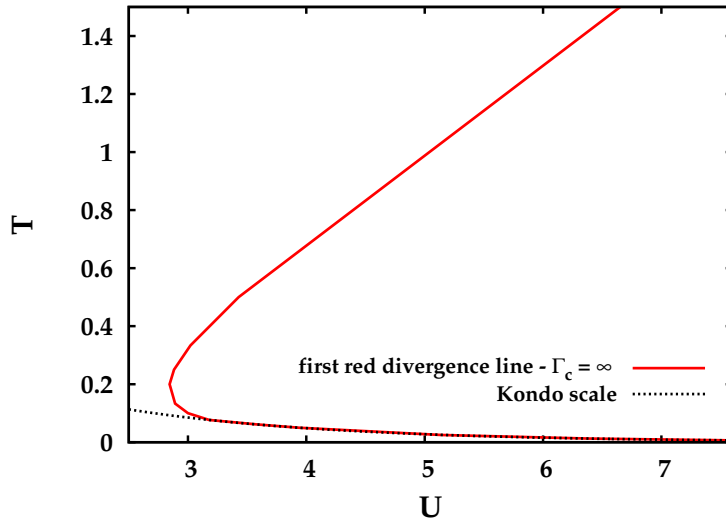


Figure 2.17: Expectation of the shape of the first divergence line of the AIM, showing a linear behaviour in the atomic limit regime. For low temperatures we expect the Kondo scale to govern the way how the divergence line approaches  $T \rightarrow 0$ , and due to the absence of a MIT at  $T = 0$ , no divergence at finite  $U$  is found.

The expectations were not met, which will be discussed in Chapter 4.



# Chapter 3

## Methods

*After thoroughly discussing the theoretical framework and the latest results reported in the recent literature, we want to highlight some crucial aspects of the methods we use to calculate the irreducible vertex divergences in the Anderson impurity model, defined in the previous section. To this end, we shortly mention the Continuous Time Quantum Monte Carlo (CT-QMC) and Exact-Diagonalization (ED) methods, as well as the post processing procedures used to determine the interaction value  $\tilde{U}$ , at which the divergences occur. As parts of these methodologies were already discussed in a previous project [50], we will focus here especially on the improvements achieved over the course of this Master work, which enabled a more precise calculation of the location of the vertex divergences.*

### 3.1 CT-HYB

The first step in obtaining vertex divergences is the calculation of the two-particle Green's function. We used the *w2dynamics* [42] package, which is a CT-QMC solver in the hybridization expansion, hence CT-HYB. The basics of Continuous Time Quantum Monte Carlo calculations were already discussed in a preceding work [50]. Here, we just refer the reader to the most pertinent literature: In particular, references [43, 44] and [47] can be recommended as a thorough introduction to this topic.

If not explicitly stated otherwise, for all calculations *w2dynamics* was used with a slight modification of its standard implementation to allow the read-in of a fixed electronic bath (see [50] for details).

During the calculations with *w2dynamics*, however, a very specific problem was observed, which will be discussed in the next section.

### 3.1.1 The random number generator

For very specific parameter sets (i.e., particular values of  $U$  and  $T$ ) our calculations yielded  $Im\Sigma(i\nu)$  with significant systematic errors in its high-frequency asymptotics. This was also leading to an incorrect behaviour of the irreducible vertex function and the singular eigenvectors. As an example for such a situation, the results for  $Im\Sigma(i\nu)$  of a pathological calculation is shown for positive Matsubara frequencies only in Fig. 3.1. It is evident that the asymptotic behaviour does not show the correct decrease of  $Im\Sigma(i\nu)$  towards zero at high frequencies, but a seemingly linear trend towards  $-\infty$ . The two-particle quantities show a similar unphysical "drift".

After a tedious search for the origin of this peculiar behaviour, we could identify the random number generator as the source of this error. In fact, the old random number generator, previously implemented in *w2dynamics*, had produced random numbers not to a sufficient accuracy, leading to operators in the trace with exactly same imaginary time. While unnoticed in many cases, in delicate calculations, such as those presented in this thesis, for very specific sets of parameters, this problem could indeed affect the quality of the final results.

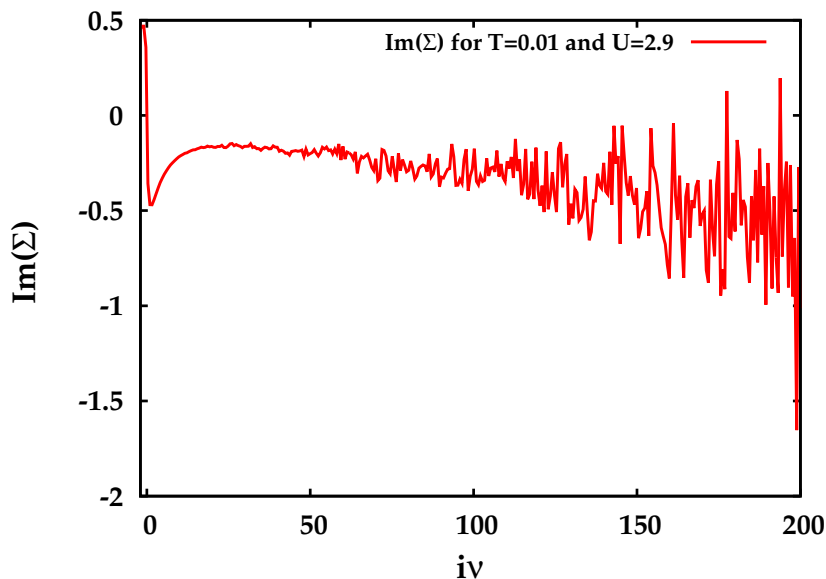


Figure 3.1: Imaginary part of the self-energy for positive Matsubara frequencies of a pathological calculation. As it turned out, the random number generator was the origin of the problem causing this false asymptotics of one- and two-particle quantities (two-particle quantities not shown).

After this bug has been identified, the random number generator was

substituted and we performed rigorous tests at many temperatures and interaction values. The tests showed that for any parameter set considered, including those which have been previously problematic, the pathological results, discussed above, no longer appear. Moreover, it should be stressed that for all non-pathological calculations performed with the old random number generator, no deviation with respect to the results was observed, indicating that these subtle problem was affecting a very limited subset of cases.

## 3.2 Exact Diagonalization

Another impurity solver allowing for the calculation of the two-particle Green's function exploits the Exact-Diagonalization method (ED) [48, 49]. Essentially, in this scheme, the hybridization function of the AIM is approximated by a discretized bath, i.e. a finite number of  $n_B$  bath sites. Under this assumption, and by that, the Hamiltonian can be diagonalized exactly using standard lapack routines. The calculations of the one- and two-particle Green's functions (and thus  $\Sigma$  and  $\Gamma$ ) can be performed then by means of the Lehmann representation [49, 19, 18]. However, the calculation of two-particle quantities is only possible to a very limited extent, due to the costly scaling of the algorithm with  $n_B$ . For our two-particle calculations, we used 5 sites, i.e. one impurity and four bath sides.

## 3.3 Postprocessing: Analysis of Vertex Divergences

In the preceding Projektarbeit [50], the method to identify the interaction value  $\tilde{U}$ , where the eigenvalue of the generalized susceptibility is equal to zero was of central interest and, thus, described in greatest detail. For this reason, we will focus, in particular, on the new progress achieved at this regard, in the course of the Master work. Let us start by recalling that from calculations at the same temperature for different interaction values the eigenvalue of interest of  $\chi_c$ <sup>1</sup> must be extrapolated to yield an estimate for  $\tilde{U}$ . In a bisection procedure calculations with interactions values closer to  $\tilde{U}$  are then performed until a satisfactory refinement in  $U$  is reached, which for our work was for the first lines  $\mathcal{O}(10^{-1})$  and for all the subsequent lines

---

<sup>1</sup>Note that, as explained in [50], we actually analyse the eigenvalues of  $\chi_c/\chi_0$  as here the eigenvalues inducing the vertex divergences can be distinguished easily from the ones decaying like  $1/\nu^2$ .

$\mathcal{O}(10^{-2})$  in  $U$ . After that,  $\tilde{U}$  is estimated from a linear approximation of the two results for eigenvalue of interest, which are closest to zero.

As in this thesis the calculation of other divergence lines but the first is of interest, let us recall here: The second, third, fourth and fifth divergence lines calculated correspond to the  $\tilde{U}$  values where the second, third, fourth and fifth eigenvalue of the generalized susceptibility in the charge channel is equal to zero. In the cases of the orange divergence lines a simultaneous vanishing of the first and second eigenvalue of the susceptibility in the particle-particle up-down channel is observed, for the first and second orange line, respectively. Because the eigenvalues of  $\chi_c$  and  $\chi_{pp,\uparrow\downarrow}$  are exactly the same in the case of an orange vertex divergence, the eigenvalues of  $\chi_{pp,\uparrow\downarrow}$  will not be explicitly shown in the following. With the help of the corresponding singular eigenvectors the eigenvalues could be related unambiguously to the associated divergence line, also in more complicated situations, such as the crossing of divergence lines. In chapter 4 general features of the singular eigenvectors (such as symmetry, minima, maxima), corresponding to the vanishing eigenvalues, which are necessary to perform this identification, will be discussed.

As for the afore mentioned improvement in the procedure to compute  $\tilde{U}$ , this exploits the information obtained as a byproduct from calculations of  $\tilde{U}$  values of previous divergence lines. Using this information allows for a faster bisection procedure, i.e. the  $U$  grid can be initially estimated to a higher precision, without performing a calculation for the specific eigenvalue of interest, as will be discussed in the following subsection.

### 3.3.1 Extrapolation procedure to determine $\tilde{U}$

In Fig. 3.2 the eigenvalue ( $\lambda$ ) of the generalized susceptibility corresponding to the third red line is plotted for  $T = 0.5$ . Every dot represents a result for  $\lambda$  obtained from a *w2dynamics* calculation. The dots at interaction values further away from  $\tilde{U}$  have been obtained beforehand as a byproduct from calculations at the same temperature, but for previous divergence lines, where other eigenvalues were of interest (data from the second, third, fourth and fifth divergence line are reported in Fig. 3.2). As it can be seen,  $\lambda(U)$  displays a rather evident quadratic behaviour in  $U$ . This information could be used to improve the extrapolation of the results for  $\lambda$  to estimate the interaction interval where  $\tilde{U}$  would most likely be found, enabling us to perform considerably less calculations.

The procedure described above for the case of the eigenvalue corresponding to the third red line for  $T = 0.5$  can be used for all  $\tilde{U}$  values of interest. Throughout this thesis this was done for all cases with a quadratic fit of the pre-existing data, which yielded very satisfying results. As a verification, of

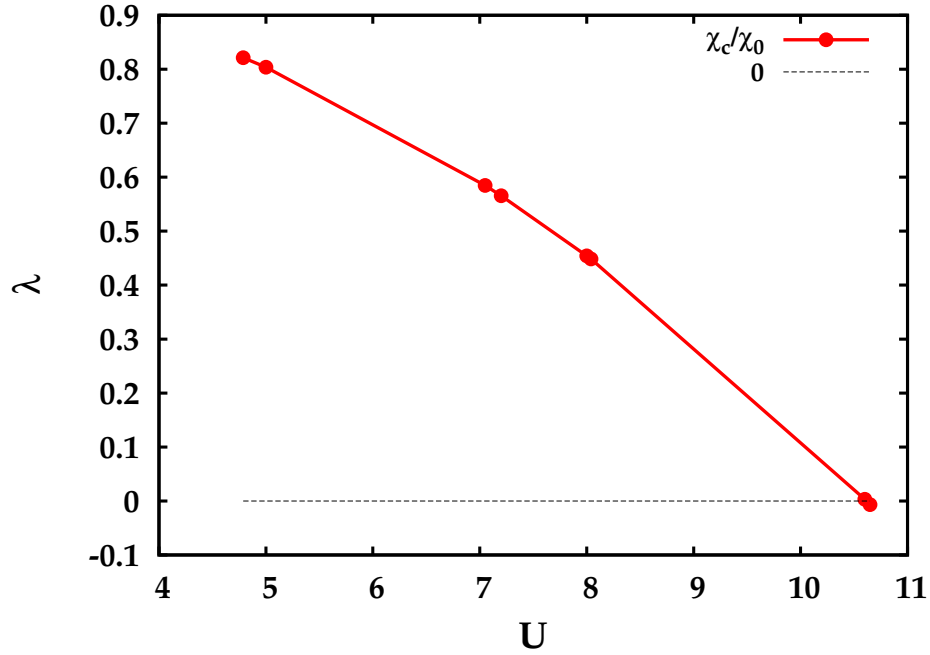


Figure 3.2: Fifth smallest eigenvalue of  $\chi_c$  for  $T = 0.5$ . Every dot represents a calculation, whereas the calculations at interaction values further away from  $\tilde{U}$  were performed to obtain the  $\tilde{U}$  values of previous divergence lines (here second, third and fourth). The  $U$  dependence of the eigenvalue allows for a good approximation as a quadratic function.

the quadratic fit, being the best choice for fitting the results of the eigenvalue of interest, we performed a comparison with higher order fits in Fig. 3.3 and Fig. 3.4. In the plots the extrapolations from a quadratic, a cubic and a fourth order fit as well as the results for two different temperatures are shown. It can be seen that the quadratic fit provided the best estimates for both temperatures.

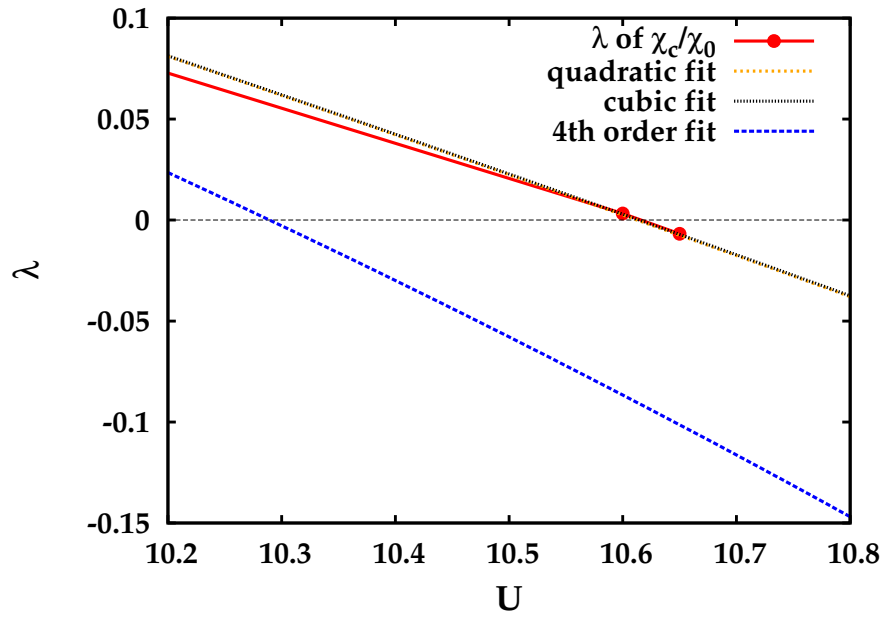


Figure 3.3: Comparison of the predictive qualities of a quadratic, a cubic and a fourth order fit (dashed lines) for  $T = 0.5$  for the singular eigenvalue of the third red line. In this case, evidently, the quadratic and the cubic fit could estimate the results (red solid line) best.

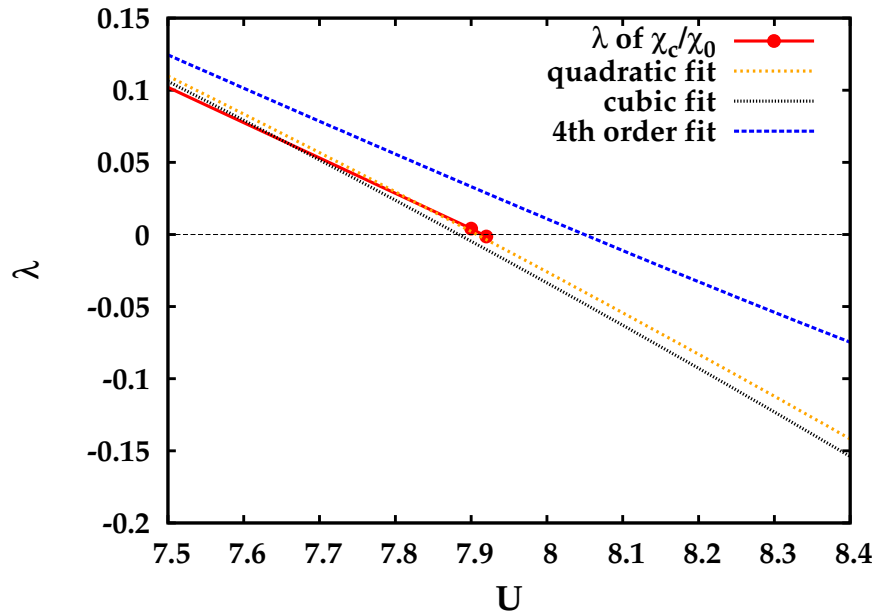


Figure 3.4: As Fig.3.3 for  $T = 0.3333$ . Here the quadratic fit yields the most satisfying estimate for  $\tilde{U}$ .

# Chapter 4

## Results and Discussion

*After defining all quantities of importance in the analysis of irreducible vertex divergences in Chapter 2 and introducing the methods used to extract them from two-particle CT-QMC calculations in Chapter 3, we now want to present the results obtained throughout this thesis for the case of the Anderson impurity model (AIM). First, the divergence lines appearing in the phase diagram of the AIM are analysed and compared to the ones of the Hubbard model, allowing to clarify the roles played by the metal-insulator transition and the Kondo scale. Thereafter, several features of the singular eigenvectors  $V_c$  corresponding to the vertex divergences of the AIM are studied in great detail in terms of their temperature behaviour, as well as of their underlying symmetries. Through this analysis a better understanding of the different properties of the divergence lines and of their low-temperature features could be gained.*

### 4.1 Phase Diagram

In Fig. 4.1 the phase diagram of the AIM is shown, depicting all divergence lines obtained in the course of this thesis. The lines correspond to the interaction value  $\tilde{U}$  at a given temperature  $T$ , where the eigenvalue of the generalized susceptibility (charge or particle-particle up-down channel) vanishes. Red lines correspond to irreducible vertex divergences taking place in the charge channel (see Sec. 2.1 for the definition of the channels). Orange lines on the other hand represent divergences taking place in the charge and the particle-particle up-down channel simultaneously.

The behaviour of the first red divergence line is already described in great detail in a previous *Projektarbeit* [50]. Summarizing the corresponding results, there it has been argued, that the occurrence of an irreducible vertex

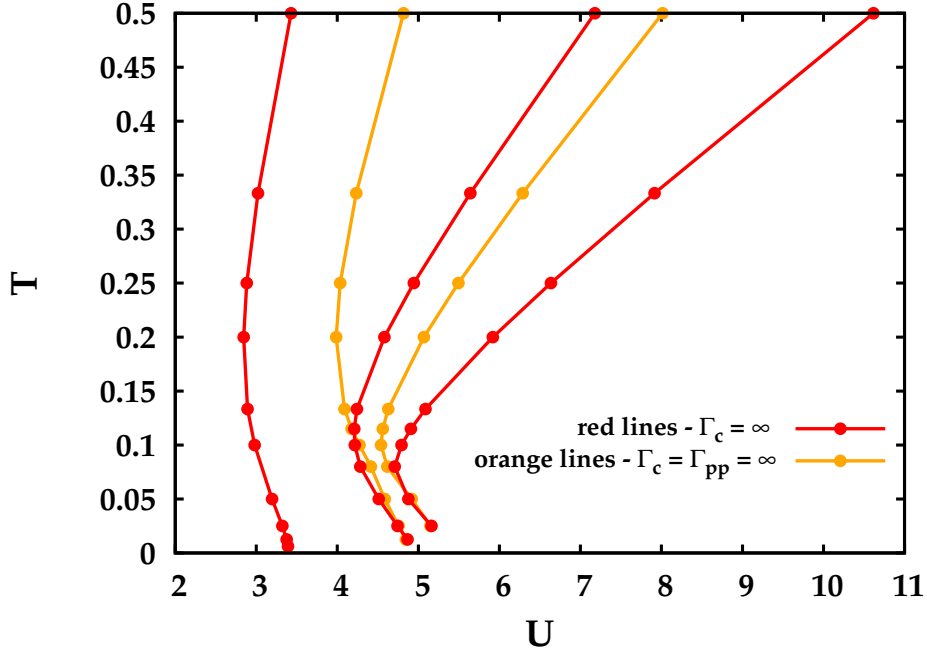


Figure 4.1: Phase diagram of the AIM depicting the first five divergence lines, i.e. the values  $\tilde{U}$  where for the temperature  $T$  the corresponding eigenvalue of the generalized susceptibility vanishes. Red lines correspond to divergences taking place in the charge channel, whereas along orange lines a simultaneous divergence in the charge and the particle-particle up-down channel is observed.

divergence at  $T = 0$  for a *finite* interaction value is very likely. Taking this into account, when analysing the behaviour of the other divergence lines shown in Fig. 4.1, it becomes rather evident that the divergence lines of the AIM show a *very similar* behaviour compared to the Hubbard model case, depicted in Fig. 2.8 [1, 2]. In the high-temperature/large interaction area of the phase diagram the lines show a linear behaviour, which would be expected, according to the insights of the results for the *Hubbard atom*, discussed in Sec. 2.2. Fig. 4.2 supports this expectation: Here the results for the first divergence line for the highest temperature values are compared with the first red divergence line of the *Hubbard atom* which is known analytically [2]. It can be seen that, although the line for the AIM shows almost a linear behaviour, the atomic limit is not yet reached completely. This is due to the fact that, in the parameter regime considered the half-bandwidth  $D$  is still the largest energy scale ( $D = 10$ ).

At intermediate temperatures, the divergence lines show a non-linear behaviour, as observed for the *Hubbard model*, as well as in the *Binary mixture*



and *Falicov Kimball* case. As argued in Sec. 2.2, however, qualitative differences between the disordered models and the *Hubbard model* emerge on the level of the corresponding singular eigenvectors, limiting the validity of the comparison with the latter ones. The same argument applies to the AIM, for which a "broadening" of the corresponding singular eigenvectors is observed, which is absent in the case of disordered models (the results for the eigenvectors of the AIM will be discussed in Sec. 4.2).

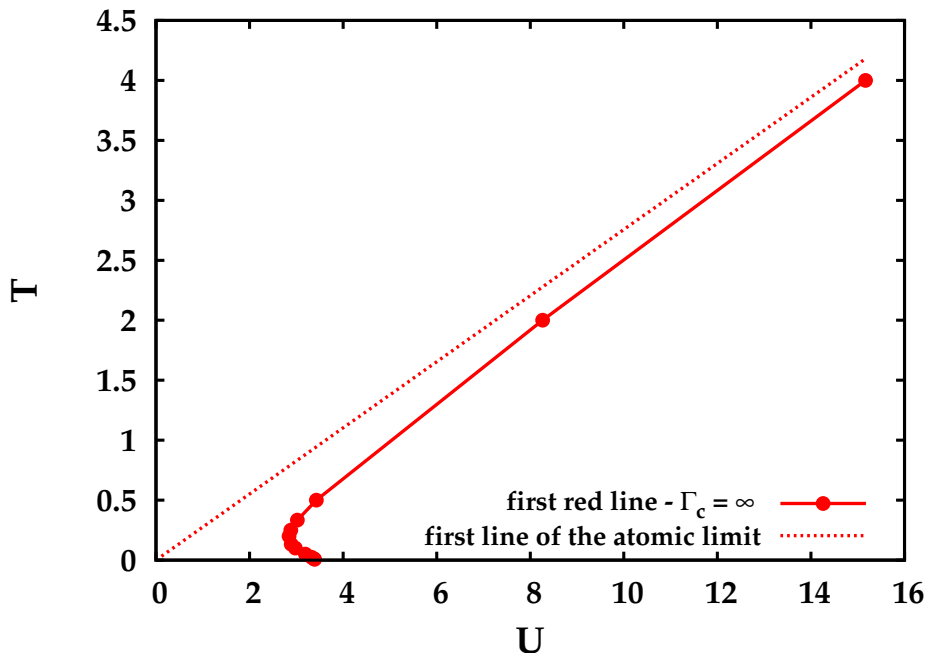


Figure 4.2: Comparison of the first divergence line of the AIM to the first divergence line of the *Hubbard atom* [2]. For high temperatures the behaviour is quite similar, however, the atomic limit is not entirely reached, due to the half-bandwidth  $D$  still being the largest energy scale.

Lowering the temperature further, one reaches the correlated metallic regime. Also there, the results of the AIM and the *Hubbard model* remain very similar, more than originally anticipated. The lines show a "re-entrance", i.e. a bending towards higher interaction values, as if the low-temperature intermediate interaction regime were "protected" against the non-perturbative mechanism originating the irreducible vertex divergences (as already discussed for the *Hubbard model* in Sec. 2.2). This unexpected resemblance, i.e. the re-entrance and especially the finite  $\tilde{U}$  at  $T = 0$ , raises concerns on the importance of the role played by the metal-insulator transition for the divergence lines, as suggested in recent publications. In fact, in

[2], where for disordered models, the *Hubbard atom* and the *Hubbard model* the occurrence of divergence lines is compared (as summarized in Sec. 2.2), it was inferred that the shape of the metal-insulator transition occurring in the *Hubbard model* should be responsible for the peculiar shape of the divergence lines in that model. Yet, comparing the results presented in this thesis for the AIM to the results for the DMFT solution of the *Hubbard model*, this conclusion seems to be not correct. In the AIM a metal-insulator transition at  $T = 0$  is absent, nevertheless the divergence lines show a qualitatively similar behaviour.

Our comparison rules out the metal-insulator transition as a crucial factor for the shape of the divergence lines in the correlated metallic regime. What may have, however, an important role is the Kondo scale, defined in Sec. 2.4. Our original expectation for the impact of the Kondo scale on the low-temperature behaviour of the first red divergence line has been illustrated in Fig. 2.17. As it can be seen in Fig. 4.3, where our numerical results are shown, the expectations were not met. In fact, the  $T \rightarrow 0$  behaviour of the first red divergence line is not at all governed by the Kondo scale.

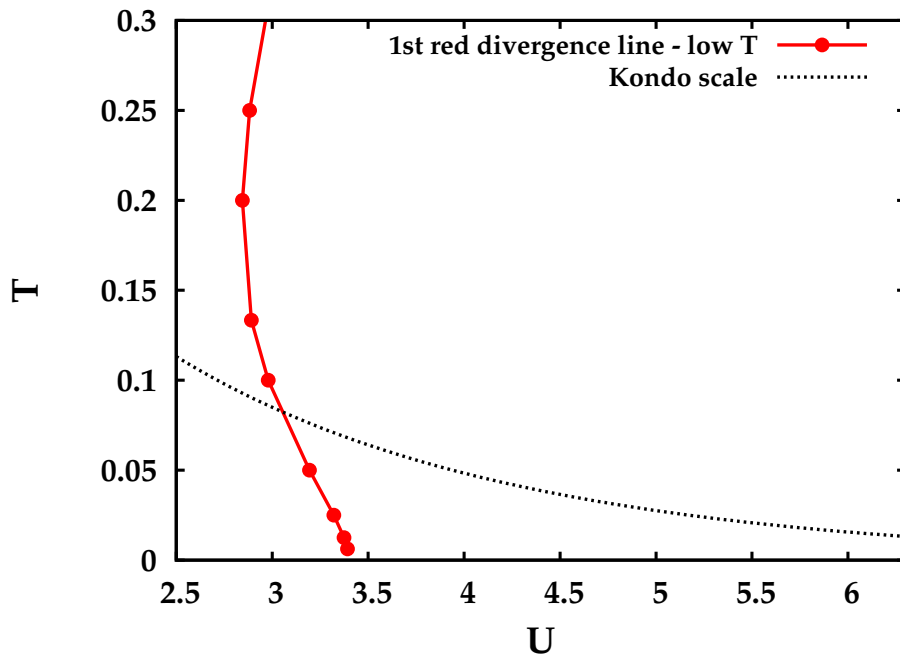


Figure 4.3: Low-temperature results for the first red divergence line compared to the Kondo scale defined in Eq. 2.34. Evidently the low-temperature behaviour is not related to the Kondo scale in the way we expected it to be.

However, as we shall see, to rule out the impact of the Kondo scale com-

pletely would be also not correct. To show this, we will include the Kondo scale in the whole phase diagram of the AIM to compare it to all divergence lines obtained throughout this thesis. In this respect, let us note here first that, the Kondo scale evidently does not refer to a sharp transition, but a crossover between two different regimes and that it can be estimated by several procedures. In Fig. 4.4 all divergence lines together with the Kondo scale obtained through estimates from several definitions are shown. The dashed black line corresponds to the analytic expression of the Kondo scale given in Eq. 2.34 ( $T_K$ ), the blue line corresponds to the same expression, without the factor computed by Krishna-murthy *et.al.* ( $T_L$ ) [33, 41]. Alternatively the Kondo scale can also be estimated from the quasiparticle renormalization factor  $Z$  as  $T_K \propto Z\Delta$  ( $\Delta$  as defined in Sec. 2.3), which is plotted as the dashed magenta line. In our case,  $Z$  was calculated independently by fitting the imaginary part of the self-energy obtained from one-particle *w2dynamics* runs at extremely low temperatures ( $T = 0.003333$ ). From this comparison, one can argue that while the  $T \rightarrow 0$  behaviour is not affected by  $T_K$ , the re-entrance of the red divergence lines most likely is. Especially the Kondo scale estimate  $T_L$  plotted as the blue dashed line, which lies almost exactly on top of the point where the divergence lines start to bend towards higher interaction values again (i.e. the re-entrance point), suggests such a connection. To prove this unambiguously the value of the Kondo scale for our specific model must be obtained from additional calculations for the corresponding local magnetic susceptibility. This will be further elaborated in Chapter 6. Let us also note, that while the connection of the re-entrance points of the red divergence lines and the Kondo scale seems very likely, for the orange lines the existence of such a relation is unclear. At this point, one can already say that the connection between the Kondo scale and the re-entrance represents an intriguing result, which could be interpreted in the following way: Starting from the high-temperature regime the divergence lines display a linear behaviour, as explained by the results of the *Hubbard atom*. Then a non-linear (but still monotonous) behaviour is observed, similar to the quadratic one of the *Binary Mixture* and *Falicov Kimball* case. When approaching the Kondo scale, however, the Kondo resonance builds up, leading to the bending towards higher interaction values of the divergence lines. In this scenario the Kondo scale would be the boundary between this two regions.

Further, if the re-entrance point, i.e. the point of the lowest interaction value obtained by a given divergence line, is connected to the Kondo scale, it is clear how an "extrapolation" of the phase diagram of the AIM at larger values of  $U$  would look like. At low temperatures the distance between the divergence lines would get narrower the lower the exponentially decreasing Kondo scale gets, as (*i*) they are always connected to results of the *Hubbard*

atom at higher temperatures and (ii) at the same time they should bend towards higher interaction values for  $T < T_K$ . This extrapolation can be exploited - in principle - to formulate possible predictions for the coexistence region of the metal-insulator transition of the *Hubbard model*, which will be mentioned in Chapter 6.

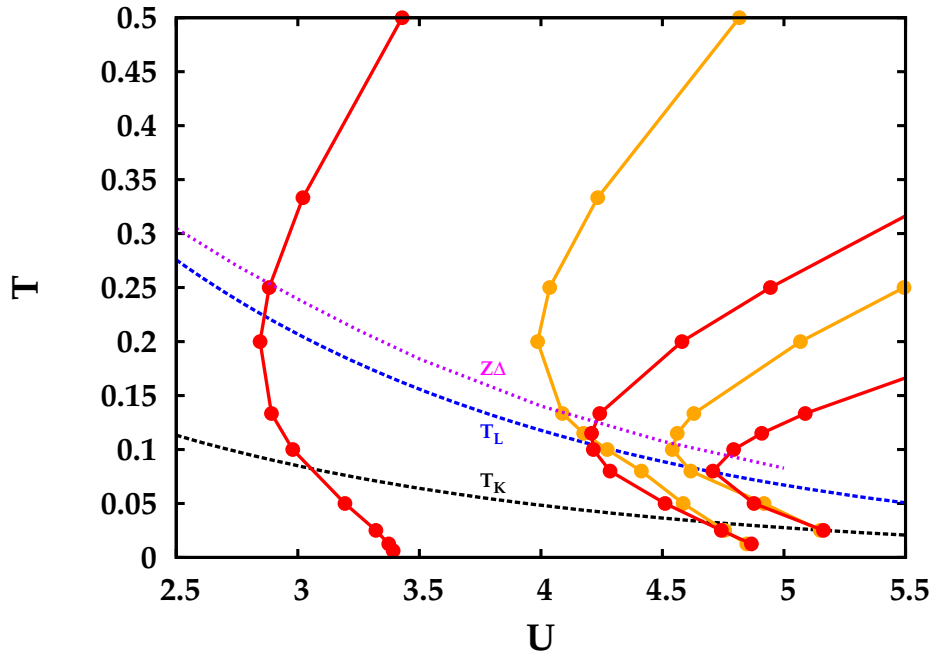


Figure 4.4: Phase diagram of the AIM with the Kondo scale, according to different definitions. The black dashed line corresponds to the analytical expression of  $T_K$  given by Eq. 2.34, the blue dashed line to the same expression, but without the factor obtained by Krishna-murthy *et.al.* [41] ( $T_L$ ) and the magenta dashed line represents the value of  $Z\Delta$  (see text). From this comparison one could infer a direct connection between the re-entrance points of the red divergence lines and the Kondo scale.

Returning to the comparison of the results of the *Hubbard model* and the AIM, apart from the general similarities discussed above a *qualitative* difference can be seen: At intermediate temperatures, the second and third divergence line cross, breaking the typical lines order found in all cases analysed so far (*Falicov Kimball*, *Hubbard atom* and *Hubbard model in DMFT*, i.e., always an orange line after a red one, before the next red line). We should also note, however, that the two lines cross again at low temperatures, restoring the typical line ordering. This surprising and hitherto unobserved feature will be discussed now in more details.

### 4.1.1 Crossing of Divergence Lines

In Fig. 4.5 a zoom of the phase diagram depicted in Fig. 4.1 in the area of the crossing of the second and third line is shown. Here, it can be also seen that even the fourth and fifth line show such a peculiar crossing, though, to a much smaller extent.

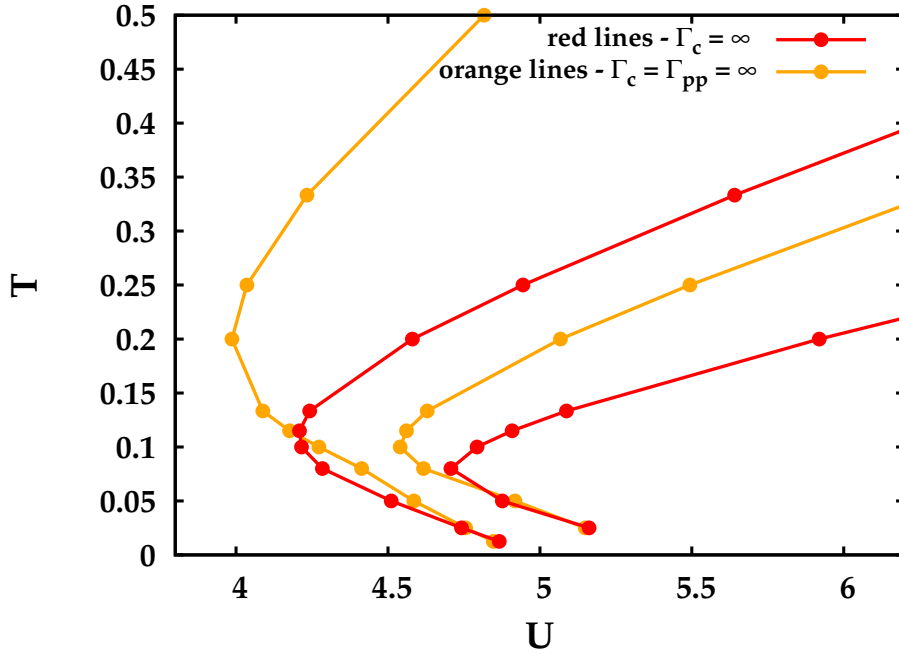


Figure 4.5: A zoom of the phase diagram of the AIM given in Fig. 4.1 where the crossing of the first orange and the second red line, as well as of the second orange and the third red line can be seen.

The first question one must ask, is, if this result is merely a numerical artefact. To rule out this possibility we performed several tests, which are described in the following.

#### Boxanalysis

For the calculation of two-particle quantities with *w2dynamics* a fermionic frequency box must be chosen, which can have, in principle, a huge effect on the results for the eigenvalues of the generalized susceptibility. To check whether a sufficient number of frequencies were taken into account, a so called "box analysis" was performed [44]. Here, the high-frequency part of the generalized susceptibility is discarded and the remaining central low-frequency part is diagonalized. This enables one to analyse the smallest eigenvalue as a

function of fermionic frequency box size. The result of this test is depicted in Fig. 4.6 and Fig. 4.7, where it can be seen, that the corresponding eigenvalues of the first orange and second red line are converged, indicating that enough frequencies were taken into account in the original calculations.

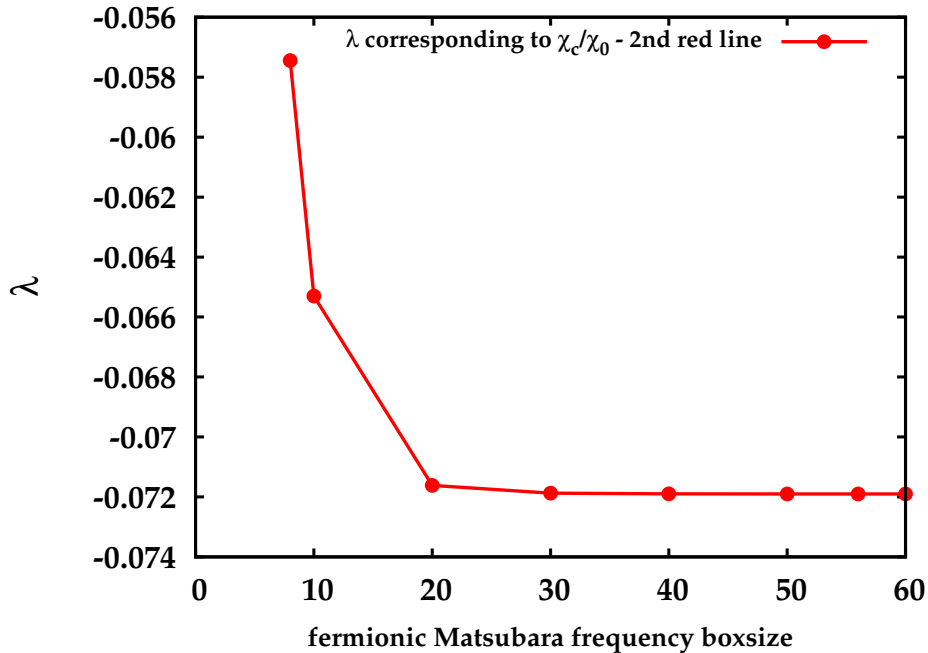


Figure 4.6: Box analysis of the eigenvalue corresponding to the second red line at  $T = 0.08$  and a specific interaction  $U$ . The test shows that the eigenvalue is converged i.e. 60 Matsubara frequencies (positive plus negative) are sufficient.

The next, more general, check is to verify the presence of the crossing, by trying to reproduce it using a completely different algorithm as impurity solver than *w2dynamics*, which is why we performed additional ED calculations for selected parameters.

### ED check

Using an ED implementation capable of performing calculations on the two-particle level, we ran a test for two interaction values at the temperature  $T = 0.08$ , i.e., where the largest distance between the red and orange line was observed. The results are displayed in the phase diagram given in Fig. 4.8, where it can be seen that the ED calculation *does reproduce* the crossing observed in the *w2dynamics* implementation of the CT-HYB QMC.

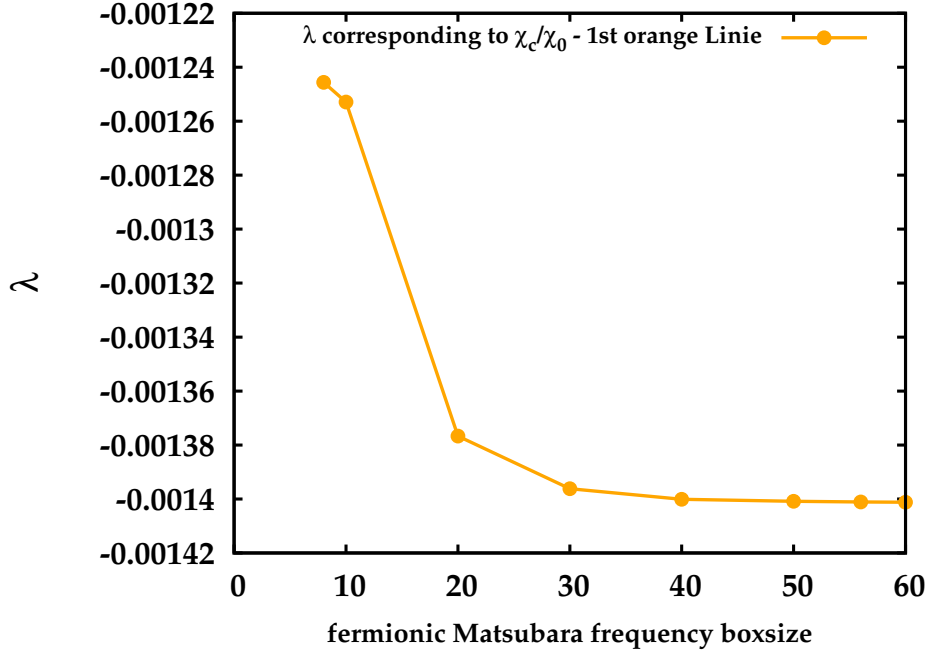


Figure 4.7: As Fig. 4.6 for the first orange line. Also for the calculations at  $T = 0.08$  for the first orange line 60 fermionic Matsubara frequencies were sufficient.

As for a more detailed comparison, in Fig. 4.9, a zoom onto the area where the calculation was performed is given. Here it can be noticed, that the results for  $\tilde{U}$  are not exactly on top of one another. In Fig. 4.10, the eigenvalues are plotted, where this slight discrepancy can be also observed. The reason for this difference of the results can be ascribed to the number of bath sites chosen for the ED calculation, which is also the computational bottleneck of the algorithm. In fact, in the two-particle ED calculation one is limited to four bath sites only, as for more sites the ED-evaluation of the Lehmann representation of the generalized susceptibility becomes computationally too expensive. In Fig. 4.11, where the imaginary part of the *w2dynamics* self-energy is compared to the one obtained from the ED fit of the hybridization function, it can be seen that four bath sites are not sufficient to completely capture the right behaviour of  $Im\Sigma$ . In Fig. 4.12, where six bath sites were used to fit the bath, it can be seen that the exact self-energy can be reproduced almost perfectly. This means that with six bath sites the discrepancies in the results of the two-particle calculation can be expected to vanish.

Summarizing, there are slight differences in the results, which could, however, be entirely ascribed to the ED discretization of the bath. In spite of this minor deviations, the crossing of lines could be clearly reproduced in

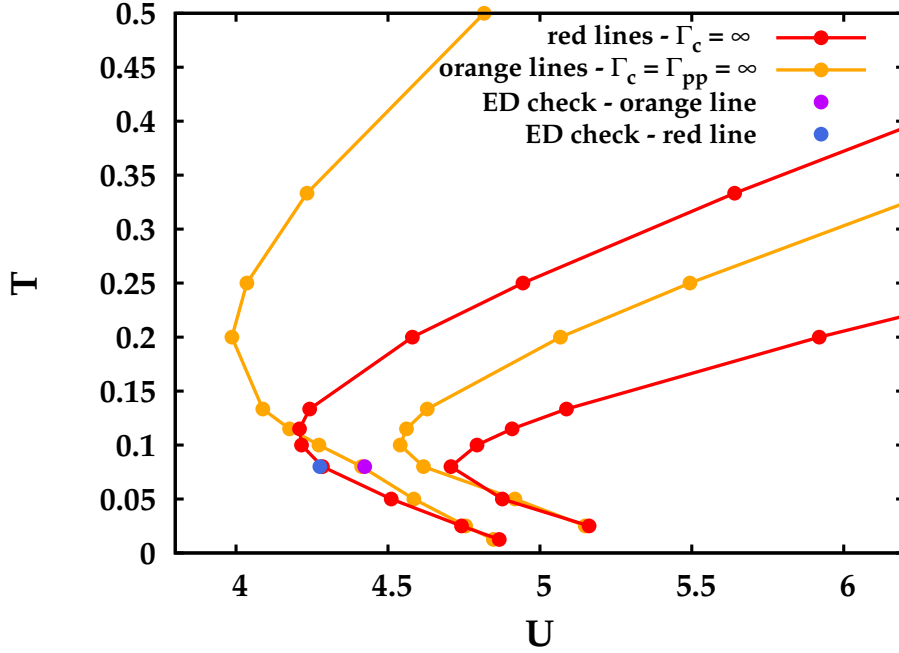


Figure 4.8: Results of the ED calculations of  $\tilde{U}$  for the second red line (blue) and the first orange line (magenta) at  $\beta = 12.5$  together with the phase diagram obtained using *w2dynamics*. As it can be seen, though slight differences occur due to the discretization of the ED-bath, the line crossing is still very clearly observed.

the ED calculations, demonstrating that this is not merely an artefact of the *w2dynamics* calculation, but a true feature of the divergence lines of the AIM.

After verifying the numerical reliability of the observed crossing of divergence lines, one must ask if this is in conflict to any aspect of the current understanding of the irreducible vertex divergences.

One of the most important progress recently achieved [9] regards the crossing of unphysical and physical solutions described in Sec. 2.2. Analysing Fig. 2.11, where such a crossing of physical and unphysical solutions for the case of the *Hubbard atom* is discussed, one can see that the first red and orange line do indeed cross themselves, but that this does happen away from the physical solution. One could in principle, however, imagine that for other cases (such as the AIM), a different situation occurs, where this crossing of unphysical solutions is shifted towards the physical solution. In this perspective, one can conclude that the previously unobserved crossing of divergence lines reported in this master thesis is somewhat surprising, but at least not in conflict with the current understanding of irreducible vertex



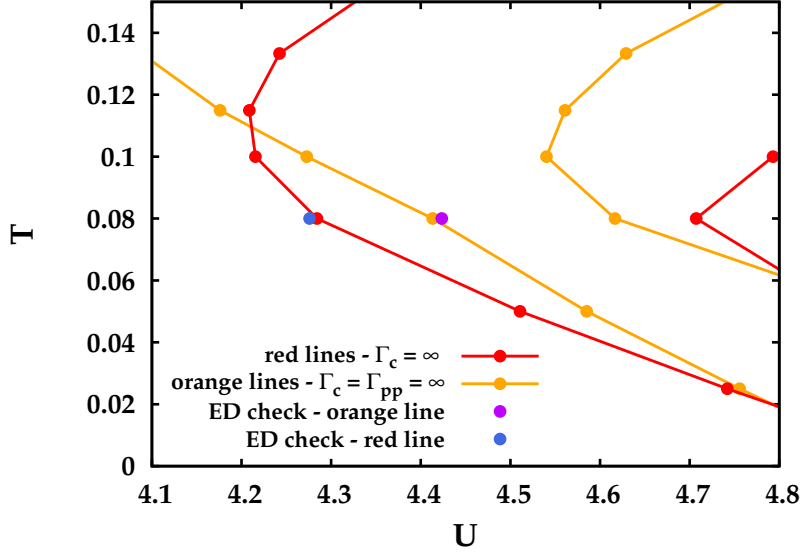


Figure 4.9: As Fig. 4.8, with a zoom onto the area of interest, to show the actual size of the slight discrepancy in  $\tilde{U}$  induced by the discretization error of ED.

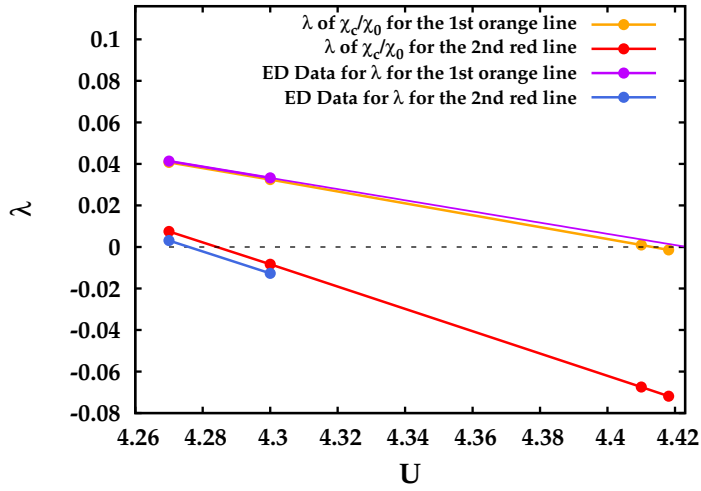


Figure 4.10: Results of the *w2dynamics* and the ED calculation for the eigenvalues of the generalized susceptibility in the charge channel. A slight difference in the eigenvalues is observed, which causes the corresponding minor discrepancy in  $\tilde{U}$  depicted in Fig. 4.8 and Fig. 4.9.

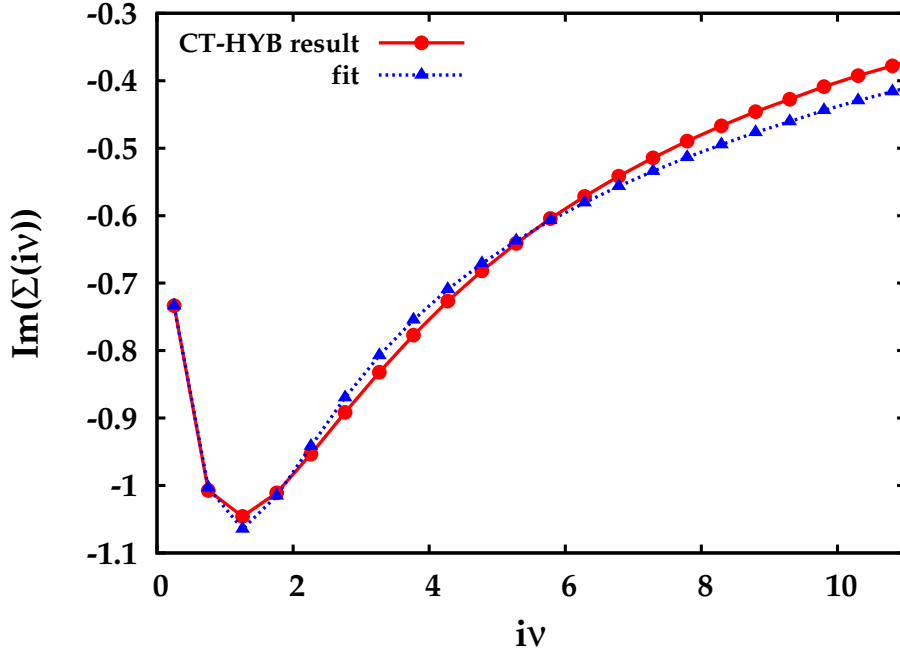


Figure 4.11: Comparison of the imaginary part of the *w2dynamics* self-energy to the one obtained from the bath fit of the ED calculation with four bath sites. The four bath sites are not enough to exactly reproduce the right behaviour of  $Im\Sigma$ , but the overall agreement is sufficient for our scopes.

divergences [9].

What is most remarkable about this result, however, is that it is hitherto only observed for the AIM, and *not* for the DMFT solution of the *Hubbard model*. In the appendix B of [2], where a low-temperature zoom of the phase diagram of the *Hubbard model* is shown, it can be seen that, although the orange and red divergence lines are extremely close to one another, they never cross. In the light of these findings, we suggest to carefully recheck the delicate DMFT low-temperature calculations of [2], to verify whether any occurrence of line crossings might have been overlooked. If this is not the case, one must conclude that the DMFT self-consistency cycle - and the associated strong renormalization of the low-energy part of the electronic bath - is somehow related to the ordering of divergence lines at low temperatures, which could be a quite intriguing topic to investigate in future studies.

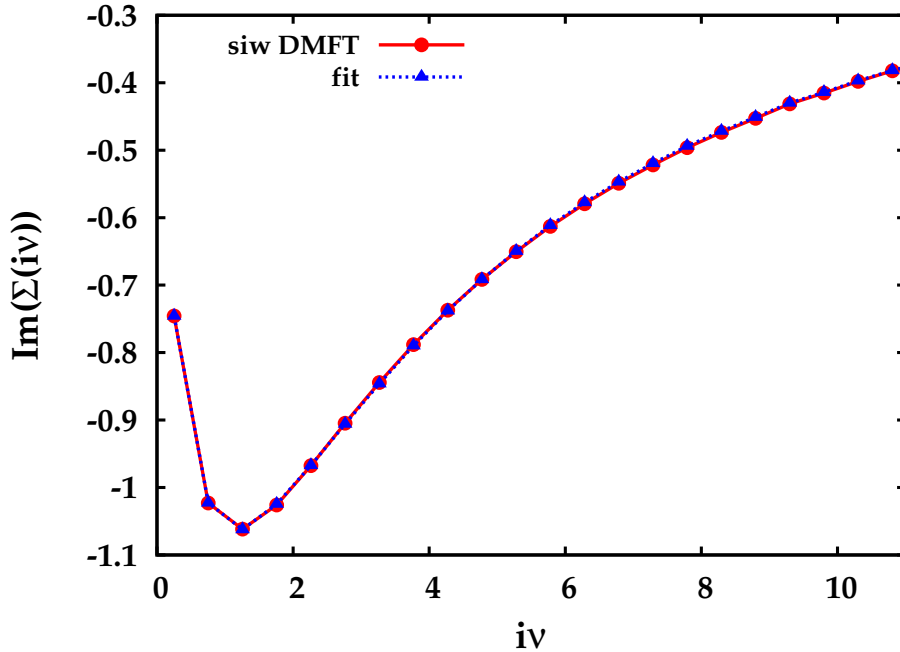


Figure 4.12: As Fig. 4.12 with six bath sites, which are sufficient for obtaining the right imaginary part of the self-energy.

## 4.2 Evolution of the singular eigenvectors

After discussing the first five divergence lines of the AIM obtained throughout this thesis, we want to study the corresponding singular eigenvectors  $V_c$ , i.e. those connected to the five lowest eigenvalues of the generalized susceptibility in the charge channel. As a short summary of the most important features of  $V_c$  introduced in Sec. 2.1 and Sec. 2.2 let us state here: The frequency structure of the singular eigenvector, i.e. whether the weight of  $V_r$  ( $r$  corresponds to the charge  $c$  or the particle-particle up-down  $pp$  channel) is localized or not, is governing at which frequencies the divergence of the irreducible vertex function can be observed. For the *Falicov Kimball* as well as the *Hubbard atom* two different kinds of vertex divergences, and correspondingly two different kinds of eigenvectors are found, which are either completely localized (red divergence lines) or not localized in frequency space (orange divergence lines). Remarkably the frequency localized structure of the first kind of eigenvectors is independent of the temperature, except of the trivial dependence originating from the definition of the Matsubara frequencies themselves.

For the *Hubbard model*, on the other hand, this is no longer the case as localized eigenvectors can be found only in the large  $U$ , high  $T$  limit, whereas

the eigenvectors progressively gain weight at more and more Matsubara frequencies, when the temperature is reduced.

Let us also note that the eigenvectors of the generalized susceptibility in the particle-particle up-down channel, where a simultaneous vertex divergence along the orange divergence lines takes place, are for the AIM *exactly* the same as in the case of the charge channel. For this reason, they are not shown in this thesis, except in Fig. 4.13, where the equivalence of the corresponding eigenvectors is explicitly demonstrated for a given interaction value and  $T = 0.025$ .

In the first subsection the effect of the temperature on the frequency structure of the singular eigenvectors  $V_c$  is studied, followed by a direct comparison of the  $V_c$ 's corresponding to given divergence lines. Afterwards, the even (orange divergence lines)/odd (red divergence lines) symmetry of the eigenvectors and a possible relation to the Green's function is investigated, before in the last part of this section the role of the interaction is discussed.

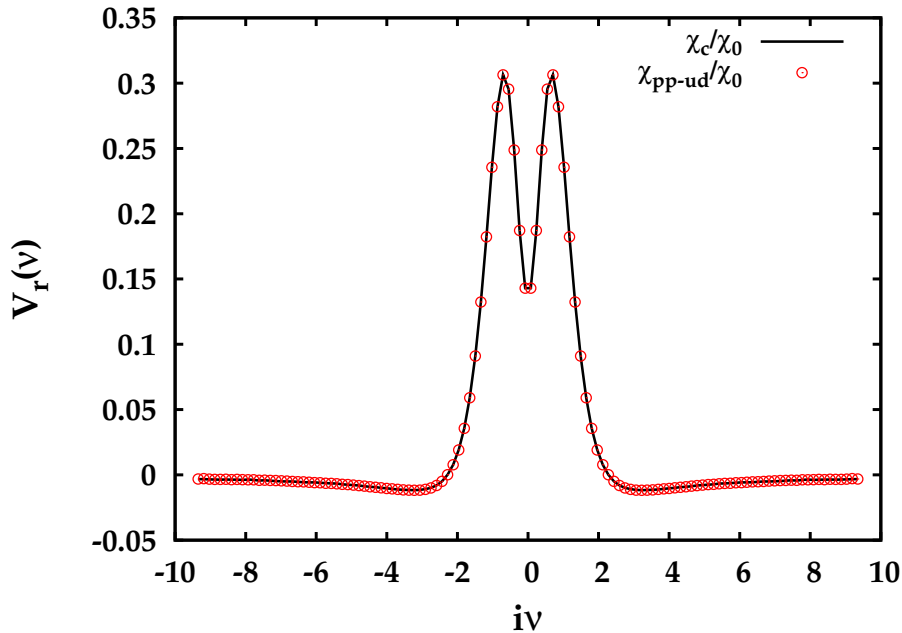


Figure 4.13: Comparison of the corresponding eigenvectors of the generalized susceptibility in the charge ( $r=c$  - black solid line) and the particle-particle up-down ( $r=pp-ud$  - red dots) channel. Evidently, the eigenvectors are exactly the same.

### 4.2.1 Evolution of the singular eigenvectors - along a given divergence line for different temperatures

In a preceding *Projektarbeit* [50] the  $V_c$ 's of the first red divergence line of the AIM for different temperatures were already discussed in great detail. In a similar fashion, our new results for different temperatures along the other four calculated divergence lines are reported and analysed in the following.

The singular eigenvectors  $V_c$  of a given divergence line are shown in Fig. 4.14 to Fig. 4.21, where they are plotted in the basis of Matsubara frequencies ( $i\nu$ ) for several temperatures. It can be readily seen that, for all cases at high temperatures the eigenvectors  $V_c$  are localized in frequency space, i.e. their components have finite weight only at a few Matsubara frequencies. This agrees, asymptotically, with the results for the *Hubbard atom*, where the singular eigenvector has finite weight only at the one Matsubara frequency corresponding to the energy scale  $\nu^*$  (see Sec. 2.2). By reducing the temperature, however, components at other Matsubara frequencies gain weight. This effect was already observed for the first divergence line, as reported in [50], and reflects that no single energy scale, like in the *Hubbard atom* case, can any longer be identified as "responsible" for all the multiple vertex divergences.

Besides these considerations, note that in Figs. 4.14 to 4.21 it looks as if the largest contributions of the low-temperature eigenvectors are located approximately at the same frequency. This was also already discussed to some extent in the previous work [50] and shall be analysed now in greater detail. In Fig. 4.22, the  $V_c$ 's of the *second* red divergence line for the highest temperatures are shown. The eigenvectors are plotted as a function of  $i\nu \cdot \beta$ , which evaluates to a prefactor times the Matsubara index  $n$  (i.e.  $2n - 1$ ). Note that only the parts of the antisymmetric  $V_c$ 's for positive Matsubara indices are reported. For the highest temperatures (in Fig. 4.22 plotted in different variations of red) the only relevant contribution is found at the *second* Matsubara index. This agrees again perfectly with the insights gained from the *Hubbard atom*. By lowering the temperature, components at other indices gain weight, i.e. the eigenvector "broadens", the largest contribution, however, remains still located at the second index. This allows us to relate the singular eigenvectors shown in Fig. 4.22 to the ones of the *Hubbard atom*, which are given by a delta function at the second Matsubara index for all temperatures. Hence, the observed broadening could be approximately described in terms of a transformation of the delta shaped eigenvectors of the *Hubbard atom* into a Lorentzian. In Fig. 4.22 in green color, the  $V_c$  for the temperature of the re-entrance of the corresponding second red divergence line is shown. It is evident that here the shape of the eigenvector can still

be understood as described above, to some extent. In Fig. 4.23 the  $V_c$ 's corresponding to the temperatures lower than the re-entrance point are shown additionally to the ones of Fig. 4.22. Starting from the eigenvector plotted in light-blue color, which still has the largest contribution at the same index as in the *Hubbard atom* case, the maximum of the  $V_c$ 's progressively shifts as the temperature is decreased. As a result, the eigenvectors show a qualitatively different behaviour for temperatures higher or lower than the re-entrance point, corresponding to the eigenvector plotted in green color.

We should note that the situation is exactly mirrored in the opposite trend of the largest component of  $V_c$  as a function of Matsubara frequencies ( $i\nu$ ), instead of the Matsubara index  $n$ . In Fig. 4.24 the eigenvectors shown in Fig. 4.23 are plotted as a function of ( $i\nu$ ). Here it can be clearly seen, that the largest contribution of the eigenvectors corresponding to temperatures lower than the re-entrance point remains located to an (almost) constant frequency independently of the temperature, while for temperatures higher than the re-entrance, a progressive shift of the largest component to higher ( $i\nu$ ) is observed.

As it has been demonstrated in [2] and recalled in Sec. 2.2, divergences controlled by a unique energy scale are associated to localized singular eigenvectors, fully defined by in terms of the index  $n$ . Hence, the nature of the divergences above/below the re-entrance is completely different, in that the existence of a unique energy scale is no longer possible below that border.

The results substantiate the discussion made for the Kondo scale in Sec. 4.1, as a boundary between two regimes. The first one, at higher temperatures, is a regime to a given extent related to the *Hubbard atom* case and the second one, at low temperatures, corresponds to a region where the appearance of the low-energy Kondo resonance drives a qualitatively different behaviour.

A further verification of this role played by the re-entrance point is provided by Fig. 4.25 and Fig. 4.26, where analogously to Fig. 4.22 and Fig. 4.23 the eigenvectors of the *third* red line (for which fewer low-temperature results exist) are shown. Here, the same explanation applies.

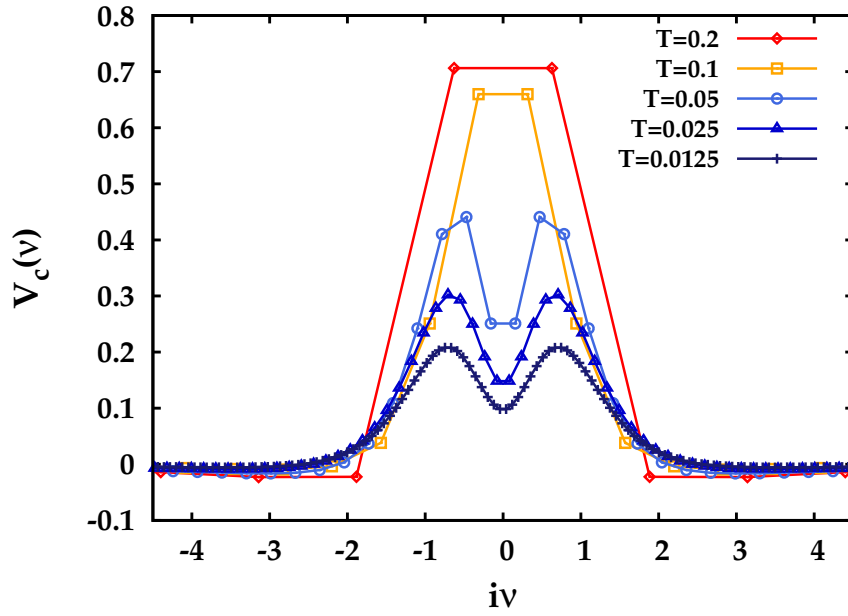


Figure 4.14: Singular eigenvectors of the generalized susceptibility in the charge channel for several temperatures of the first orange divergence line, plotted as a function of Matsubara frequencies.

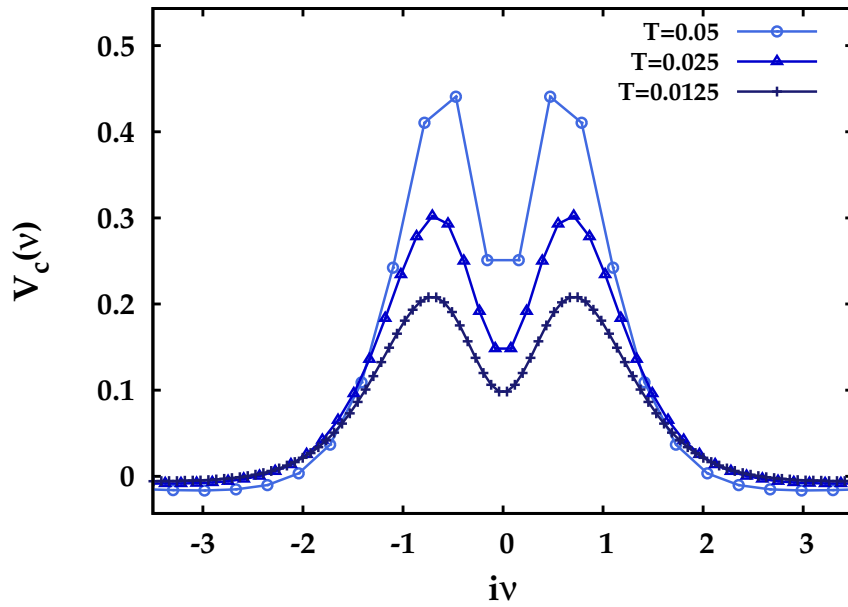


Figure 4.15: As Fig. 4.14, reporting, in an enlarged scale, solely the results for low temperatures. Here it can be seen, that the location of the maximum contribution of the eigenvectors stays constant for low enough temperatures.

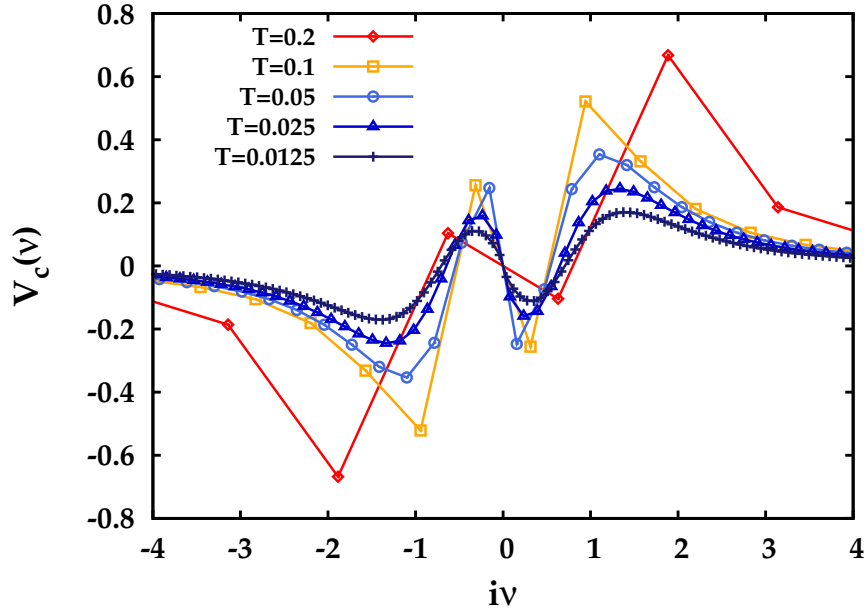


Figure 4.16: Singular eigenvectors of the generalized susceptibility in the charge channel for several temperatures of the second red divergence line, plotted as a function of Matsubara frequencies.

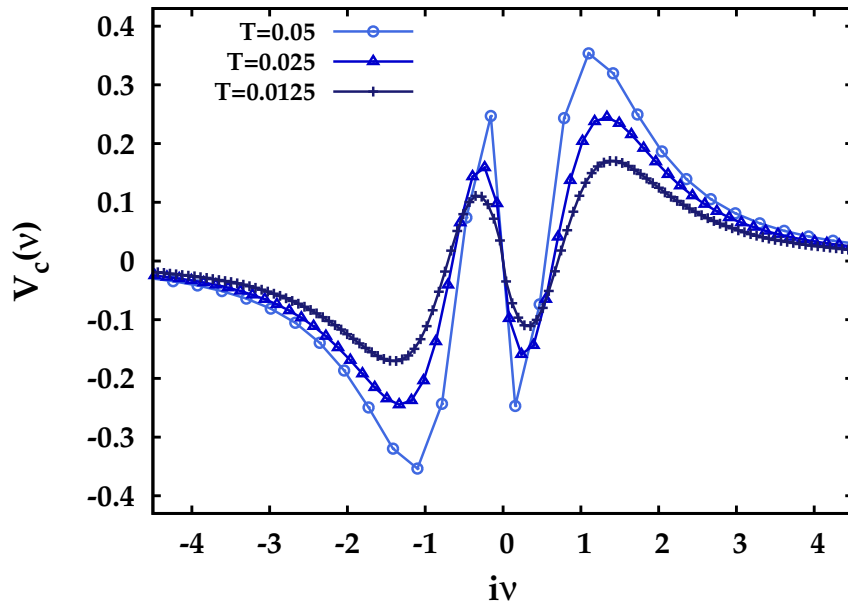


Figure 4.17: As Fig. 4.16, reporting, in an enlarged scale, solely the results for low temperatures. Here it can be seen, that the location of the maximum contribution of the eigenvectors stays constant for low enough temperatures.



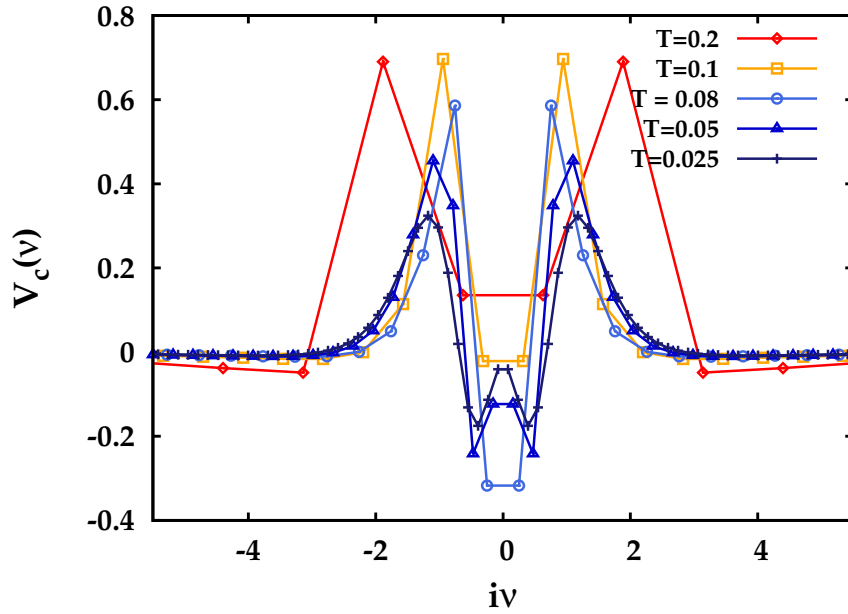


Figure 4.18: Singular eigenvectors of the generalized susceptibility in the charge channel for several temperatures of the second orange divergence line, plotted as a function of Matsubara frequencies.

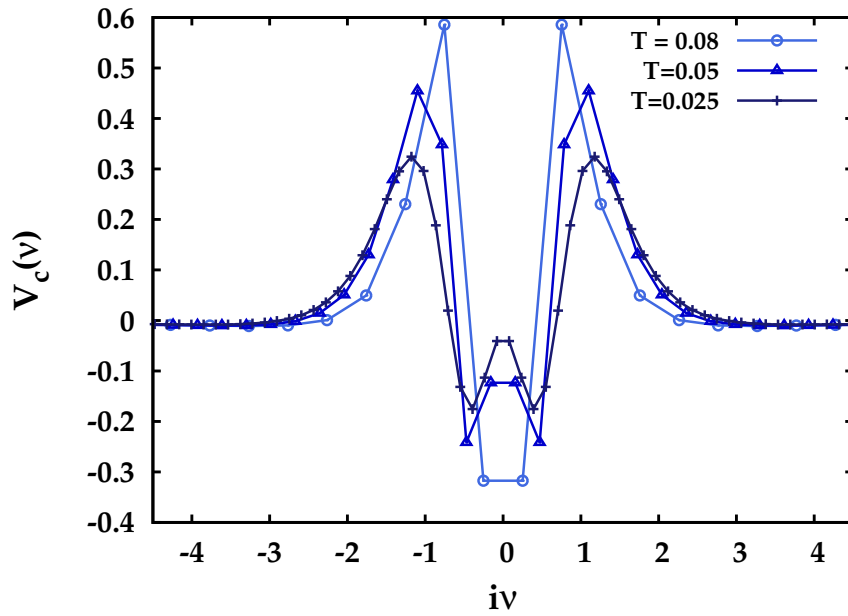


Figure 4.19: As Fig.4.18, reporting, in an enlarged scale, solely the results for low temperatures. The constant location of the maximum contribution of the eigenvectors can hardly be seen here, as not enough low-temperatures exist.

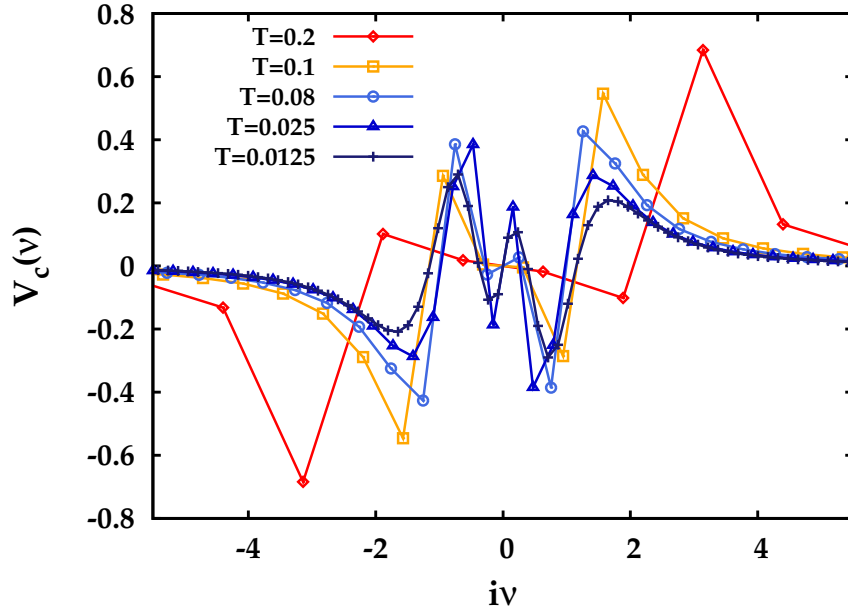


Figure 4.20: Singular eigenvectors of the generalized susceptibility in the charge channel for several temperatures of the third red divergence line, plotted as a function of Matsubara frequencies.

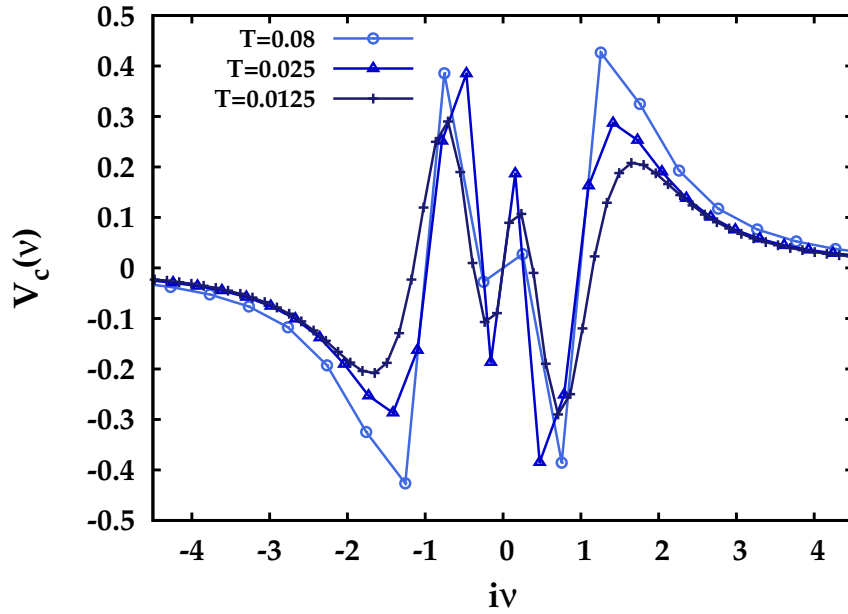


Figure 4.21: As Fig. 4.20, reporting, in an enlarged scale, solely the results for low temperatures. The constant location of the maximum contribution of the eigenvectors can hardly be seen here, as not enough low-temperatures exist.

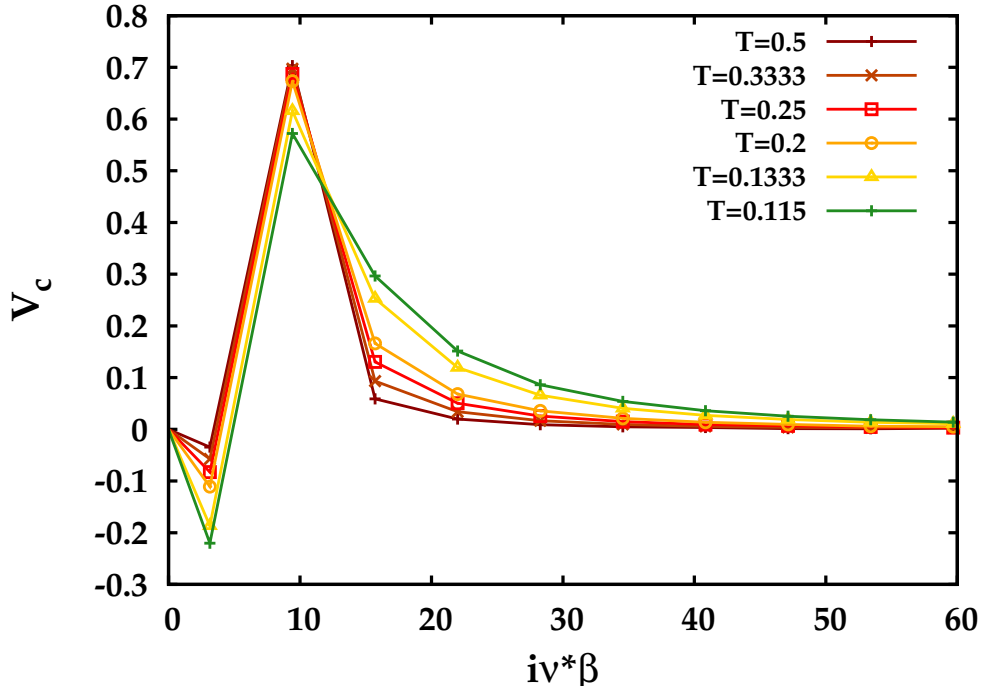


Figure 4.22: Singular eigenvectors of the generalized susceptibility in the charge channel for several temperatures of the *second* red divergence line, plotted as a function of the product  $i\nu \cdot \beta$ , which corresponds to  $(2n-1)$ . By this representation, the relation to the results of the *Hubbard atom* can be seen very well, as, for high enough temperatures, the largest contribution is always found at the *second* Matsubara index. For the eigenvectors plotted in different orange color-tones, as well as for the one shown in green, one can still see the relation to the delta peak shaped frequency structure of the eigenvectors of the atomic limit, only broadened into a Lorentzian shape. The eigenvector plotted in green color corresponds to the temperature where the re-entrance point of the associated divergence line is found.

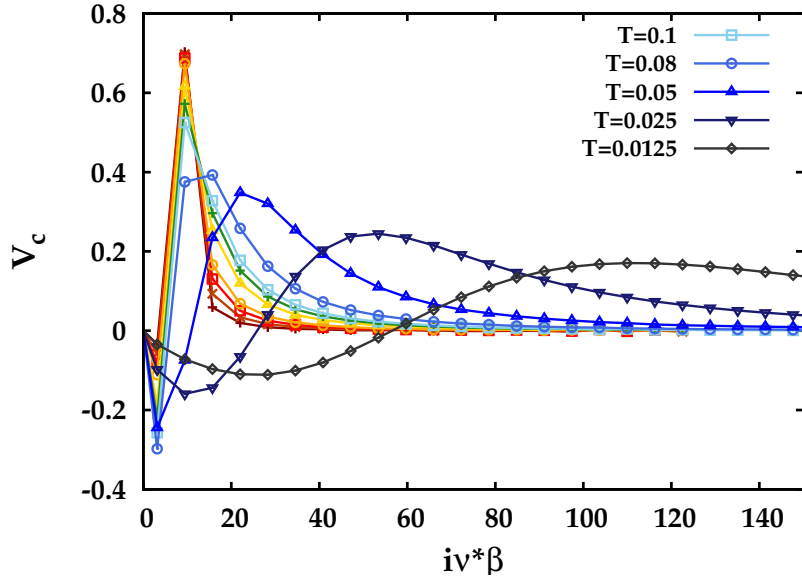


Figure 4.23: As Fig.4.22, but showing also the results for temperatures lower than the one of the re-entrance point. Evidently, the relation to the singular eigenvectors of the *Hubbard atom* can no longer be established, as the maximum is now shifting to the right.

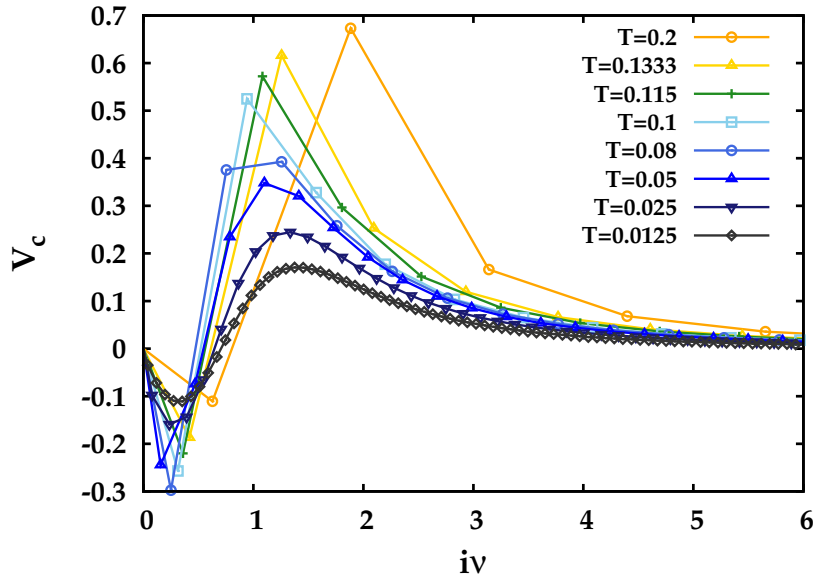


Figure 4.24: As Fig.4.23, but the eigenvectors are plotted now as a function of the Matsubara frequencies. Here, it can be seen that the largest contribution of the eigenvectors is found at the same Matsubara frequency, if the temperature is decreased below the one of the re-entrance point.

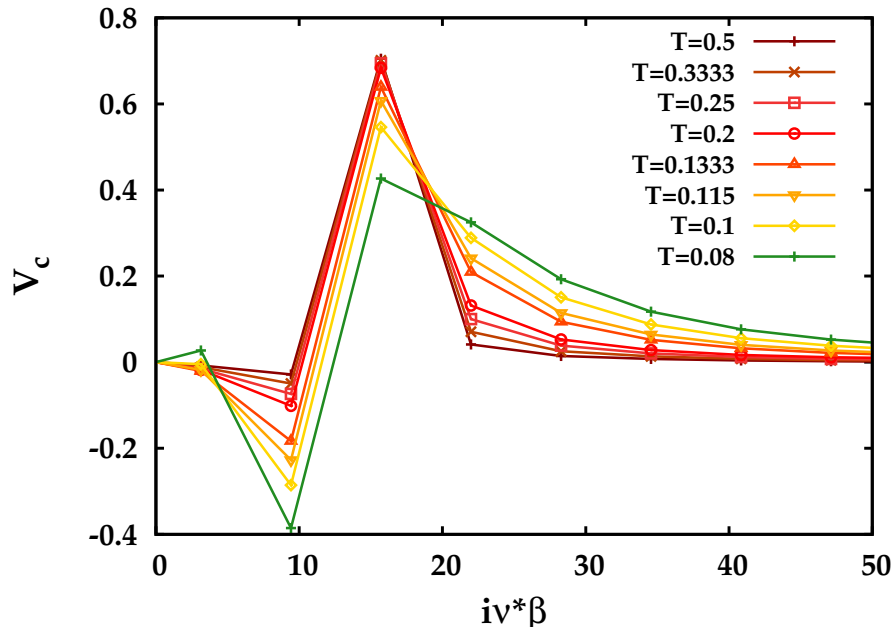


Figure 4.25: As Fig. 4.22 for the third red divergence line.

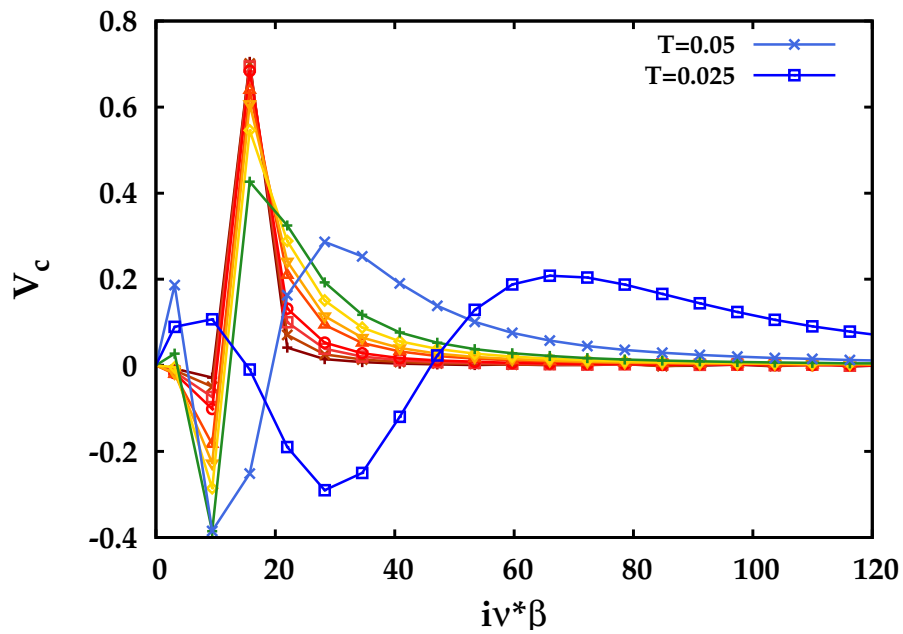


Figure 4.26: As Fig. 4.23, for the third red divergence line. Note that for this divergence line fewer results in the low-temperature regime have been computed hitherto.

## 4.2.2 Evolution of the singular eigenvectors - comparison for different divergence lines

As described in the beginning of this section, the singular eigenvectors show a "broadening" with decreasing the temperature if plotted as a function of Matsubara indices. This indicates that no single energy scale can be responsible any more for the irreducible vertex divergences. However, it turns out that it is also very intriguing to compare the eigenvectors of different divergence lines with one another, as it will be discussed below. Note that here also the "broadening" will be discussed shortly, described in great detail in the previous chapter.

In Fig. 4.27 the singular eigenvectors of the charge channel of the three red divergence lines calculated over the course of this thesis are compared for the same temperature ( $T = 0.025$ ). In gray the corresponding singular eigenvectors at the highest temperature value reached during the calculations ( $T = 0.5$ ) is shown <sup>1</sup>. The gray eigenvectors show a perfect agreement with the insights provided by the results of the *Hubbard atom*. As discussed in Sec. 2.2 and also in Sec. 4.2.1, for the *Hubbard atom* an energy scale  $\nu^*$  could be identified, yielding an irreducible vertex divergence soon as a Matsubara frequency is equal to this scale. This allowed, in turn, for the identification of the multiple divergence lines with single Matsubara frequencies, which corresponded eventually to those Matsubara frequencies where the localized singular eigenvectors have finite weight.

This can be seen in Fig. 4.27, where for the first divergence line (top panel) the gray eigenvector displays its largest contribution at the first Matsubara frequency. Note that this agreement is clearly not perfect, as the atomic limit is not fully reached, in the parameter regime considered, see the discussion made for Fig. 4.2.

In any case, also the other eigenvectors, corresponding to the second and third divergence line (middle and top panel) for  $T = 0.5$  can be understood in the same manner, as they show the largest contribution at the second or third Matsubara frequency, respectively. Comparing the eigenvectors plotted in gray to the eigenvectors plotted in red (i.e., red for the first red divergence line, light-red for the second red and dark-red for the third red line) one notices that this largest contribution is shifted towards higher frequencies, as discussed in great detail in the previous section. At the same time, at low frequencies a "structure" is emerging: For the eigenvector of the second divergence line (middle panel) a local maximum and a local minimum appear,

---

<sup>1</sup>Note that for a better representation of the features we intend to discuss, the eigenvectors of  $T = 0.5$  are rescaled by a factor of 0.45.

leading to 3 "nodes" in their frequency components. In the case of the third line (bottom panel) the corresponding eigenvector has 5 "nodes", and, thus, a minimum and maximum more. Extrapolating the behaviour observed for the three eigenvectors, one can infer that the eigenvector of the  $n$ -th red divergence line will have  $2n - 1$  "nodes". As the interpretation of the singular eigenvectors of the generalized susceptibility is lacking, it is still unclear at the moment, what the meaning of this elusive low-frequency "structure" is.

After analysing the eigenvectors of the red divergence lines only, a similar comparison can be eventually made for the eigenvectors of the red and orange divergence lines, shown in Fig. 4.28. In the upper panel the eigenvector corresponding to the first red and orange divergence line are plotted in red and orange, respectively, for the same temperature  $T = 0.025$ . Analogously, in the lower panel, the eigenvectors corresponding to the second divergence lines are reported. The eigenvectors of the orange lines look, to a rough extent, as a "symmetrized" version of the antisymmetric eigenvectors corresponding to the red divergence lines. This, hitherto unexploited, feature is very helpful for rigorously classifying the two kinds of divergences, as argued in the following section.

### 4.2.3 Symmetry of the singular eigenvectors

As a consequence of the temperature evolution of the singular eigenvectors discussed above and the considerations made in Sec. 2.2 concerning the distinction criterion of the two kinds of vertex divergences, i.e., the locality of the eigenvector, it becomes clear that a specific difficulty arises: As seen in Figs. 4.22 to Fig. 4.26, as well as Fig. 4.27, the eigenvector "broadens", i.e. it gains weight at all Matsubara frequencies. This means obviously that the locality of the eigenvector does no longer represent a valid distinction criterion between the two kinds of vertex divergences introduced in Sec. 2.1. However, as explained in Sec. 4.2.2 in the discussion of Fig. 4.28, the symmetry of the eigenvectors could still be. In fact, the even/odd symmetry of the eigenvectors  $V_c$  remains *always* preserved in the two different classes of vertex divergences. More precisely, for the first kind of vertex divergences (always depicted in red color), which in Sec. 2.1 was classified as the localized one, the eigenvectors are for all temperatures *antisymmetric* under the transformation  $i\nu \rightarrow -i\nu$ . In the case of the other kind of divergences (depicted always in orange) the eigenvector is *symmetric*. As a result, the frequency symmetry of  $V_c(\nu)$  can be adopted as a clear-cut criterion, valid at all temperatures, to classify the divergence lines in the (half-filled) AIM. Moreover the symmetry of the eigenvectors is directly reflected in the shape of the irreducible vertex function. In the Figs. 4.29 and 4.30 the influence of the symmetry of the  $V_c$ 's

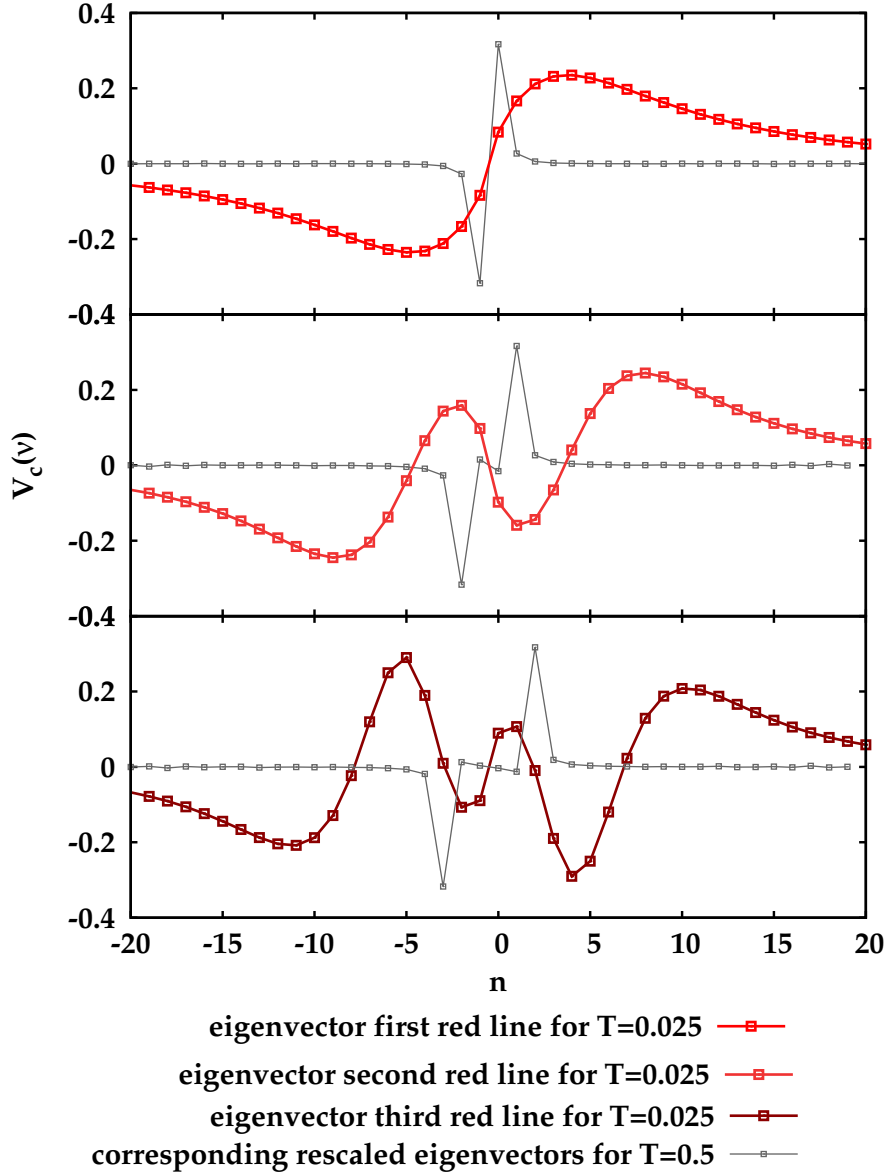


Figure 4.27: Top panel: Singular eigenvector for  $T = 0.025$  (red) and  $T = 0.5$  (gray) of the first red divergence line. Middle panel: Eigenvector  $T = 0.025$  (red) and  $T = 0.5$  (gray) of the second red divergence line. Bottom panel: As middle and top panel, only for the third red divergence line. All eigenvectors correspond to vanishing eigenvalues of the generalized susceptibility in the charge channel. From this comparison one can see that the eigenvectors at the high temperature value (gray) agree precisely with the insights of the *Hubbard atom*, i.e. they are localized with finite weight at the Matsubara frequency corresponding to the irreducible vertex divergence. The eigenvectors plotted in red display not only the "broadening" discussed in Sec. 4.2.1 but also the emergence of a characteristic low-frequency structure.



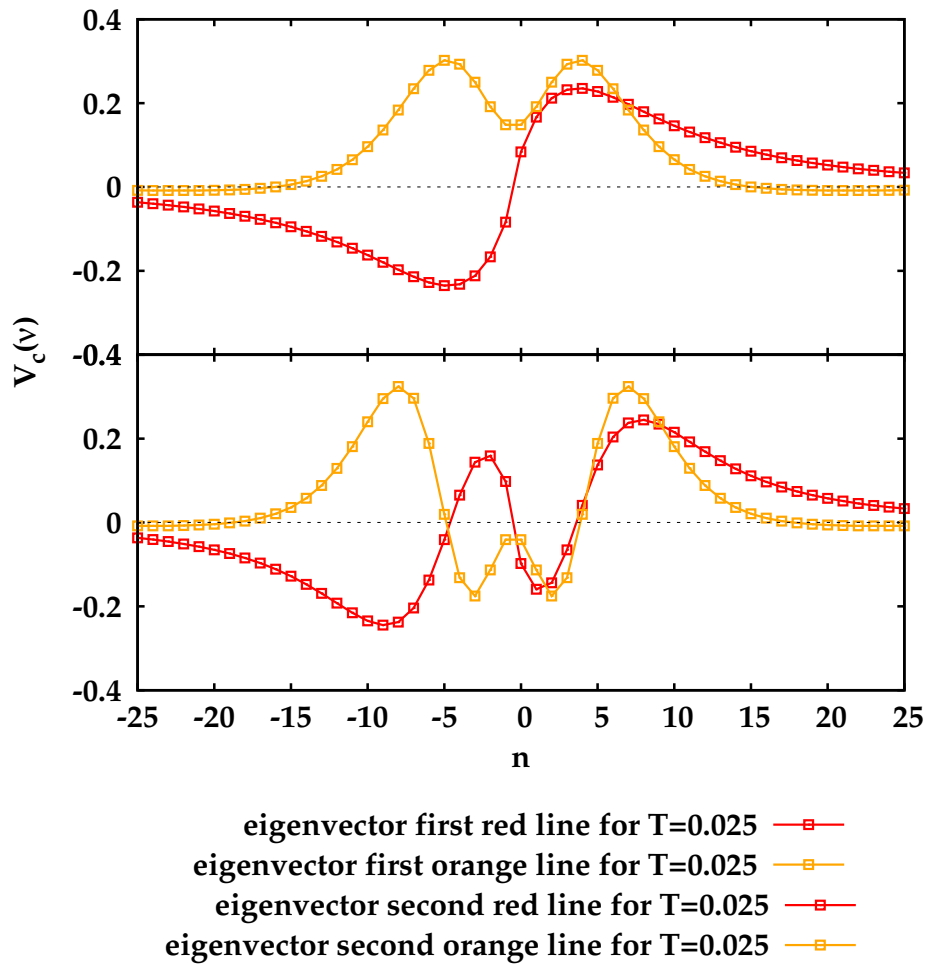


Figure 4.28: Upper panel: Comparison of the eigenvectors of the first red and orange divergence line for  $T = 0.025$ , plotted in red and orange, respectively. Lower panel: Same comparison made for the second divergence lines, respectively. It appears, that the orange eigenvectors can be regarded, to some extent, as the "symmetrized" version of the antisymmetric red eigenvectors.

onto the shape of the irreducible vertex function is illustrated. In the left inset of both figures the smallest eigenvalues are shown. In particular, we are considering a case where the calculations have been performed between the second red and the first orange divergence line, in a parameter regime where the two lines are very close to each other. In the first case, shown in the left inset of Fig. 4.29, the red dot marks the eigenvalue closest to zero, which, in this case, corresponds to a red divergence with an antisymmetric eigenvector plotted in the inset on the right side. In the main panel, where the irreducible vertex function in the charge channel,  $\Gamma_c$ , is shown, it can be easily seen that  $\Gamma_c$  has almost the same frequency structure as the eigenvector. This can also be understood from the considerations made in Sec. 2.1, which we want to summarize here shortly: The irreducible vertex in the charge channel is governed by the inverse of the corresponding generalized susceptibility, given in the expression below

$$[\chi_c]_{\nu\nu'}^{-1} = \sum_i (V_{i,\nu'})^* (\lambda_i)^{-1} V_{i,\nu} \quad . \quad (4.1)$$

From this relation one sees immediately that the eigenvector  $\tilde{V}_{i,\nu}$ , and by that also the associated symmetry, corresponding to the eigenvalue closest to zero ( $\tilde{\lambda}_i \approx 0$ ), is crucial for the frequency structure of  $\Gamma_c$ :

$$[\Gamma_c]_{\nu\nu'} \approx [\chi_c]_{\nu\nu'}^{-1} \approx (\tilde{\lambda}_i)^{-1} (\tilde{V}_{i,\nu'})^* \tilde{V}_{i,\nu} \quad (4.2)$$

This can also be seen in the second example shown in Fig. 4.30. Here, the interaction value was changed only marginally, nevertheless, as it can be seen in the left inset, the eigenvalues corresponding to the first orange divergence line are now the closest to zero. This leads to an almost perfectly symmetric vertex function due to the dominance of the corresponding symmetric eigenvector in the sum of Eq. 4.1.

Evidently, the correspondence between the frequency symmetries of  $V_c(\nu)$  and  $\Gamma_c$  holds rigorously at the divergence line, i.e. at calculations performed at  $\tilde{U}$ . Otherwise, several small eigenvalues can give a large contribution, especially in calculations performed not in the proximity of a vertex divergence. As an example, one could imagine to perform a calculation at an interaction value in between the two selected for Fig. 4.29 and Fig 4.30. In such a case the irreducible vertex function will not have a clear symmetry. This will also be the case for  $\Gamma_c$  at the crossing of the divergence lines, described in Sec. 4.1.

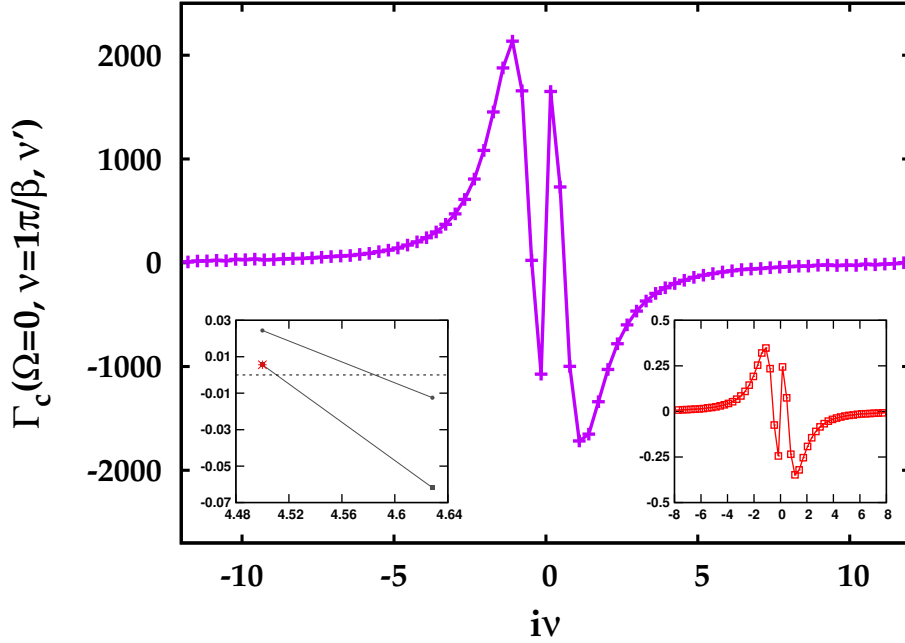


Figure 4.29: Irreducible vertex function in the charge channel for  $\Omega = 0$ , a fixed  $\nu$  and a variable  $\nu'$ . This calculation was performed at the interaction value  $U=4.5$  and  $T = 0.05$ , which is in the proximity of the second red divergence line. Left inset: Small eigenvalues of the generalized susceptibility are shown. The red dot marks the smallest one, corresponding to a divergence in the charge channel only, i.e. a red divergence line. Right inset: The antisymmetric eigenvector corresponding to the smallest eigenvalue depicted in the left inset in red, is shown. As it can be seen in the main panel,  $\Gamma_c$  has almost exactly the same frequency structure.

#### 4.2.4 Relation of the vertex divergences and the Green's function

After discussing several features of the singular eigenvectors, now their relation to the Green's function will be investigated. At this scope we will briefly reconsider the irreducible vertex divergences of the *Binary Mixture* [2] (see Sec. 2.2). For this simple disordered model the vertex divergences, and by that the underlying energy scale  $\nu^*$ , could be related to the spectral gap formation due to the connection of  $\nu^*$  and the minimum of the Green's function. As it turns out, a somewhat similar relation, can also be found for the irreducible vertex divergences of the *Hubbard atom* [51]. Starting from the Green's function of the *Hubbard atom*, given in Eq. 4.3 as a function of

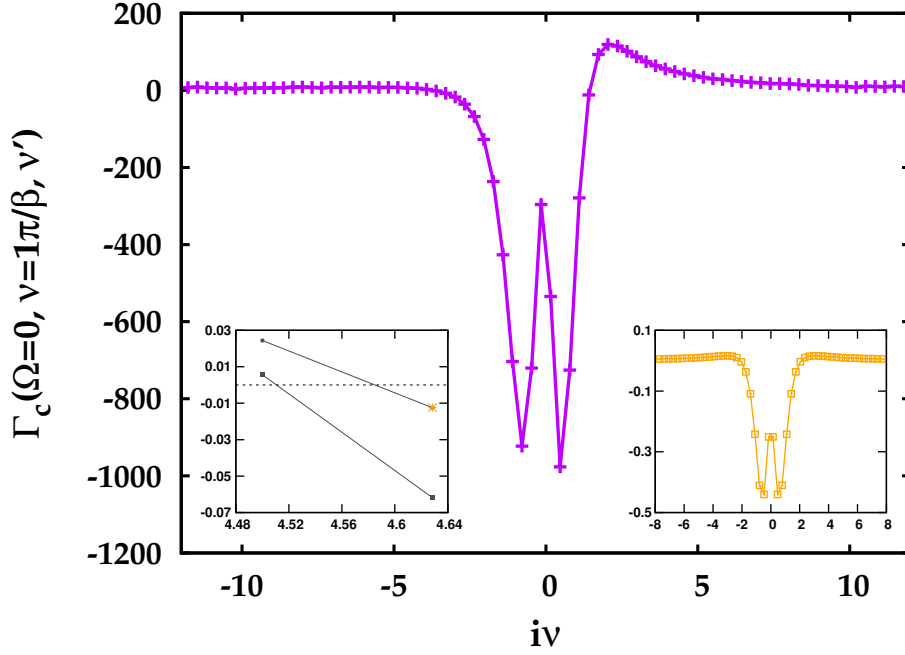


Figure 4.30: As Fig.4.29, only now at  $U=4.62$ , which is in the proximity of the first orange divergence line. In the left inset it can be seen that the other eigenvalue in the charge channel (the one of the particle-particle up-down is not shown, vanishes however at the same  $\tilde{U}$ ) is now the smallest. As a result, here the shape of the vertex function is essentially governed by the corresponding symmetric eigenvector, shown in the right inset.

Matsubara frequencies

$$\begin{aligned}
 G(\nu) &= \frac{1}{2} \left( \frac{1}{i\nu + \frac{U}{2}} + \frac{1}{i\nu - \frac{U}{2}} \right) \\
 &= -\frac{i\nu}{\nu^2 + \frac{U^2}{4}},
 \end{aligned} \tag{4.3}$$

one can easily verify that the second derivative is zero at the interaction value  $\frac{\sqrt{3}}{2}U$ . This expression, however, is equal to the energy scale  $\nu^* = \frac{\sqrt{3}}{2}U$  related to the irreducible vertex divergences of the *Hubbard atom*. Summarizing shortly the discussion made in Sec.2.2 for the vertex divergences of this model: As soon as a Matsubara frequency is equal to  $\nu^*$ , a divergence takes place at this frequency, and the only non-zero contribution of the corresponding eigenvector is located at this frequency. This means that, in contrast to the *Binary mixture* case where the divergence could be related to the minimum of the Green's function, now for the *Hubbard atom* the di-

vergence is related to the inflection point of the Green's function. Physically the inflection point of a Green's function is an indication for a spectral gap formation, however not as clear as the minimum.

Coming back to our case of the AIM, as seen in the Figs. 4.22 and 4.25 the singular eigenvectors in the high-temperature regime of the phase diagram hardly change and resemble those of the *Hubbard atom case*. Thus, it is interesting to investigate, if also the connection to the Green's function found for the case of the *Hubbard atom* still holds in the case of the AIM. In Figs. 4.31, 4.32 and 4.33 the second derivatives of the Green's function and the Green's functions themselves are shown for the highest temperatures of the third red divergence line. Note that the Green's functions had to be rescaled in order to be able to make visible the changes of the second derivatives in the plots. The second derivative was calculated using a simple numerical differentiation, i.e.,

$$f''(x) \approx \frac{f(x+h) - 2f(x) + f(x-h)}{h^2}$$

We note that, due to this simple implementation, no second derivative for the first frequency can be calculated.

Analysing Fig. 4.31, showing the Green's function and the second derivative for the highest temperature value ( $T = 0.5$ ) of the third red divergence line, it can be seen, that at such high temperatures the relation between the inflection point of the Green's function and the divergences observed for the *Hubbard atom*, is also found in the AIM. Here, the inflection point is located at the *third* Matsubara frequency for the *third* divergence line, and the largest contribution of  $V_c(i\nu)$ , plotted in Fig. 4.25, is exactly at the *third* Matsubara frequency. However, such a connection gets lost at lower temperatures, as the next two Figs. 4.32 and 4.33, corresponding to the temperatures  $T \approx 0.333$  and  $T = 0.2$ , show. In fact, at  $T \approx 0.333$  the inflection point is somewhere between the second and third Matsubara frequency, but at  $T = 0.2$  no inflection point is visible any longer. Quite surprisingly, this already happens at temperatures where the singular eigenvectors of the AIM still largely resemble the very localized ones of the *Hubbard atom*, as it can be seen in Fig. 4.25.

#### 4.2.5 Evolution of the eigenvectors - the role of the interaction $U$

In this subsection, we complete the discussion of the "adiabatic" evolution of singular eigenvectors by studying their dependence on the interaction. At

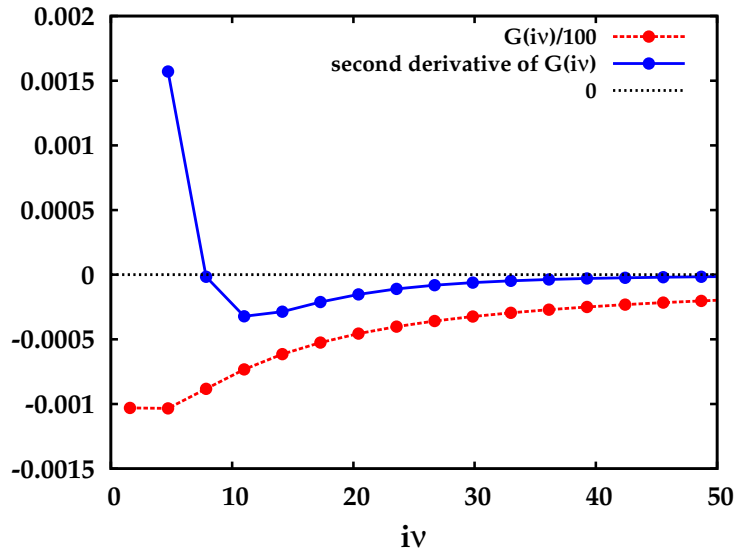


Figure 4.31: Second derivative of the Green's function as a function of Matsubara frequencies (blue solid line) and the rescaled Green's function itself (red dashed line), for  $T = 0.5$  and  $U$  in the proximity of the third red divergence line. As the first blue dot refers to the second Matsubara frequency, the inflection point is located at the third frequency, agreeing with the observations made for the *Hubbard atom*.

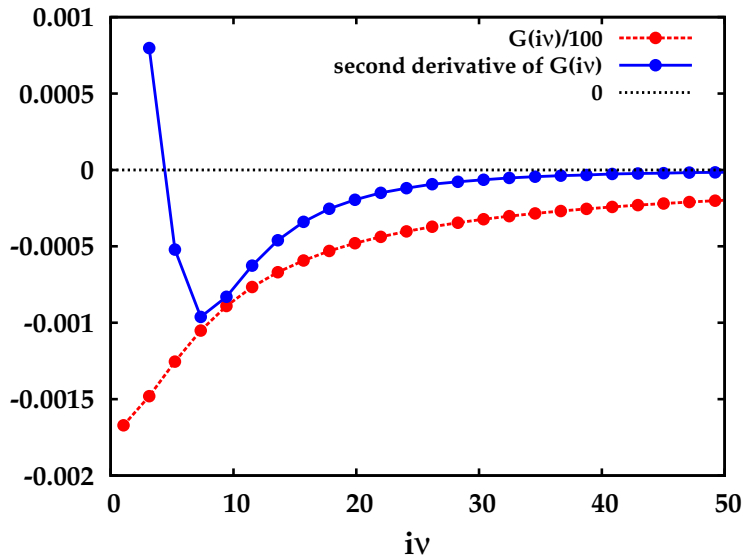


Figure 4.32: As Fig. 4.31 for  $T \approx 0.333$ . The inflection point is no longer at the third frequency, as it starts to shift towards the second.

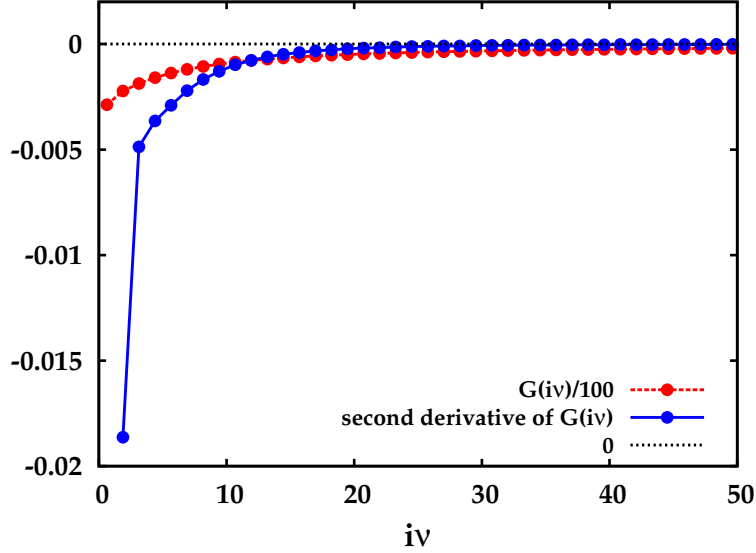


Figure 4.33: As Fig. 4.31 for  $T = 0.2$ . The inflection point is no longer visible in the plot, the Green's function shows a purely metallic behaviour. This implies that the connection of the vertex divergences and the inflection point is lost.

this scope, however, only in this subsection, also non-singular eigenvectors will be shown.

We will analyse how the a variation of  $U$  at the same temperature affects the shape of the two kinds of eigenvectors, which become singular at the corresponding divergence line, i.e. when  $U = \tilde{U}$ .

In Fig. 4.34 and Fig. 4.35 the eigenvectors corresponding to the second and third eigenvalue of the generalized susceptibility which become singular eigenvalues for  $U = \tilde{U}$  (i.e. second red and first orange divergence line), are shown for the temperature  $T = 0.025$  and different interaction values  $U$ . Interestingly, the shape of the asymmetric eigenvectors of the second red line show hardly any influence of the interaction  $U$ . Note that in Fig. 4.34 only the part of the eigenvectors for positive Matsubara frequencies are shown, in order to highlight the very small changes. The opposite happens for the symmetric eigenvectors corresponding to the first orange line, depicted in Fig. 4.35. More precisely, it appears that the Matsubara frequency, where the largest contribution of the eigenvector is located, is essentially unaffected by a change of the interaction, while in the high-frequency tail a strong dependence on the interaction value can be observed.

The implications of this peculiar dependence on the interaction value, only observed for one kind of eigenvectors, i.e. those corresponding to the

orange divergence lines, remain so far unclear.

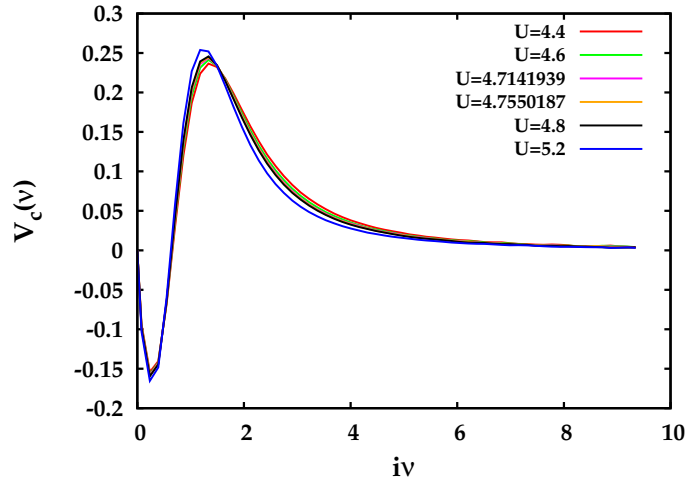


Figure 4.34: Comparison of the antisymmetric eigenvectors corresponding to the second red divergence line for  $T = 0.025$  and several interaction values. Only the positive Matsubara frequency axis is shown, in order to demonstrate the smallness of the variations of  $V_c(\nu)$  as a function of  $U$ . The corresponding  $\tilde{U}$  value for this temperatures is 4.742.

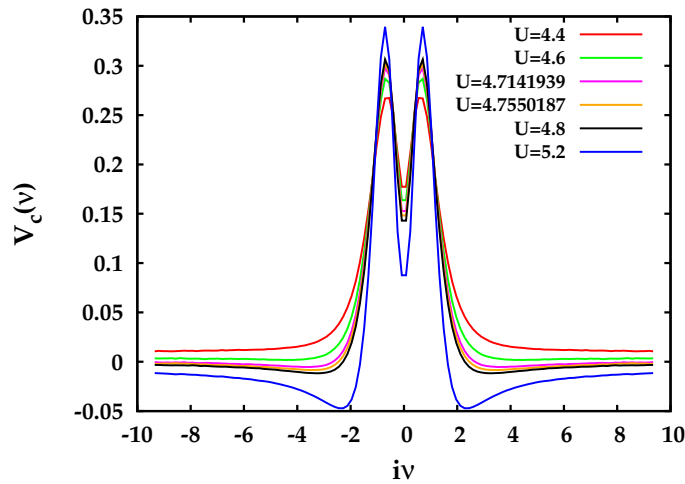


Figure 4.35: Comparison of the symmetric eigenvectors corresponding to the first orange divergence line for  $T = 0.025$  and several interaction values. The corresponding  $\tilde{U}$  value is 4.756. It appears that the interaction has a definitive influence on the tail of the eigenvector components in the high-frequency range. The location of the largest contribution on the other hand seems to remain rather constant.



# Chapter 5

## Conclusions

This thesis was devoted to the discussion of an elusive as much as intriguing feature of quantum many-body theories, the divergences of the irreducible vertex function. Specifically, in this work, the occurrence of such problems has been analysed for a model not yet considered in this perspective: the Anderson impurity model (AIM).

The study of vertex divergences in the AIM allowed for the investigation of two questions of profound importance: Are the vertex divergences related to an occurrence of a Mott transition? What is the role of the Kondo scale, if it has an influence at all?

In the first part of the thesis a short introduction to the general theoretical framework, including also a concise recollection of the latest results from the literature (Chapter 2), as well as a review of the numerical methods to extract the vertex divergences (Chapter 3), is given. In the following Chapter 4, the new results of this master thesis are presented: The irreducible vertex divergences of the Anderson impurity model are precisely described and analysed. As a conclusion, the main findings and their implications are briefly reconsidered in this conclusions chapter.

In particular, as for the results, in Sec. 4.1 the phase diagram of the AIM is shown and compared to the one of the *Hubbard model* solved by means of DMFT [2]. From this comparison, larger similarities than initially expected for have been found, as the divergence lines show qualitatively the same behaviour in the whole phase diagram. More specifically, for both models a re-entrance of the divergence lines is found, i.e. a bending towards higher interaction values in the low-temperature regime and, most importantly, divergences at *finite* interaction values for  $T = 0$  are observed. Note that in the AIM no metal-insulator transition is present at  $T = 0$ , from which it logically follows that the metal-insulator transition must be ruled out as a crucial factor for determining the shape of the divergence lines and the

behaviour of the corresponding eigenvector in the low-temperature regime. This answers the first question that was of central interest for this thesis.

Such a crucial role for the shape of the vertex divergences in the low-temperature regime could be ascribed, instead, to the Kondo scale. In fact, the Kondo scale appears to mark the boundary between two regimes of radically different behaviour of the vertex divergences. The crossing of such a border is reflected in two main aspects: (i) the shape of the divergence lines and (ii) the corresponding singular eigenvectors. As for the first aspect, a regime showing a monotonous (linear or quadratic) behaviour of the divergence lines is found for higher temperatures than the Kondo scale ( $T_K$ ) and it can be clearly distinguished from the regime of lower temperatures. In fact, by crossing  $T_K$  the re-entrance of the divergence lines is observed and rather similar line-shapes in the AIM and the *Hubbard model* are found at low-temperatures, where the Kondo resonance dominates the low-energy physics. As for (ii) results for the temperature evolution of the singular eigenvectors  $V_c(i\nu)$ , discussed in great detail in Sec. 4.2.1, further substantiate the claim that the Kondo scale represents indeed a boundary between two different regimes. In particular, the eigenvectors for higher temperatures, show great similarities with the ones of the *Hubbard atom*, in that way that the largest component of  $V_c(i\nu_n)$  is found at the same Matsubara index  $n$  for different temperatures. For lower temperatures than the Kondo scale, however, the locations of the largest contribution of the singular eigenvectors stay no longer constant at the same Matsubara index, but at the same Matsubara frequency, independent of the temperature. This means that the shape of the eigenvectors can no longer be related to the ones found for the *Hubbard atom*, differently from temperatures higher than  $T_K$ . Furthermore, this also reflects the absence of a unique energy scale  $\nu^*$ .

The evident relation of the Kondo scale and the re-entrance point of the divergence lines allows for an "extrapolation" of the phase diagram calculated for the AIM in the following way: Due to the exponentially decreasing Kondo scale at large  $U$  the distance between the multiple divergence lines of the AIM will get smaller and smaller. This can be understood from the fact that, on the one hand, the divergence lines are always connected to the results of the *Hubbard atom* for higher temperatures than the re-entrance point and, on the other hand, they are bending towards higher interaction values for lower temperatures. This also suggests, in a sort of "Gedankenexperiment", how to make a prediction for the vertex divergences in the not yet investigated coexistence region of the Hubbard model in DMFT, which will be discussed as an outlook of this work in Chapter 6.

Beyond the overall similarities of the divergence lines of the *Hubbard model* to those obtained for the AIM, one qualitative difference was, how-

ever, found: In the case of the AIM a previously unobserved crossing of divergence lines of different kinds is found. While such a crossing is not in contradiction to the current understanding of irreducible vertex divergences, it calls for further, more precise studies of the low-temperature area of the phase diagram of the *Hubbard model*.

Additionally, the comparison of the singular eigenvectors of different divergence lines suggests that the symmetries in frequency space, specifically the odd symmetry found for the eigenvectors corresponding to the red divergence lines and the even symmetry found for the orange kind of eigenvectors, provides a valid distinction criterion between the two kinds of vertex divergences observed so far, generically applicable also to the most challenging correlated metallic regime.

In conclusion, this thesis has provided clear-cut answers to several questions in the context of the irreducible vertex divergences, especially for the role of the Kondo scale and of the metal-insulator transition. Although other important issues remain to be clarified, through the findings of this thesis, the possible paths how to proceed further have become clearer, as it will be explicitly outlined in Chapter 6.



# Chapter 6

## Outlook

After the discussion of the results obtained throughout this thesis, as well as of their implications, we want to present some among the most promising follow-up projects. This ranges from numerical refinements planned to rigorously prove the strong indications emerging from this Master work, to completely new calculations suggested by the same thesis' results.

### **Error Analysis**

Throughout this thesis, several claims considering the low-temperature properties of irreducible vertex divergences were made, which could be significantly substantiated further, from a numerical perspective, if results at even lower temperatures could be obtained. Among those claims, we want to recall here the most likely occurrence of a vertex divergence at a finite interaction value at  $T = 0$  and the approximately constant location of the maximum component of the singular eigenvectors as a function of Matsubara frequencies ( $i\nu$ ). In principle, CT-QMC calculations at lower temperatures are possible, but the relevant question is, whether it is possible to get precise enough results in a reasonable amount of computation time. To answer this question, we suggest to implement a resampling error analysis method, such as e.g., exploiting the  $n - 1$  Jackknife method [52, 53]. Using such a procedure it would be possible to add an error bar to the  $\tilde{U}$  values in the phase diagram, verifying rigorously the validity of the results obtained so far and revealing if calculations at lower temperatures can indeed yield meaningful results in reasonable computation times.

## Kondo scale

Another major result of this thesis is the identification of the role played by the Kondo scale. In fact, we found strong indications that the Kondo scale is connected to the re-entrance behaviour of, at least, the red divergence lines. However, the Kondo scale could be estimated hitherto only by exploiting approximative textbook expressions or, indirectly, through one-particle spectral properties. To bring a definite proof, the Kondo scale should be at best obtained from two-particle calculations for the local susceptibility of our specific model at different temperatures. If this connection is confirmed, we suggest to perform DMFT calculations in the coexistence region of the Hubbard model on the metallic side of the Mott transition, because we expect the occurrence of a particularly interesting configuration of divergence lines there. More precisely, the Kondo scale of the auxiliary AIM of a DMFT calculation goes to zero at  $U = U_{c2}$ , which means that, in the proximity of this interaction value, we can expect a kind of "compressed" version of the phase diagram of the AIM. This would lead to a situation where the divergence lines accumulate more and more as  $U_{c2}$  is approached, with the distance between the lines getting smaller and smaller. Also, one would expect that in this configuration only the re-entrance part of the lines remains as the Mott transition, on its metallic side, should "cut off" the part of the divergence lines connected to the *Hubbard atom* results and the parts bending towards higher interaction values for temperatures lower than  $T_K$ .

## Two-site model

Analysing an AIM with only a single bath site allows for analytic calculations of the ground state and the first excited ones. If also in such an oversimplified AIM a vertex divergence at a finite interaction value at  $T = 0$  takes place, as it is quite likely in the light of the new results of this thesis, it could be possible to gain an analytical insight about the microscopic processes controlling the vertex divergences of the AIM.

## Symmetry broken phases

Over a longer time perspective, it would be also very desirable to study the occurrence vertex divergences in the case of symmetry broken phases. In such situations, a considerably large amount of the interaction is "used" to stabilize the long range order. This means that not much of the interaction strength remains available to originate the non-perturbative divergences of the irreducible vertex. Hence, they can be expected to vanish or, at least, to appear at a weaker extent. This long-term project would be intrinsically

connected to the foreseen challenging development of DMFT extensions for the cases of symmetry broken phases.

# Bibliography

- [1] T. Schäfer, G. Rohringer, O. Gunnarsson, S. Chiuchi, G. Sangiovanni, and A. Toschi, *Divergent precursors of the Mott-Hubbard transition at the two-particle level*, Phys. Rev. Lett., **110**, 246405 (2013).
- [2] T. Schäfer, S. Chiuchi, M. Wallerberger, P. Thunstöm, O. Gunnarsson, G. Sangiovanni, G. Rohringer, and A. Toschi, *Non-perturbative landscape of the Mott-Hubbard transition: Multiple divergence lines around the critical end point*, Phys. Rev. B, **94**, 235108 (2016).
- [3] V. Janiš, and V. Pokorný, *Critical metal-insulator transition and divergence in a two-particle irreducible vertex in disordered and interacting electron systems*, Phys. Rev. B, **90**, 045143 (2014).
- [4] T. Ribic, G. Rohringer, and K. Held, *Nonlocal correlations and spectral properties of the Falicov-Kimball model*, Phys. Rev. B, **93**, 195105 (2016).
- [5] O. Gunnarsson, T. Schäfer, J.P.F. LeBlanc, J. Merino, G. Sangiovanni, G. Rohringer, and A. Toschi, *Parquet decomposition calculations of the electronic self-energy*, Phys. Rev. B, **93**, 245102 (2016).
- [6] E. Kozik, M. Ferrero, and A. Georges, *Nonexistence of the Luttinger-Ward functional and misleading convergence of skeleton diagrammatic series for Hubbard-like models*, Phys. Rev. Lett., **114**, 156402 (2015).
- [7] R. Rossi, and F. Werner, *Skeleton series and multivaluedness of the self-energy functional in zero space-time dimensions*, J. Phys. A, **48**, 485202 (2015).
- [8] A. Stan, P. Romaniello, S. Rigamonti, and L. Reining, and J. A. Berger, *Unphysical and physical solutions in many-body theories: from weak to strong correlation*, New J. of Physics, **17**, 093045 (2015).
- [9] O. Gunnarsson, G. Rohringer, T. Schfer, G. Sangiovanni, A. Toschi, *Breakdown of traditional many-body theories for correlated electrons*, arXiv:1703.06478



- [10] W. Tarantino, P. Romaniello, J. A. Berger, and L. Reining, *The self-consistent Dyson equation and self-energy functionals: failure or new opportunities?*, arXiv:1703:05587
- [11] N. F. Mott, *Metal-Insulator transition*, Rev. Mod. Phys., **40**, 4 (1968).
- [12] J. Kondo, *Resistance Minimum in Dilute Magnetic Alloys* Progress of Theoretical Physics **32**, 37 (1964)
- [13] G. Rohringer, A. Valli, and A. Toschi, *Local electronic correlation at the two-particle level*, Phys. Rev. B, **86**, 125114 (2012).
- [14] G. Rohringer, *New routes towards a theoretical treatment of nonlocal electronic correlations*, Ph.D. Thesis, TU Wien (2014).
- [15] A. Georges, and G. Kotliar, *Hubbard model in infinite dimensions*, Phys. Rev. B, **45**, 6479 (1992).
- [16] W. Metzner, and D. Vollhardt, *Correlated lattice fermions in  $d = \infty$  dimensions* Phys. Rev. Lett., **62**, 324 (1989).
- [17] T. Maier, M. Jarrell, T. Pruschke, and M. H. Hettler, *Quantum cluster theories* Rev. Mod. Phys., **77**, 1027 (2005).
- [18] G. Rohringer, H. Hafermann, A. Toschi, A. A. Katanin, A. E. Antipov, M. I. Katsnelson, A. I. Lichtenstein, A. N. Rubtsov, and K. Held, *Diagrammatic routes to non-local correlations beyond dynamical mean field theory* arXiv:1705.00024.
- [19] A. Toschi, A. A. Katanin, and K. Held, *Dynamical vertex approximation: A step beyond dynamical mean-field theory* Phys. Rev. B **75**, 045118 (2007).
- [20] K. Held, A. A. Katanin, and A. Toschi, *Dynamical Vertex Approximation: An Introduction* Prog. Theor. Phys. Suppl. 176, 117 (2008).
- [21] A. Valli, G. Sangiovanni, O. Gunnarsson, A. Toschi, and K. Held, *Dynamical Vertex Approximation for Nanoscopic Systems* Phys. Rev. Lett. **104**, 246402 (2010).
- [22] A. N. Rubtsov, M. I. Katsnelson, and A. I. Lichtenstein, *Dual fermion approach to nonlocal correlations in the Hubbard model* Phys. Rev. B **77**, 033101 (2008).

- [23] A. A. Abrikosov, *Methods of quantum field theory in statistical physics*, Pergamon Press (1965).
- [24] G. D. Mahan, *Many-particle physics*, Springer-Verlag (2000).
- [25] W. Nolting, *Grundkurs Theoretische Physik 7*, Springer-Verlag (2015).
- [26] D. Senechal, et al., *Theoretical Methods for Strongly Correlated Electrons* Springer-Verlag (2003), Chapter 6
- [27] J. K. Freericks and V. Zlati, *Exact dynamical mean-field theory of the Falicov-Kimball model* Rev. Mod. Phys., **75**, 1333 (2003).
- [28] M. Potthoff, *Non-perturbative construction of the Luttinger-Ward functional* Cond. Matt. Phys., **9**, 3(47), 557-567 (2006).
- [29] J.M. Luttinger, J.C. Ward, *Ground-State Energy of a Many-Fermion System. II* Phys. Rev., **118**, 1417 (1960).
- [30] G. Baym, and L. P. Kadanoff, *Conservation laws and correlation functions*, Phys. Rev. Lett., **124**, 287 (1961).
- [31] L. M. Falicov, and J. C. Kimball, *Simple Model for Semiconductor-Metal Transitions: SmB<sub>6</sub> and Transition-Metal Oxides*, Phys. Rev. Lett., **22**, 997 (1969).
- [32] P. W. Anderson, *Localized Magnetic States in Metals*, Phys. Rev. **124**, 41 (1961).
- [33] A. C. Hewson, *The Kondo problem to heavy fermions*, Cambridge University Press (1993).
- [34] J. Sólyom, *Fundamentals of the physics of solids, Volume 3 - Normal, broken-symmetry, and correlated systems*, Springer-Verlag (2010).
- [35] P. Philips, *Advanced solid state physics. second edition* Cambridge University Press (2012).
- [36] C. Enss, S. Hunklinger, *Low-temperature physics* Springer-Verlag (2005).
- [37] A. A. Abrikosov, *Physics* **2**, 5 (1965).
- [38] K. G. Wilson, *Rev. Mod. Phys.* **47**, 773 (1975).
- [39] N. Andrei, *Phys. Rev. Lett.* **45**, 379 (1980).

- [40] P. B. Wiegmann, Soviet Physics JETP Letters **31**, 392 (1980).
- [41] H. R. Krishna-murthy, J. W. Wilkins, K. G. Wilson, Rev. Mod. Phys. **47**, 773 (1975).
- [42] N. Parragh, A. Toschi, K. Held, and G. Sangiovanni, *Conserved quantities of SU(2)-invariant interactions for correlated fermions and the advantages for quantum Monte Carlo simulations*, Phys. Rev. B **86**, 155158 (2012).
- [43] E. Gull, A.J. Millis, A. I. Lichtenstein, A.N. Rubtsov, M. Troyer, and P. Werner, *Continuous-time Monte Carlo methods for quantum impurity models*, Rev. Mod. Phys., **83**, 349 (2011).
- [44] M. Wallerberger, *w2dynamics: Continuous time quantum Monte Carlo calculations of one- and two-particle propagators*, Ph.D. Thesis, TU Wien (2016).
- [45] P. Werner, A. Comanac, L. de Medici, M. Troyer, and A. J. Millis, *Continuous-time solver for quantum impurity models*, Phys. Rev. Lett., **97**, 076405 (2006).
- [46] J. E. Hirsch, and R. M. Fye, *Monte Carlo method for magnetic impurities in metals*, Phys. Rev. Lett., **56**, 2521 (1986).
- [47] E. Gull, *Continuous-time quantum Monte Carlo algorithms for fermions*, Ph.D. Thesis, ETH Zürich (2008).
- [48] M. Caffarel, and, W. Krauth, *Exact diagonalization approach to correlated fermions in infinite dimensions: Mott transition and superconductivity*, Phys. Rev. Lett., **72**, 1545 (1994).
- [49] A. Georges, G. Kotliar, W. Krauth, and, M.J. Rozenberg, *Dynamical mean-field theory of strongly correlated fermion systems and the limit of infinite dimensions*, Rev. Mod. Phys., **68**, 13 (1996).
- [50] P. Chalupa, *The First Line of Irreducible Vertex Divergences in the Anderson Impurity Model* Projektarbeit, TU Wien (2017).
- [51] P. Thunstrm, O. Gunnarsson, S. Ciuchi, and G. Rohringer, in preparation.
- [52] M. Knap, *Jackknife und Bootstrap*, Bakkalaureatsarbeit, TU Graz (2007)
- [53] J.Hughes, *The Jackknife and Bootstrap*, (2013)